Continuous mixing layer height determination

using the LD-40 ceilometer:

a feasibility study

Marijn de Haij
Wiel Wauben
Henk Klein Baltink

# Table of Contents

1   Introduction

1.1   The "Climate *changes* Spatial Planning" project ME2

The Kyoto Protocol is an agreement made under the United Nations Framework Convention on Climate Change (UNFCCC). Countries that have ratified this protocol commit to reduce their emissions of carbon dioxide and five other greenhouse gases (GHG), or engage in emissions trading if they maintain or increase emissions of these gases. The objective is the "stabilisation of greenhouse gas concentrations in the atmosphere at a level that would prevent dangerous anthropogenic interference with the climate system" (source: http://unfccc.int/).

Based on the Kyoto agreements, The Netherlands committed itself to a reduction of 6 % of their anthropogenic GHG emissions compared to the level of emissions in 1990. These reductions should be realised in the period 2008-2012. In addition, even stronger reductions are expected to be the result of negotiations for the period after 2012. The achieved reductions will be reported following standard IPCC-Guidelines. Basically, this is a bottom-up summation over various (anthropogenic) activities where the volume of each activity is multiplied by an emission factor. As reductions become more and more challenging to achieve, and as penalties for non-compliance may become more serious, the need for independent verification mechanisms at a national level will increase (Hutjes, 2005).

Inverse methods are able to provide such a verification of emission reductions. The inverse methods use measured time series of a GHG at one or more locations, together with transport and diffusion information provided by an atmospheric model. Although mainly used on continental to global scales until now, the principle of the methods seems also applicable to national scales (e.g. Dolman et al., 2004). The overall goal of the project 'Integrated observations and modeling of Greenhouse Gas budgets at the national level in The Netherlands', from here on referred to as the ME2 project, is to improve the description of the temporal and spatial distribution of greenhouse gases in The Netherlands. The ME2 project focuses on the long-lived components CO_2, CH_4, N_2O, SF_6, CO, HFC's and ^{222}Rn, and is divided in five Work Packages (WPs), which have their own specific tasks. An overview of these WPs and their relations is schematically presented in Figure 1.1. The ME2 project is executed under the umbrella programme "Besluit Subsidies Investeringen Kennisinfrastructuur – Klimaat voor Ruimte" (BSIK-KvR), within the theme "Mitigation".

The main objective of Work Package 1 (WP1) is to address the influence of the dynamics and mixing processes in the Planetary Boundary Layer (PBL) on GHG concentrations that are observed in the PBL. An important task is the continuous monitoring of PBL height and the driving variables for PBL growth (e.g. sensible heat flux) at several locations in The Netherlands. Another task of WP1 is to improve understanding of currently most limiting PBL aspects by performing specific experiments. Finally, the WP will develop improved PBL parameterisations for mesoscale models, making use of existing and new understanding of PBL processes.
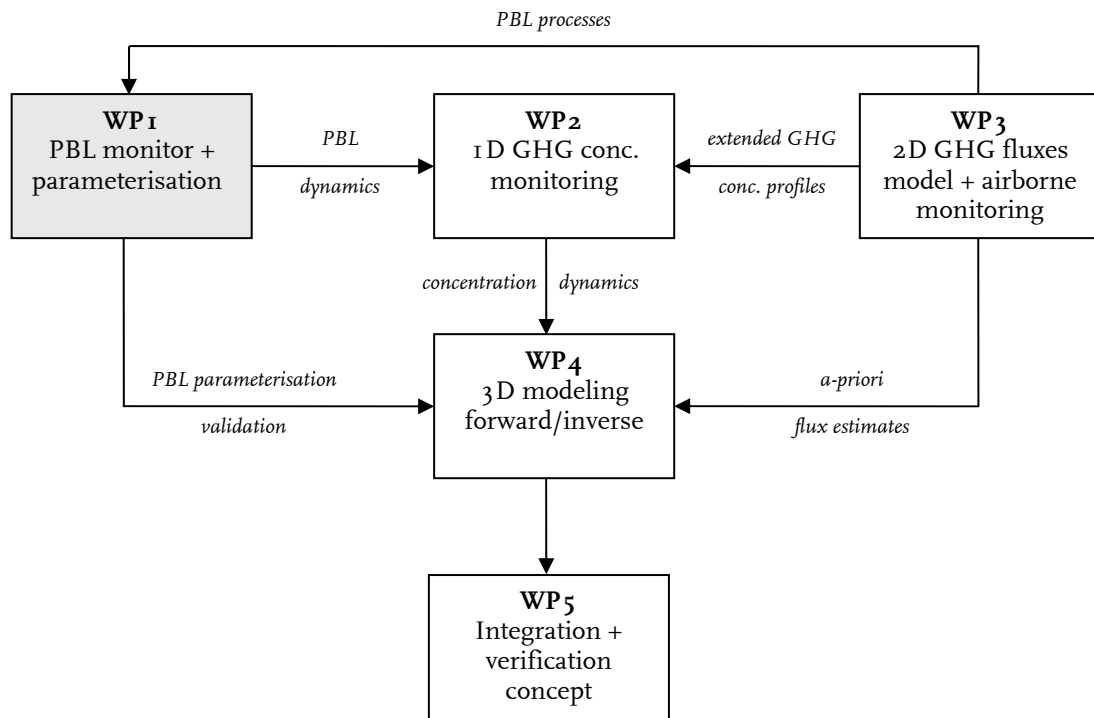
FIGURE 1.1. Overview of the five Work Packages in the BSIK-KvR ME2 project (from: Hutjes, 2005).

This report presents the results of the feasibility study performed within the subtask 'Determination of the height of the atmospheric boundary layer from a network of ceilometers' of Work Package 1. The height of the planetary or atmospheric boundary layer, also commonly referred to as mixing layer height (MLH), is a key parameter in monitoring and modeling dispersion of atmospheric constituents. It primarily determines the volume in which turbulence is active and into which constituents which are emitted near the surface are dispersed. In the context of inverse methods, it is one of the main parameters within the required atmospheric transport and diffusion information.

1.2 Goals and setup

The two goals of the aforementioned subtask under WP1 are:

1. Development, test and evaluation of an algorithm for the determination of the mixing layer height from backscatter profiles of the Vaisala LD-40 ceilometer, which is operational at the Royal Netherlands Meteorological Institute (KNMI).
2. Monitoring of the mixing layer height within a network of at most 5 operational ceilometers, during a measurement campaign of 2 years.

In this report only the first goal will be considered, concerning the development of an algorithm for mixing layer height determination. It consists of a feasibility study, algorithm description and results obtained from archived data during the period 2000 to 2006. The feasibility study is carried out to investigate whether it is possible to derive mixing layer height from the backscatter profiles of the commercial LD-40 ceilometer. A

positive answer to this question is mandatory for the second stage to be executed. KNMI operates LD-40 ceilometers at 18 different locations (reference date January 1, 2006) in its meteorological measurement network in The Netherlands.

The second stage is embedded within the BSIK-KvR observational campaign, which is scheduled for the years 2007 and 2008. A well-considered collocation of the LD-40 ceilometers with scintillometry instruments operated within the consortium by Wageningen University is aimed for and would provide the opportunity to couple PBL height dynamics directly to measurements of sensible heat flux. If satisfactory results are achieved in both stages of the subtask, the need for the estimation of the temporal and spatial variation of PBL height on the scale of The Netherlands will be served.

1.3   Determination of mixing layer height

Within the feasibility study presented in this report an algorithm has been developed and compared with existing methods applied to reference data to assess the quality and success rate of MLH determinations with the LD-40 ceilometer. Backscatter profiles at location De Bilt (KNMI station number 261) have been stored continuously for a period of six years. This data set is used in the development and testing of the algorithm. Comparison is possible with radiosonde measurements at the same location, as well as with some routinely inferred mixing layer height estimates from a wind profiler radar and a research lidar at nearby sites.

If one determines MLH from lidar or ceilometer backscatter profiles the results can get contaminated due to the influence of advected or accumulated aerosol layers or cloud layers, which contribute to the backscatter profile. Furthermore, nocturnal (stable) boundary layers do not always show very well defined aerosol gradients at their top. This can cause a questionable MLH determination. All these shortcomings are listed in literature, and lead to problematic determination of mixing layer height in such cases (e.g. Fischer et al., 1998; Seibert et al., 2000). Most of the MLH studies have been carried out using a research lidar from the ground or mounted on an aircraft, but also commercially available ceilometers, radiosondes, sodars and wind profilers are commonly used measurement platforms for this purpose.

Dispersion models assume that turbulent dispersion takes place in the mixing layer, and not beyond the mixing layer height. Hence, the mixing layer height forms a sharp boundary between the volume in which constituents are mixed very well, and the relatively clean free atmosphere. A complication is that some plumes penetrate through this boundary, whereas other plumes undershoot it. This principle is driving the so-called entrainment zone, a distinct layer on top of the mixing layer that coincides with the MLH, and in which air from the free atmosphere is entrained. More recent models can deal with this phenomenon and aim at quantifying the constituent flux that penetrates beyond the MLH (Fischer et al., 1998). Therefore, not only the mean MLH is considered but also a preliminary assessment is made to estimate the thickness of the entrainment zone from the observations.

1.4 Outline

The main terminology and processes concerning the atmospheric boundary layer are introduced in chapter 2. Existing methods for MLH determination from recent literature are described, as well as the main advantages and disadvantages of the instruments used.

In chapter 3 the characteristics of the Vaisala-Impulsphysik LD-40 ceilometer are described. Furthermore, the data preprocessing steps common to both MLH algorithms described in chapter 4, are presented. These steps have to be made in order to deliver proper data to the MLH algorithms.

Chapter 4 presents the two MLH algorithms that are considered. The algorithms are described, and a quality index is introduced which indicates the reliability of the MLH obtained from the ceilometer backscatter profiles.

In chapter 5 a number of case studies are considered, which represent commonly occurring conditions. A comparison with the KNMI wind profiler in Cabauw, the RIVM backscatter lidar in Bilthoven and the regional climate model RACMO is also presented.

The results of the algorithm intercomparison and the comparison with other platforms (radiosonde, wind profiler) are presented in chapter 6. Finally, a choice is made for one of the two considered MLH algorithms.

Chapter 7 gives the conclusions of this feasibility study and lists some recommendations including suggestions for improving the results.

Finally, the Appendices contain a description of some additional applications and features of the LD-40 backscatter measurements and their preliminary results.

2 The atmospheric boundary layer

2.1 Theory

The atmospheric boundary layer (ABL) is defined as "the part of the troposphere that is directly influenced by the presence of the Earth's surface, and responds to surface forcings with a timescale of about an hour or less" (Stull, 1988). It is the layer directly coupled to the surface with a typical height at the mid-latitudes between 50 and 2000 m. The actual height of the boundary layer depends on for example the season, time of day, the synoptic situation and local conditions as orography, land use and surface roughness.

The vertical transport of heat, moisture, momentum and constituents in the ABL is driven by turbulence, due to both mechanical and thermal forces. Mechanically forced turbulence is generated by wind shear, whereas thermal turbulence is generated by buoyant convection. The latter is the result of inhomogeneous heating of the surface, which occurs in both time and space. Structures that establish in the presence of buoyant convection are called thermals or convective plumes. The number and intensity of convective plumes in the boundary layer are strongly connected to the local atmospheric stability.

The density of air is not only dependent on temperature, but also on moisture content. Water vapor lowers the density of air, whereas the presence of liquid water makes air denser. The virtual temperature T_v is a variable that is introduced to characterise stability:

$$T_v = T(1 + 0.61q_v - q_l)$$

where T [in K] is the air temperature and q_v [in g/g] and q_l [in g/g] denote the water vapor specific humidity and liquid water content, respectively. The virtual temperature can be interpreted as the temperature air would have after removal of all moisture. A useful property of the virtual temperature is that it is inversely proportional to the density of air.

The virtual potential temperature θ_v is the virtual temperature corrected for cooling or warming effects due to adiabatic pressure change:

$$\theta_v = T_v \left(\frac{p_0}{p} \right)^{R_d / c_p}$$

where p_0 is a given reference pressure, with a value of 10^5 Pa. Furthermore, p [in Pa] represents the pressure of the air and $R_d / c_p \cong 0.286$.

The local stability of the atmosphere can now be considered in terms of the lapse rate Γ of virtual potential temperature, which is defined as:

$$\Gamma = \frac{\partial \theta_v}{\partial z}$$

The actual lapse rate can be compared with standard conditions that hold for dry-adiabatic and wet-adiabatic situations, i.e. for unsaturated and saturated (cloudy) air respectively. The lapse rate for a dry-adiabatic displacement, Γ_d, is zero by definition, whereas the lapse rate for a wet-adiabatic displacement, Γ_m, is positive due to latent heat release of the condensation process. The latter has a typical value of 4 K/km, for T = 288 K, p = 1000 hPa and q_v = 11 g/kg.

Three cases of atmospheric stability can be distinguished:

- Absolutely unstable: $\quad\quad\quad\quad\quad\quad \Gamma < \Gamma_d$
  In an absolutely unstable situation the vertical displacement of an air parcel will lead to a further rise, due to positive buoyancy with respect to its environment. This situation typically occurs in the surface layer.

- Conditionally unstable: $\quad\quad\quad\quad\quad \Gamma_d < \Gamma < \Gamma_m$
  In a conditionally unstable situation the result of a vertical displacement of an air parcel depends on whether the air parcel is saturated or not. If it is unsaturated, the atmosphere is stable, while for saturated air it is unstable. The latter is caused by the contribution of latent heat release to buoyancy production. Typically, this situation occurs in a cloud layer.

- Absolutely stable: $\quad\quad\quad\quad\quad\quad\quad \Gamma > \Gamma_m$
  In an absolutely stable situation the vertical displacement of an air parcel will lead to negative buoyancy, which results in a subdued vertical motion such that the air parcel will fall back to its original level. This situation typically occurs in the nighttime stable boundary layer and in the inversion layer.

2.2 Diurnal cycle

Solar radiation is the main driving force behind the diurnal evolution of the boundary layer. When incoming short wave radiation starts to heat the surface shortly after sunrise, the air near the surface gets unstable which leads to the process of buoyant convection. Especially in high-pressure areas over land, turbulent activity can persist during the day as a result of the incoming radiation, causing a convective mixing layer to build up. When the sun sets and turbulence dies out, the convective mixing layer decays and a nocturnal stable layer sets in. A residual layer is frequently observed on top of this stable layer. This layer is characterised by the same properties as the previous mixing layer, though fully decoupled from the surface.

A schematic picture showing the diurnal cycle of a well defined boundary layer over land is presented in Figure 2.1. Four types of layers can be discriminated: a) the surface layer, b) the convective mixed layer (with entrainment zone on top), c) the nocturnal (or stable) boundary layer and d) the residual layer.

2.2.1 Surface layer

The surface layer is a thin layer directly above the surface. The vertical extent of this layer is typically 50 – 100 m, about 1/10th of the height of the boundary layer. It is defined as

the region where the turbulent fluxes and stresses are almost constant with height and vary by less than 10 % of their surface magnitude (Stull, 1988).

During daytime, the surface layer can get into a superadiabatic situation, as a result of a positive (upward pointed) heat flux. This is caused by heating of the soil by shortwave solar radiation. During such a situation, the air in the surface layer is potential warmer and contains more moisture than the air above. The unstable situation that has established can get into balance again by a vertical mixing process, by air that tends to rise from the surface and mixes with air at higher levels. This is where the buoyant convection process originates and a thermal starts to rise.
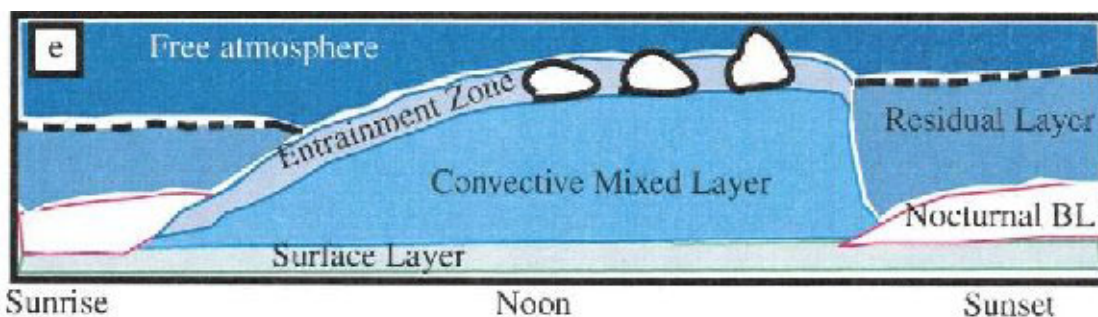
FIGURE 2.1. Diurnal cycle of the boundary layer, which is typically observed during the occurrence of a high pressure area over land (from: Cohn and Angevine, 2000).

2.2.2 Convective mixed layer

The most important source of turbulence in the convective mixed layer is buoyancy, but also wind shear can be present and contribute to turbulent mixing. Convective sources not only include the heat transfer from the warm surface layer, but also downward radiative cooling from the top of a boundary layer clouds (Stull, 1988). The latter has a suppressing effect on convective activity.

In the cloud-free convective mixed layer, turbulent eddies tend to mix heat, moisture, momentum and constituents uniformly in the vertical. This process is initiated by a statically unstable situation where thermals rise from the surface. This causes the profiles of these variables to be fairly uniform within the mixed layer, which is demonstrated in the vertical profiles of virtual potential temperature and relative humidity measured by radiosonde in Figure 2.2. On top of the convective mixed layer a capping stable layer is present, the so-called inversion layer or entrainment zone. It is characterised by an inversion in (potential) temperature, together with a strong decrease in specific humidity. A typical value for the height of the noontime convective mixed layer is 500 to 2500 m.

Not all convective plumes have the same amount of buoyancy. The most active buoyant plumes will overshoot the mean convective mixed layer top into the free atmosphere. The plumes that overshoot will fall back into the convective mixed layer if they run out of available potential energy, taking warm and dry air from the free atmosphere with them. This process is called entrainment. In general, the inversion layer is found on top of a developing convective mixed layer and restrains the vertical domain in which turbulence is active. It can be seen as the interface between the convective mixed layer and the free atmosphere. If humidity exceeds a pressure and temperature dependent saturation level

and the plume has enough potential energy available to rise further, a cumulus cloud forms on top of the convective mixed layer.
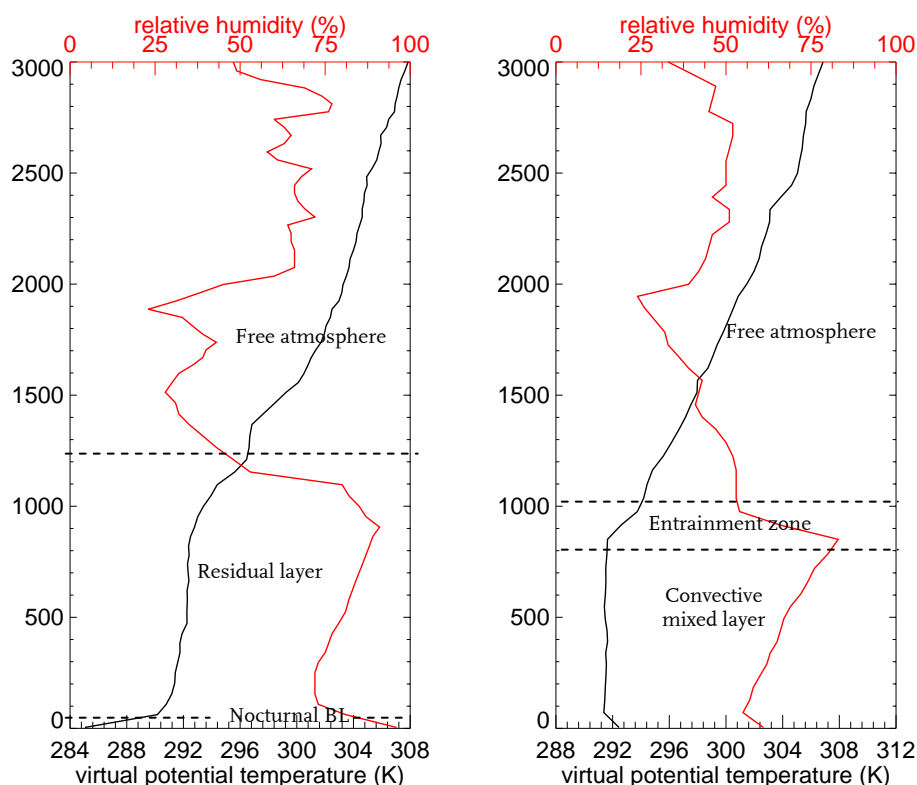
FIGURE 2.2. Radiosonde measurements of virtual potential temperature (black) and relative humidity (red) for De Bilt on August 17, 2005, 00 UTC (left) and 12 UTC (right).

As most atmospheric constituents (like aerosol) are emitted near the surface, they will also experience the turbulence that is present in the mixed layer. The constituents are dispersed throughout the mixed layer by convective plumes as well, and the inversion layer that is on top of the mixed layer also restrains the domain in which the vertical transport of these constituents takes place. In fact, the inversion layer is a transition between the polluted mixed layer and the relatively clean free atmosphere. This offers an opportunity to detect the height of the mixed layer by the negative gradient in e.g. the aerosol profile.

2.2.3 Nocturnal (stable) boundary layer

If the surface is cooler than the air above, the boundary layer is stably stratified. The most important example of a stable boundary layer is the nocturnal boundary layer. During nighttime, incoming shortwave radiation is no longer available for heating the soil, and the cooling due to outgoing longwave radiation (particularly during clear sky situations) causes the surface heat flux to become negative. Hence, turbulence due to buoyancy forces is not present in this type of boundary layer.

Turbulence can be present in the nocturnal boundary layer in an intermittent or patchy form, driven by wind shear. The wind speed as well as the wind direction may vary strongly with increasing altitude. This means that constituents also show a very strong

but complex horizontal dispersion. Typically, the nocturnal boundary layer is some tens to a few hundreds of metres deep.

2.2.4   Residual layer

Turbulence which is present in the well-mixed layer will decay from about half an hour before sunset, due to weaker buoyant fluxes. In the absence of strong advection processes, a layer can establish that is characterised by the same initial state variables and constituent concentrations as in the previous mixed layer (Stull, 1988).

The residual layer (RL) is neutrally stratified, hence turbulence will be active almost equal in all directions. Residual layer height is fairly constant during the night. As it is separated from the surface by the nocturnal (stable) boundary layer, there is no influence from the surface on the RL properties. In most cases, the residual layer is present until the moment the next day's convective mixed layer develops to a level corresponding to the RL height.

2.3   Mixing layer height determination

In this section the theory and principles before mentioned are used to discuss the feasibility of existing methods for boundary layer height determination from different types of atmospheric measurements. The terms 'mixed layer' and 'mixing layer' are commonly used in studies in which the objective is to determine the maximum height for dispersion of constituents. A lot of different definitions exist in literature (Fischer et al., 1998). From now on, this height is called the mixing layer height or MLH.

Various instruments and models have been used to determine mixing layer height during the past decades. All of these have their advantages and disadvantages. It is stated that one should use a combination of measurements to describe the evolution of MLH accurately (Seibert et al., 2000). For several measuring platforms, the advantages and disadvantages are listed in Table 2.1. The reader is referred to Fischer et al. (1998) for a complete overview of commonly used methods to determine mixing layer height.

2.3.1   Lidar

The LIDAR (Light Detection And Ranging) principle offers an opportunity to detect boundaries in the atmosphere that are characterised by a transition in tracer concentration. A lidar system transmits laser pulses and measures the backscattered signal. The backscattered signal depends on the amount and nature of scattering particles in a certain volume of air. The time interval between transmission and reception of the signal determines the corresponding altitude. The vertical range of a lidar system is mainly limited by the presence of low optically thick (boundary layer) clouds, precipitation and fog. The sensitivity of a lidar is a function of (the product of) emitted laser power, receiving telescope area, photosensitivity and resolution of the detector. A lower sensitivity generally reduces the signal-to-noise-ratio of the measured backscatter. This has limiting consequences for the vertical range in which a reliable backscatter signal is available.

TABLE 2.1. Overview of advantages and disadvantages of several instruments used for mixing layer height determination (Adapted from: COST 710 Final Report (Fischer, 1998)).

Instrument	Advantages	Disadvantages
Radiosonde (operational)	-routine ascents all over the world -data transmitted via international networks, therefore suited for operational use -compatibility with measurements in the free atmosphere	-provides only snapshot of the ABL -limited height resolution -operationally only 2-4 soundings a day at fixed times -tracking problems at low levels
Tethered balloon	-ascent velocity can be chosen -measurements of turbulence and trace gas concentration possible	-limited to field campaigns -synchronous profile measurement difficult -limited measurement range, usually < 500 m -not possible in cases of high wind speed of strong convection
Mast	-installation of a large number of different sensor types possible including turbulence measurements -continuous operation	-very high installation / operation costs -limited range: 200-300 m -high vertical resolution requires a high number of sensors
Research aircraft	-possibility to operate many different sensors (meteorology, chemistry, turbulence, remote sensing) -provides spatial information, specifically suited for mesoscale studies	-high costs, only for special field studies -operation mostly limited to daylight hours -lowest flight level subject to restrictions (safety)
Radar / Wind profiler	-ground based and aircraft based operation possible (radar) -different scanning modes possible for 3D studies (radar) -high sampling rate and continuous operation	-lowest range normally not below 200 m -limited vertical resolution (50-250 m) -expensive -frequency allocation problems within Europe
Sodar	-relatively simple, not very expensive: suited for long-term operation -high temporal and vertical resolution	-limited sounding range (500-1000 m) -sensitivity to environmental noise -noise contamination to the environment
Lidar	-ground based and aircraft based operation possible -different scanning modes possible for 3D studies -high sampling rate -return signals directly from aerosols	-expensive -unattended operation often not possible -tracer necessary (gas, aerosol) -incomplete overlap lower range gates (for bi-axial systems)
Ceilometer	-not very expensive, suited for unmanned long-term operation -in operational use all over the world -high temporal and vertical resolution	-tracer necessary (gas, aerosol) -limited sensitivity -incomplete overlap lower range gates (for bi-axial systems)

A ceilometer is a commercial lidar system that is primarily used for the detection of cloud base heights for aviation and synoptic weather purposes. It transmits light at a single wavelength and is eye-safe in its operation. Ceilometers are typically designed to operate and measure continuously for long periods without maintenance. In general, ceilometers have a lower sensitivity than high power research lidars.

The presence of aerosols can be detected in the backscatter profiles of ceilometers. Aerosols are mainly emitted at the surface and the concentration of aerosol is therefore generally higher in the mixing layer than in the free atmosphere. Therefore, the MLH estimation from lidar systems is based on the detection of the sharp decrease in aerosol backscatter at the top of the mixing layer. This negative gradient marks the interface between the polluted mixing layer and the relatively clean free atmosphere. Furthermore, it has been shown that the backscatter time variance often has a local maximum around the top of the convective mixing layer (e.g. De Ruiter and Swart, 1991; Hennemuth and Lammert, 2006). This is related to the dynamic behavior of the air at the mixing layer top and the associated strong exchange of air originating from the free atmosphere throughout the entrainment zone.

Backscatter gradient and variance methods are frequently used in mixing layer height estimation studies with lidars. De Ruiter and Swart (1991) developed an algorithm for mixing layer determination from the backscatter measurements of a 1064 nm backscatter lidar, operated by the National Institute for Public Health and the Environment (RIVM) for air quality purposes. The principle of the algorithm is the search for data points in the backscatter profile at which both a strong negative backscatter gradient and a strong time variance occur. Under poorly defined meteorological conditions (rain, fog), the mixing layer height can not be calculated.

Hourly MLH values from the RIVM lidar were compared to the MLH as derived from radiosonde measurements. A linear regression for data logged during two weeks in autumn resulted in a correlation of 0.93, and a linear fit $y = ax + b$ with coefficients $a = 0.98 \pm 0.03$ and $b = 52 \pm 25$ m. It should be remarked that this agreement covers only 54 % of the measurement results, mainly because the two measurement platforms did not always estimate layer tops at the same time. A good correlation between MLH estimates from the RIVM lidar and radiosonde MLH at noontime was also found by Van Pul et al. (1994).

Schäfer et al. (2004) used the altitude of minimum backscatter gradient as an indicator for MLH. In this study, 10 minute and 180 m averaged backscatter profiles of the LD-40 ceilometer were considered for the estimation of MLH in several cases. It was shown that the LD-40 can estimate the mixing layer height fairly well in the absence of low clouds and precipitation. For some cases the results were compared to the MLH estimated by a sodar (see section 2.4.3), in order to show the different abilities of optical and acoustic remote sensing systems. This comparison showed that generally, the sodar is more sensitive to low inversions than the ceilometer.

Sicard et al. (2004) made a comparison of three different methods for MLH detection by research lidar in the Barcelona area. They made use of (1) the minimum of the first vertical derivative of backscatter, (2) the minimum of the second vertical derivative of backscatter and (3) the minimum of the first vertical derivative of the logarithm of backscatter. All three methods performed very similar for the considered cases. Method (2) showed the best results with respect to the Richardson bulk MLH method applied to radiosonde measurements with a correlation coefficient of 0.969 and a standard deviation of 82 m. The correlation coefficients of (1) and (3) were 0.963 and 0.979, respectively, whereas the standard deviations were 89 and 101 m. However, the number of cases in the analysis is limited to 29 and cases with clouds or significant secondary aerosol layers on top of the mixing layer were discarded.

Menut et al. (1999) also used the minimum of the second vertical derivative of backscatter (the so-called 'inflection point') and compared MLH estimations from a research lidar with radiosonde (Richardson bulk) detections. Furthermore, a backscatter variance method was used, which always reported higher MLH values than the inflection point method. Individual comparisons differed 100 m or even more. However, the correlation with the radiosonde detections was good; correlation coefficients of 0.99 and 0.98 and standard deviations of 15 and 25 m were found for the inflection point and variance method, respectively. Again, the number of cases for the comparison is low, only 10 for this study. Important limitations of the methods were again the presence of fog and rain. It was shown that the simultaneous use of the inflection and variance methods can be advantageous in some cases.

Steyn et al. (1999) applied a technique called "simulated annealing" for the determination of mixing layer height and entrainment zone thickness (EZT) from lidar. The Steyn method is based on fitting a four parameter, idealised profile (based on the error function) to observed profiles of aerosol backscatter ratio. It was shown that the method is a very robust one and that it is able to detect MLH and EZT even in difficult cases. However, the backscatter profile should consist of a fairly uniform backscatter in and above the mixing layer, with a sharp transition at the interface. The most difficult cases were those in which the backscatter differed only slightly, or the ones containing plumes or strongly scattering air in the mixing layer or upper layers. This method was later adopted by Eresmaa et al. (2006), in which MLH was estimated from measurements of the CT25K ceilometer and compared to radiosonde MLH estimates. For a comparison with the Richardson bulk method, a linear fit $y = ax + b$ with coefficients a = 0.80 ± 0.10 and b = 47 ± 89 m and a correlation coefficient of 0.90 was found for convective cases. For stable cases, the results that were found are a = 0.62 ± 0.16 and b = 120 ± 34 m, and a correlation coefficient of 0.80.

In recent studies on MLH determination from lidar observations wavelet transforms were also commonly used (Cohn and Angevine, 2000; Davis et al., 2000; Brooks, 2003). The most important advantage of wavelet methods is the decomposition of the signal in both altitude as well as vertical spatial scale of the structures in the backscatter signal. Cohn and Angevine (2000) found a good agreement between estimates of MLH by two lidars and a wind profiling radar (correlation coefficients of 0.87 and 0.95). It was shown that

the (Haar) wavelet transform is a powerful tool to detect a significant decrease in aerosol backscatter, even at very high time resolution. A vertical averaging of the profile, like for the application of gradient/variance methods, does not seem necessary because of the implicit averaging included in the application of the wavelet transform.

Davis et al. (2000) applied wavelet analysis to airborne infrared lidar data to obtain an objective determination of boundaries in aerosol backscatter that are associated with boundary layer structure. The dilation (width of the wavelet) corresponding with the maximum in wavelet variance was used for the determination of these boundaries. The method was adapted for cases with a lot of noise in the backscatter signal. Based on four different cases with different instruments, it was shown that the Haar wavelet is a very strong tool for this purpose, which enables one to detect high-resolution spatial variability of planetary boundary layer height, even in complex, multilayered situations.

Brooks (2003) continued to study the wavelet MLH methods introduced by Cohn and Angevine (2000) and Davis et al. (2000) An extensive theoretical analysis of the method was carried out in order to study the MLH determination from backscatter profiles that deviate from the ideal situation, e.g. with a sloping background or a deep inversion. It was found that the method produces dilation-dependent errors in the MLH determination. An alternative method was developed using multiple dilations. With this method, it seems possible to identify the upper and lower limits of the backscatter transition zone, while the impact of a sloping background is minimised. The method was applied to an airborne lidar backscatter cross section to demonstrate its benefits.

Conditions like fog, boundary layer clouds, precipitation or advected aerosol layers, caused problems in the determination of MLH in all studies concerning this subject. In these situations, it is very hard to distinguish unambiguously between the top of the mixing layer and the other features in the backscatter profile that also show a strong gradient signature.

2.3.2 Radiosonde

Determination of MLH from a thermodynamic point of view, in which for example temperature and humidity profiles from a radiosonde are used, is the most direct one. A disadvantage of the use of radiosondes is that they are only operated routinely at fixed synoptic times, with a maximum of two or four radiosondes a day. Consequently, continuous monitoring of mixing layer height with this measurement platform is not possible.

A commonly used method which is suitable for stable as well as for unstable conditions is the Richardson bulk method (Vogelezang and Holtslag, 1996; Menut et al., 1999; Sicard et al., 2004; Hennemuth and Lammert, 2006). The Richardson number is a scaling parameter that indicates the ratio of thermal and mechanical production of turbulence. It has a characteristic behavior for the mixing layer and the free atmosphere on top of it.

The Richardson bulk number R_{ib} is calculated as:

$$R_{ib}(z) = g \frac{(z - z_0)}{\theta(z)} \frac{[\theta(z) - \theta(z_0)]}{u(z)^2 + v(z)^2}$$

with g the gravity constant of 9.81 m/s², z [in m] and z_0 [in m] represent altitude and the altitude of the lowest level of observation. Furthermore, θ [in K] denotes potential temperature ($\theta = T(p_0 / p)^{R_d / c_p}$) and $u(z)$ [in m/s] and $v(z)$ [in m/s] are the zonal and meridional components of the wind vector, respectively. The numerator can be interpreted as a buoyancy term, in which thermal rising potential is described. The denominator contains information about wind shear. Here it is assumed that the wind speed at z_0 is zero.

Mixing layer height can be defined as the height of the first level at which the Richardson bulk number exceeds a certain threshold value, such that $R_{ib} > R_{ibc}$ (Sicard et al., 2004). A common value for R_{ibc} reported in literature is 0.21. Beyond this critical value of R_{ib} the atmosphere can be considered fully decoupled from the mixing layer.
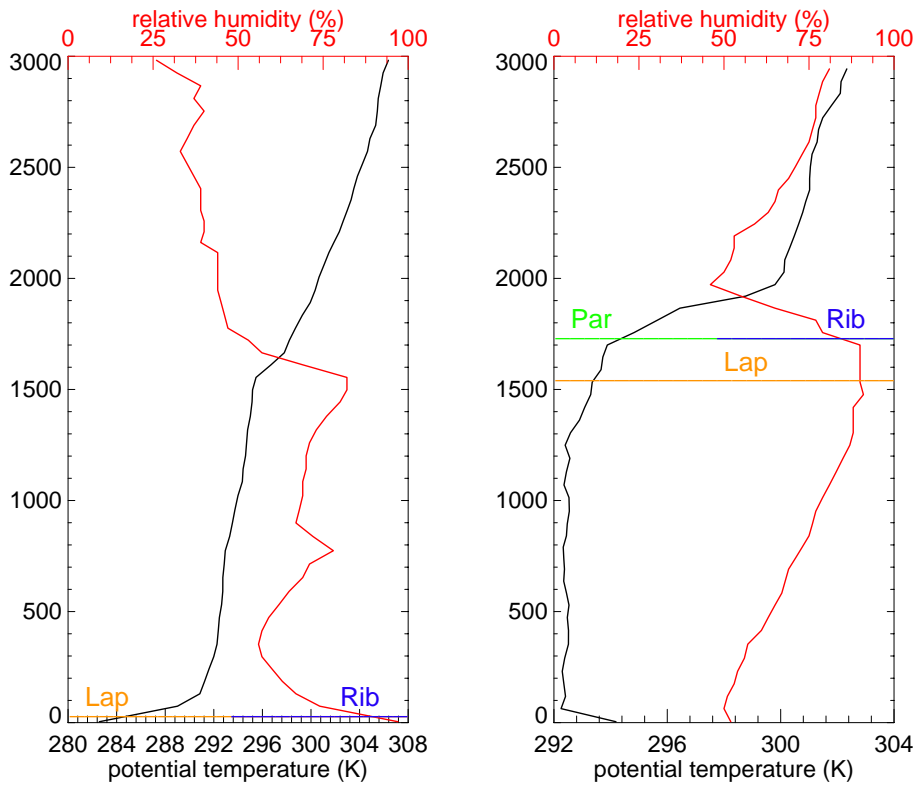
FIGURE 2.3. Radiosonde measurements of potential temperature (black) and relative humidity (red) for De Bilt on July 8, 2003, 00 UTC (left) and 12 UTC (right). Estimates of mixing layer height by the Richardson bulk (Rib), Parcel (Par) en Lapse rate (Lap) methods are presented.

The parcel method for MLH determination is only suitable in convective situations and is based on the notion that parcels rise from the surface throughout the mixing layer because they have enough buoyancy with respect to their environment. At a certain level the parcel becomes colder than the environment, and the rising motion of the parcel terminates. A simple approach of the parcel method is the fixation of mixing layer height at the level at which the straight vertical line of surface potential temperature crosses the

potential temperature profile for the first time. Extensions have been made on this approach with the use of a surface excess temperature, which is determined by surface flux and friction velocity parameters. The result is the so-called advanced parcel method (see e.g. Seibert et al., 2000).

Another method for the determination of the mixing layer height from radiosonde observations is based on vertical gradients in potential temperature and/or relative humidity (Garrett, 1981). Because the mixing layer is characterised by profound mixing of thermodynamic properties, gradients in the mentioned quantities are expected to be very small. The inversion present on top of the mixing layer shows significant gradients in potential temperature and relative humidity, towards the warmer and drier free atmosphere. The algorithm of Hayden et al. (1997) detects MLH at the first level at which the vertical gradient in potential temperature exceeds 2 K/km. This kind of method is commonly called the lapse rate method, because it is triggered on a prescribed value or on a combination of prescribed values of lapse rates in atmospheric variables.

Radiosonde profiles of pressure, air temperature, relative humidity, dewpoint temperature and wind speed are interpolated to a 10 m vertical grid starting at 5 meters above the surface. The above mentioned methods are applied to the derived variables and radiosonde MLH can be calculated for each available sounding, following:

- the Richardson bulk number method with $R_{ibc} = 0.21$
- the simple Parcel method
- the Lapse rate method, triggered on a gradient in $\theta > 2$ K/km and a gradient in RH < 0 [%/km]

The lowest possible height of detection is 25 m. No MLH is detected for stable surface conditions, concerning the Parcel method.

An example of estimates made by these radiosonde methods is given in Figure 2.3. Note the good agreement between the methods for the 12 UTC sounding, especially between the Parcel and Richardson bulk (both 1725 m) methods. The Lapse rate method reports a MLH of about 200 m lower (1535 m), because the potential temperature profile already starts to increase gradually at that height. For sharper inversions the three methods converge to a larger extent than shown here.

2.3.3 Wind profiler

A wind profiler is a Doppler radar which looks almost vertically into the atmosphere. It has the ability to measure vertical profiles of wind, radar echo strength and turbulence above the profiler antenna. Wind profilers operate at frequencies between 40 and 1400 MHz. Wind measurements are made typically by pointing the radars antenna beam in 3 or 5 different directions. The Doppler shifts of the received echoes in each direction are combined to determine the horizontal wind speed and direction. These echoes occur mainly from turbulence, rain, snow and cloud droplets, but incidentally also from insects or birds. Buildings in the sight of view and airplanes also lead to false echoes.

The wind profiler appears to be a very promising device for direct and continuous measurement of mixing layer height in a deep convective boundary layer (Seibert et al., 2000). In general, the backscatter intensity of the electromagnetic signal is proportional to the structure parameter C_n^2. The vertical profile of this parameter usually exhibits a maximum at the top of a developed CBL, because it largely depends on small-scale fluctuations in temperature and moisture. Several algorithms on MLH estimation from wind profiler measurements have been developed, see e.g. Grimsdell and Angevine (1998) and Bianco and Wilczak (2002).

The atmospheric research department (KS/RK) of KNMI operates a Vaisala LAP-3000 wind profiler/RASS (Radio Acoustic Sounding System) at the research site in Cabauw, since July 1994. It operates at a frequency of 1290 MHz and measurements are taken in 5 different beam directions. Operation is possible in two different modes, dependent on the required vertical resolution and height coverage. The latter depends on the atmospheric scattering conditions and transmitted power. Most important measurements of the KNMI wind profiler are those of wind speed, wind direction, vertical wind velocity and virtual temperature fields (RASS).

An algorithm was developed for the estimation of mixing layer height from the wind profiler backscatter profiles and the width of the Doppler velocity spectrum. This algorithm does not only take into account the vertical profile of the structure parameter C_n^2, but combines the local maximum in C_n^2 with a minimum in spectral width for the proper detection of the MLH. Estimates of MLH are made automatically every 10 to 20 minutes and are subsequently edited manually.

2.3.4 Sodar

SODAR (Sound Detection And Ranging) systems are used to remotely measure the vertical turbulence structure and the wind profile of the lower layer of the atmosphere. Sodar systems operate like radar systems except that sound waves rather than radio waves are used for detection. It is also a commonly used measurement platform for the routine estimation of mixing layer height (Seibert et al., 2000).

Sodar signals are scattered by temperature inhomogeneities in the atmosphere, characterised by the structure parameter of the acoustic refractive index, C_n^2. Hence, the SODAR principle closely resembles the wind profiler (section 2.3.3) principle. Several methods exist to derive MLH from the vertical profile of C_n^2, see e.g. Beyrich (1997), Emeis et al. (2004), Asimakopoulos et al. (2004). The vertical range of most sodars is limited to about 1 km, which restrains the instrument from detecting deep convective MLHs. The vertical range depends both on acoustic frequency of the SODAR and the atmospheric conditions The lowest range gate of a typical sodar system is around 40 m, which is lower than most other remote sounding systems. This property makes the sodar especially suitable for the estimation of the top of the shallow nocturnal (stable) mixing layer. Climatology of the MLH from sodar at different locations has been studied in Lokoshchenko (2002) and Emeis and Türk (2004).
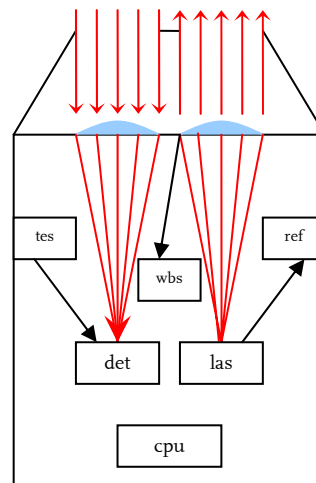
3   The LD-40 ceilometer

3.1   Instrument specifications

The Vaisala-Impulsphysik LD-40 ceilometer (Impulphysik, 1998) makes use of the LIDAR principle. The instrument transmits laser pulses into the atmosphere and measures the intensity of the backscattered signal as a function of time. The time interval between emission and reception determines the height at which the backscatter occurred. The backscatter profile as a function of height is the result of multiple laser emissions. Typically, 65000 pulses are emitted every 15 seconds. The backscatter profile provides information on the amount of particles that cause the backscatter, as a function of height.

The LD-40 (Figure 3.1) has a measurement range of 25 to 43000 ft (7.5 m to 13.6 km) and operates at a resolution of 25 ft (7.5 m). It uses laser diodes with 855 nm wavelength that are pulsed at a frequency of 6494 Hz. The pulse energy power is 1 µJ and pulse duration is 75 ns. A complete overview of the specifications is listed in Table 3.1.

Backscatter profiles are reported by the LD-40 every 15 seconds, together with the lowest three cloud bases (C1, C2 and C3), vertical visibility (VV), maximum range of detection (CX) and a precipitation index (PI). These additional parameters are derived from the backscatter profile by the internal LD-40 software (currently v3.5, as described in Supplement 1 to User Manual (Impulsphysik, 1999). The sensor features a reference detector and test laser to measure the power of the laser and the sensitivity of the detector, and adjust them if necessary. The window backscatter detector measures the backscatter as generated by pollution on the window of the sensor. If it exceeds certain thresholds, a warning or an error is reported.


FIGURE 3.1. Left: The Vaisala-Impulsphysik LD-40 ceilometer, mounted on a concrete base. Right: Schematic overview of operation of the LD-40, with: cpu (CPU), det (detector), las (laser), tes (test laser), wbs (detector for window backscatter), ref (reference detector). Adapted from Wauben et al. (2001).

The KNMI SIAM (Sensor Intelligent Adaptation Module) XC4 (Bijma, 1999) or DC4 (Bijma, 2006) polls the LD-40 every 12 seconds, which is the default sample interval in the KNMI synoptical network. The LD-40 sends the above-mentioned derived parameters in a so-called X1TA telegram. Only the C1, C2, C3, VV and CX parameters in the X1TA telegram are acquired by the SIAM and forwarded to the operational network of KNMI. These parameters are used in the cloud algorithm that determines the cloud layer heights and amounts. The LD-40 sends the backscatter profile in a so-called X1RD message with a length of 2048 bytes. This message is not processed by the SIAM, but it can be stored separately by a PC, which also provides a time stamp for the measurement. Because the LD-40 operates on a cycle of 15 seconds and the SIAM polls every 12 seconds, two identical X1RD messages will appear within every 5 messages (corresponding to 1 minute). Every byte of the backscatter profile gives a coded ASCII character with the backscatter value in the corresponding gate. 7200 profiles are stored in a daily KNMI format file, corresponding to the polling time of 12 seconds.

TABLE 3.1.   Specifications of the Vaisala-Impulsphysik LD-40 ceilometer (Adapted from: Impulsphysik, 1998).

Performance		Receiver	
Range	25 ft to 43000 ft (7.5 m to 13600 m)	Collector	Si-avalanche photo diode, gain controlled automatically
Resolution	25 ft (7.5 m)		
Accuracy (for solid targets)	± 25 ft (7.5 m)	**Optics**	
		Transmitter	Single lens system Focal length 500 mm Diameter 140 mm Divergence typically 1 mrad
Range gates	2048		
Measurement cycle	15 seconds	Receiver	
Output	Up to 3 cloud bases Maximum range of detection Vertical visibility Backscatter profile Instrument status information		Single lens system Focal length 500 mm Diameter 140 mm Divergence typically 1.2 mrad Filter 855 (±2) nm Half-value width 8.1 nm
Transmitter		**Other**	
Light emitter	Stacked diode, InGaAs (MOCVD)	Power supply	230 / 115 VAC +10% - 15%
Wavelength	855 nm	Power consumption	700 W max.
Peak power	20 W	I/O connections	Data: RS232/RS422/RS485/ modem Maintenance: RS 232
Pulse duration	75 ns		
Pulse repetition rate	6494 Hz		
		Dimensions	1260 x 444 x 404 mm
LASER safety	Eye-safe laser product Conforming to IEC 825/EN 60 825-1 from 07/94	Weight	40 kg

The backscatter profiles in the X1RD data telegram are coded as the natural logarithm of the measured power P in pW, multiplied with the squared height r in m: $\ln(Pr^2)$. The latter follows from the range correction that is applied to the backscatter values. In addition, P is the average power that is received per laser pulse during the measurement cycle of 15 seconds in which approximately 65000 pulses are emitted. The backscatter resolution is 0.2 (expressed in $\ln(Pr^2)$), and values are in the range from 10.1 to 22.7. An example of a backscatter profile measured by the LD-40 ceilometer in De Bilt is shown in Figure 3.2.
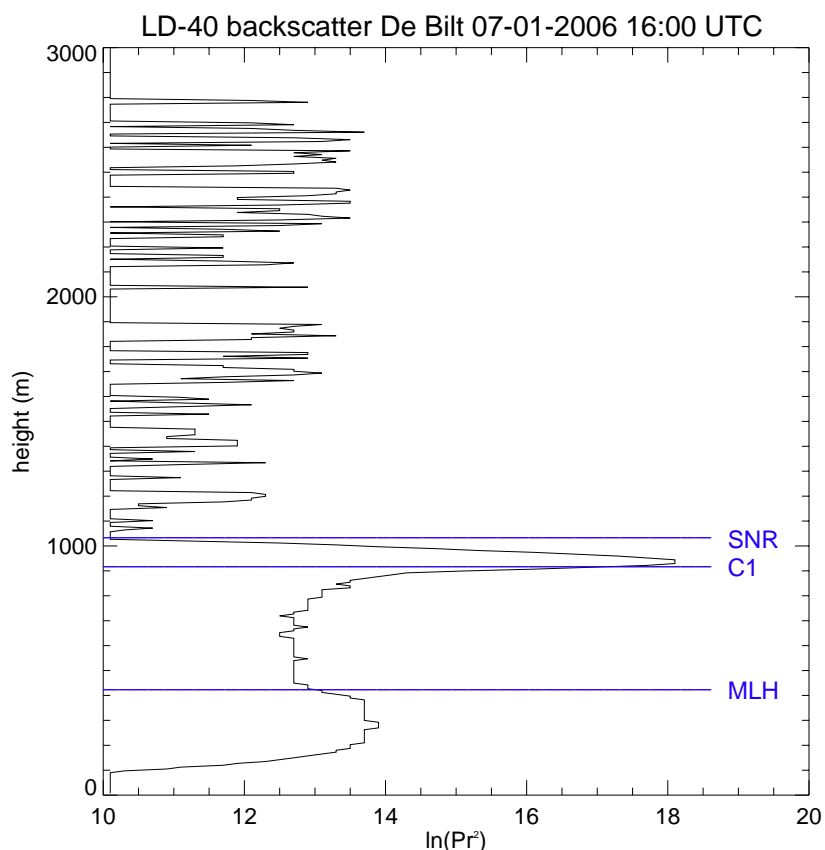
FIGURE 3.2. Backscatter profile for the LD-40 in De Bilt on January 7, 2006 16:00 UTC. Data are presented in $\ln(Pr^2)$, for the lowest 3 km of the atmosphere. Two significant structures in the backscatter signal are observed around 400 m and around 900 m, coinciding with the top of the mixing layer ('MLH') and a cloud base ('C1'), respectively. Above the cloud, the signal is below the SNR=1 threshold (see section 3.2.2).

3.2 Data preprocessing

3.2.1 Overlap correction

The LD-40 is a bi-axial system, hence the beams of the transmitter and receiver do not overlap completely in the lowest 1125 m. This is a disadvantage with respect to a co-axial (i.e. single lens) system, like e.g. the CT25K ceilometer. Up to 60 m the overlap of the LD-40 is zero, therefore it is not possible to extract any backscatter information from gates below this level. Any received signal below 60 m results from multiple scattering. Between 60 and 1125 m, the overlap increases to 1. The backscatter signal measured in this range has to be corrected for the incomplete overlap between transmit and receiver beam (Münkel and Räsänen, 2004). This is schematically presented in Figure 3.3.
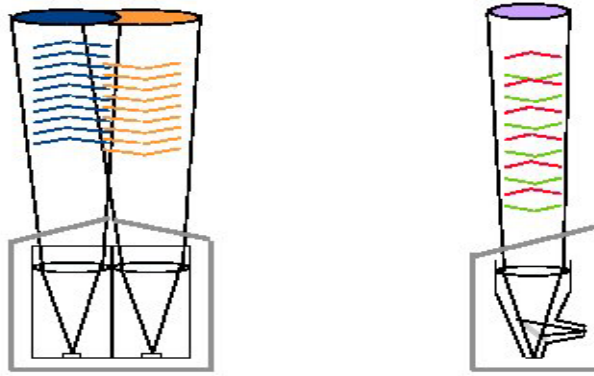
FIGURE 3.3. Left: bi-axial (e.g. LD-40) versus right: co-axial (e.g. CT25K, CL31) ceilometer design. For the bi-axial ceilometer the detected backscatter in the near-range domain is dominated by multiple scattering. An overlap correction is carried out on the signal in the lowest 1125 m (from: Münkel and Räsänen, 2004).

The average power P is already corrected for the incomplete overlap of the bi-axial ceilometer, but an additional overlap correction seemed necessary after inspection of several backscatter profiles. This was confirmed by the manufacturer and KNMI was provided with a modified overlap table for the gates between 0 and 1800 m. The maximum overlap height of 1800 m instead of 1125 m is a result of the overcorrection that is actually applied to the values of P in the X1RD telegram up to 1800 m. The Vaisala overlap correction profile for the LD-40 is presented in Figure 3.4.
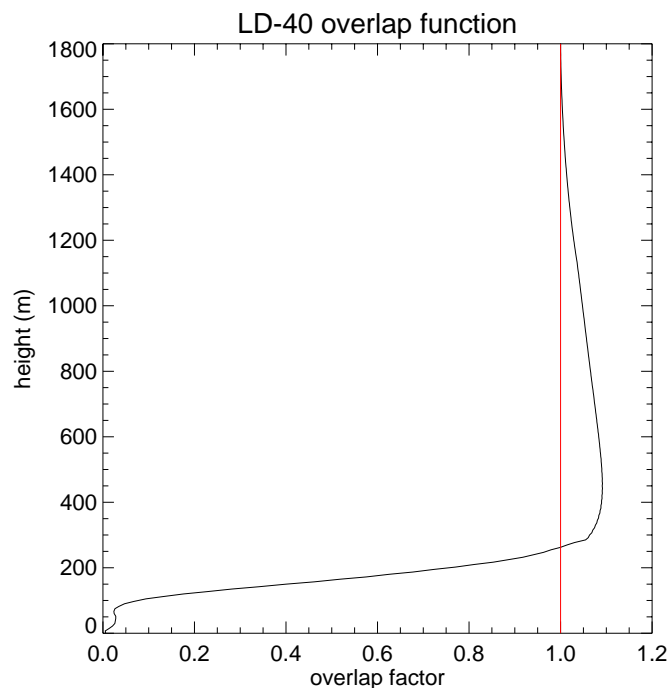
FIGURE 3.4. General overlap correction profile (black) for the LD-40 ceilometer and complete overlap representation (red) (Münkel, 2006; personal communication).

The overlap correction is applied on the values of P that are extracted from the $\ln(Pr^2)$ backscatter values. For each range gate up to 1800 m, the value of P is divided by the value in the corresponding range gate of the overlap profile. This means that the largest

corrections occur between 0 and 270 m, the region in which the overlap profile rapidly increases towards 1. The lowest possible value for $\ln(Pr^2)$ in the X1RD telegram of the KNMI LD-40 data format is 10.1. This value is reported for all range gates for which $\ln(Pr^2)$ is smaller than 10.2. The overlap correction is therefore only employed for gates in which the value for $\ln(Pr^2)$ is reported 10.3 or higher. Below 135 m, gates with a value of 10.1 are set to zero.

The overlap factor is larger than 1 for the ceilometer gates between 270 and 1792.5 m, which means that the value of P gets smaller after application of the overlap correction. In Appendix B, the general applicability of the standard overlap function to different ceilometers is discussed.

3.2.2 Signal-to-noise-ratio check

Only that part of the backscatter signal with a sufficiently high signal-to-noise-ratio (SNR) should be taken into account within the application of the MLH detection algorithm. When regions of low SNR values are considered, the MLH determination might get contaminated due to backscatter structures related to noise instead of atmospheric signals. For this purpose, a LD-40 SNR preprocessing is applied which is based on a procedure that was introduced within the Cloudnet project (Haeffelin, 2005; personal communication). This procedure ignores any points of the backscatter profile that are below a certain noise threshold value. The threshold value is derived from gates in the upper 3 km of the backscatter profile.

The background noise BN is computed as the average of backscattered power P for the range gates between 12 and 15 km (gates 1601 to 2000). The standard deviation σ_P of P over these 400 levels is calculated as well. The noise level is now defined as $BN + \sigma_P$, and the SNR is calculated as: $SNR = P/(BN + \sigma_P)$.

Backscatter values with a SNR lower than 1 and backscatter values equal to the minimum or maximum possible value for the logarithmic range corrected backscatter (10.1 and 22.7, respectively), are also assumed to be noise levels. Next, the SNR stop level h_{SNR} is determined as the lowest level at which the SNR<1 criterion has been satisfied 10 times or at which the backscatter signal shows a minimum (10.1) or maximum (22.7) value. The determination of the SNR stop level has a lower boundary of 150 m, because the lowest range gates are mostly truncated due to very low overlap (section 3.2.1). The SNR stop level is introduced to prevent the MLH algorithms from estimating mixing layer height in an unreliable region of the backscatter signal. Hence, MLH will not be determined beyond h_{SNR}.

3.3 Restrictions in MLH detection

Next, the lower boundary of the vertical domain is set to 90 m, whereas the upper boundary is set to 3000 m. The latter is considered to be an upper limit for boundary layer heights in The Netherlands.

Backscatter signals from other origin than aerosol are filtered out before the MLH algorithm is applied. The parameters derived by the internal Vaisala algorithm are used to

detect the occurrence of these disturbances. Firstly, the LD-40 MLH algorithms are not applied if the precipitation index PI exceeds a value of 1 (light precipitation). Furthermore, the vertical domain on which the algorithm is applied is constrained by the maximum value of the SNR stop level h_{SNR} (section 3.2), but also by the minimum values of first cloud base C1, the vertical visibility VV and the maximum range of detection CX within the MLH processing interval of 10 minutes. For PI, the maximum value within the 10 minute interval is considered.

4 Ceilometer MLH algorithms

4.1 Introduction

As discussed in chapter 2, two major types of algorithms exist for the determination of the mixing layer height from backscatter profiles measured by a lidar or ceilometer. Therefore two algorithms were assessed within this feasibility study. The first one, 'Peaks', is based on the analysis of the gradient and the variance of the backscatter profile, whereas the second one, 'Wavelet', uses the wavelet transform of the backscatter profile. Besides the quantities used for the MLH detection, averaging in height and time is a crucial step in these algorithms. In this chapter, the set up of both algorithms (averaging, used quantities, MLH detection) will be discussed.

It is important to note that the mixing layer height detection algorithm is in principle a pattern recognition problem. The basic assumption that is made is that the vertical distribution of aerosol can be used as a tracer for finding the boundaries. The absolute value of backscatter is not needed, because only the gradients in backscatter are considered. However, certain threshold values in terms of the internal backscatter units will be introduced in this chapter in order to enhance the reliability of the MLH estimation. The backscatter profiles used in the algorithms are in $\ln(Pr^2)$ units. This form is preferred in studies concerning aerosol layering, because its derivative then contains the extinction in a linear form (Martucci et al., 2005; Lammert and Bösenberg, 2006).

4.2 Peaks MLH algorithm

The Peaks algorithm is based on an algorithm originally developed by De Ruiter and Swart (1991). They used the algorithm for detection of the top of multiple aerosol layers from backscatter profiles measured by the RIVM 1064 nm backscatter lidar. The method is based on analysis of collocated minima of the backscatter gradient and maxima of the backscatter variance. The aerosol layer heights and the corresponding standard deviations are determined on a 4½ minute temporal resolution, together with the lowest cloud base.

4.2.1 Averaging

The Peaks algorithm developed here, is applied on the 10 minute averaged, range and overlap corrected backscatter profiles (in $\ln(Pr^2)$ units) within a vertical domain of 90 – 3000 m. These profiles are constructed from ten 1 minute range and overlap corrected backscatter profiles (in Pr^2) in the LD-40 X1RD telegram. This means that only one out of every five profiles is used, for computational reasons. However, no significant improvement is observed when profiles are used on a 12 second temporal resolution. Vertical averaging is carried out on a window size of 2 range gates (15 m). Furthermore, a linear smoothing of the $\ln(Pr^2)$ profile is applied on a range of 135 m (+/- 4 levels). The averaging and smoothing steps are required to eliminate small-scale features that may lead to faulty MLH detections.

4.2.2 Variance computation

The 1 minute range and overlap corrected backscatter $B(i, j)$, in $\ln(Pr^2)$ units, is now introduced, as retrieved from the LD-40 X1RD telegram. In this quantity, i denotes the

time index, which is between 1 and 10 with a step width of 1 minute. The index j denotes the height index, which is between 6 and 200 with a step width of 15 m. The backscatter time variance $\sigma_B^2(j)$ is computed at each height from the 10 profiles in the interval as:

$$\sigma_B^2(j) = \frac{1}{10} \sum_{i=1}^{10} (B(i,j) - \overline{B}(j))^2$$

where $\overline{B}(j)$ denotes the 10 minute vertically averaged backscatter for the jth range gate. A normalisation of the variance is subsequently carried out by dividing $\sigma_B^2(j)$ by $\overline{B}^2(j)$, resulting in $\overline{\sigma}_B^2(j)$.

As noise is by definition very strongly varying within a time interval, it also contributes for a large part to the variance. Although a check on SNR has been introduced, that will be used to constrain the vertical domain of the algorithm, the increasing noise with height causes $\overline{\sigma}_B^2(j)$ to increase as well. The Peaks algorithm will be mainly dependent on a gradient criterion (section 4.2.3 and 4.2.4), due to these instrumental limitations. In addition, clouds enhance the vertical profile of backscatter variance to a large extent. Compared with the variance caused by varying backscatter at the top of the mixing layer, this contribution is often even dominating.

4.2.3 Gradient calculation

The backscatter gradient at the jth level of the backscatter profile is computed as:

$$\frac{\partial \overline{B}}{\partial z}(j) = \left(\frac{\overline{B}_s(j+1) - \overline{B}_s(j-1)}{z(j+1) - z(j-1)} + \frac{\overline{B}_s(j+2) - \overline{B}_s(j-2)}{z(j+2) - z(j-2)} \right) / 2$$

where $\overline{B}_s(j)$ denotes the 10 minute vertically averaged and smoothed backscatter. Furthermore, $z(j)$ denotes the height of this level.

4.2.4 MLH detection

The backscatter variance is tested on the presence of a local maximum by comparing it with the window-averaged value. The window-averaged variance profile is calculated on a window size that increases with height, adopted from the original RIVM algorithm (De Ruiter and Swart, 1991). This choice is motivated by the decreasing SNR with increasing height. The window sizes used are listed in Table 4.1. A significant local maximum is assumed at a level at which the backscatter variance exceeds the window-averaged value.

TABLE 4.1 Overview of used window sizes for the averaging of backscatter variance.

| range	window size
0 m − 375 m	45 m (+/- 1 levels)
375 m − 750 m	75 m (+/- 2 levels)
750 m − 1500 m	105 m (+/- 3 levels)
1500 m − 3000 m	135 m (+/- 4 levels)

The mean backscatter gradient is computed for the vertical domain between 90 and 3000 m to test the significance of the backscatter gradient minima. It is computed as the average of all gates with a negative backscatter gradient up to the first cloud base C1. The latter limit is chosen because of the dominating effect of a cloud layer on the backscatter signal. A local minimum in backscatter gradient is significant if it has a smaller value than 1.2 times the mean backscatter gradient. Furthermore, no MLH is detected if the mean backscatter gradient that is computed, exceeds -0.0011. The structures in aerosol which are present in these cases are assumed to be too weakly pronounced. Finally, the mixing layer height is determined as the lowest level at which a significant local minimum in the backscatter gradient is accompanied by a significant local maximum in backscatter variance, within a bandwidth of 165 m (+/- 5 levels).

The Peaks algorithm steps summarised:
- The original 1 minute range and overlap corrected LD-40 backscatter profiles (in Pr^2) are averaged over 10 minutes in time and over 2 gates in the vertical (15 m resolution), followed by a linear vertical smoothing of the averaged profile (in $\ln(Pr^2)$) over 135 m (+/- 4 levels).
- The vertical domain under consideration ranges between 90 and 3000 m, with an upper boundary, if below 3000 m, determined by the minimum of the lowest value of cloud base C1, vertical visibility VV and the maximum range of detection CX and the highest value of the SNR<1 height in the 10 minute interval.
- The backscatter gradient profile and the mean backscatter gradient (up to first cloud base) are calculated, as well as the backscatter time variance and window-averaged backscatter time variance.
- Mixing layer height is determined as the lowest level at which the backscatter gradient is smaller than 1.2 times the mean backscatter gradient, if the backscatter variance exceeds its window-averaged value, within a bandwidth of 165 m. No MLH is detected if the mean backscatter gradient that is computed, exceeds -0.0011.

An example of the development of a convective mixing layer in De Bilt on July 27, 2002, is shown in Figure 4.1. The backscatter profiles of 06, 08, 10 and 12 UTC clearly show an increasing mixing layer height in time, within the mixing layer a fairly uniform and high aerosol load is observed. Note also the increasing height at which the corresponding variance shows a significant increase, which seems to be correlated to the detected mixing layer height in the backscatter profile. This height also generally coincides to a large extent with the transition to the noisy part of the backscatter profile. The large contribution of noise to the variance is indicated as well by the increasing profile around the MLH, whereas the variance within the mixing layer itself is very small. Values for the SNR<1 height corresponding to the four profiles are 1004 m, 577 m, 772 m and 997 m, respectively.
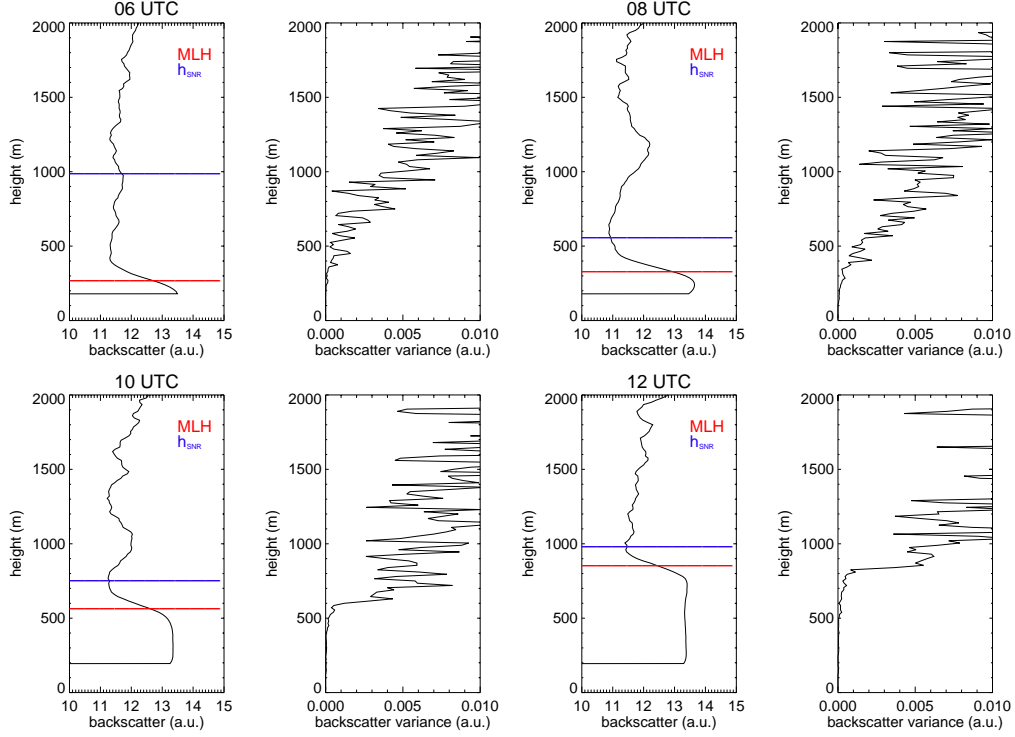
FIGURE 4.1 Backscatter and normalised backscatter variance profiles for De Bilt on July 27, 2002 at 06, 08, 10 and 12 UTC. Backscatter profiles are based on 10 minute average backscatter data from 10 distinct 1 minute profiles and include vertical averaging over 15 m and linear vertical smoothing over 135 m. Peaks MLH and the SNR stop level h_{SNR} are presented by the red and blue horizontal lines, respectively.

4.3　Wavelet MLH algorithm

The use of wavelets for the detection of mixing layer height from backscatter profiles from ground based and aircraft mounted remote sensing measurements has gained a great amount of popularity during the last years (section 2.3.1). In this study, the Haar wavelet transform is used, which is a simple but powerful gradient locator.

4.3.1　Wavelet theory

The Haar wavelet (or step) function (Figure 4.2) is defined as:

$$
h\left(\frac{z-b}{a}\right) = \begin{cases} 1 : b - \dfrac{a}{2} \le z < b \\ -1 : b < z \le b + \dfrac{a}{2} \\ 0 : elsewhere \end{cases}
$$

where z denotes the height for our application. The dilation (width) of the wavelet is described by a, while the translation (location at which the wavelet is centered) is given by b. Note that the wavelet function is only defined on the interval $z = [z_b, z_t]$, with the bottom height $z_b = 90 + a/2$ [in m] and the top height $z_t = \min(3000 - a/2, Cl, VV, CX, h_{SNR})$ [in m].

26
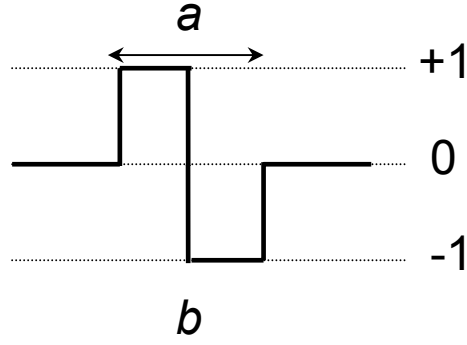
FIGURE 4.2 A representation of the Haar wavelet function, with dilation *a* and translation *b*.

The localised transform delivers the wavelet power spectrum coefficients $W_B(a,b)$, calculated as:

$$W_B(a,b) = a^{-1} \int_{z_b}^{z_t} B(z) h\left(\frac{z-b}{a}\right) dz$$

which can be interpreted as the convolution of the backscatter profile $B(z)$ and the Haar wavelet function, integrated between the bottom and top altitudes z_b and z_t of $B(z)$. The parameter a^{-1} denotes the corresponding normalisation factor.

Positive values of $W_B(a,b)$ coincide with levels at which the backscatter profile is positively correlated with the Haar function, i.e. the backscatter signal shows a strong decrease with increasing height. They are typically observed at the top of an aerosol layer. The highest values of $W_B(a,b)$ are generally found at height levels for which the strong decrease in backscatter is vertically spread over the size of the dilation under consideration. Vice versa, negative values of $W_B(a,b)$ indicate an anticorrelation of the backscatter profile with the Haar function for the corresponding dilation. This means that a strong increase in backscatter is observed at the corresponding height, which occurs most likely around cloud base or at the lower boundary of an aerosol layer.

To investigate the contribution of the different dilations within the wavelet transform, the global wavelet spectrum $D^2(a)$ is introduced:

$$D^2(a) = \int_{z_b}^{z_t} [W_B(a,b)]^2 \, db$$

The global wavelet spectrum quantifies the contribution of each dilation for the total vertical domain under consideration. However, it is not used in the Wavelet algorithm.

In the Wavelet algorithm the scale averaged power spectrum $\overline{W_B}(b)$ is used to detect aerosol tops in the ceilometer backscatter profile and is defined as:

$$\overline{W_B}(b) = \frac{1}{N_a} \sum_{a_{min}}^{a_{max}} W_B(a,b)$$

where a_{min} and a_{max} denote the minimum and maximum dilation which are taken into account and N_a is the number of dilations.

4.3.2 Averaging

The Wavelet algorithm is applied to the 10 minute averaged range and overlap corrected backscatter profile (in $\ln(\text{Pr}^2)$ units) within a vertical domain of 90 – 3000 m. This averaged profile is constructed from ten 1 minute backscatter profiles (in Pr^2) in the LD-40 X1RD telegram. This means that one out of every five profiles is used.

4.3.3 MLH detection

The top of at the most two significant aerosol layers is detected within the Wavelet algorithm. This gives the opportunity to trigger the mixing layer height as well as a secondary aerosol layer top, like for example the top of an advected aerosol layer or the residual layer. These layer heights are hereafter called MLH1 and MLH2 respectively.

The MLH detection method presented here uses the scale averaged power spectrum profile $\overline{W_B}(b)$, with 24 dilations between 15 and 360 m and step size 15 m. The step size used is the smallest possible, i.e. 2 range gates. For each range gate up to the upper boundary of the vertical domain (as determined by the minimum of the lowest value of C1, VV, CX and the highest value of h_{SNR}) the average value $\overline{W_B}(b)$ is computed from the contributions of each available single dilation for that corresponding height. Note that for an increasing dilation, the level at which $W_B(a,b)$ obtains a value for the first time also increases due to the decreasing vertical extent for which the wavelet function is defined. If a wavelet does not fit due to its dilation size, the contribution of this dilation is omitted in the calculation of the scale averaged power spectrum profile.

The top of the first layer, MLH1, is detected at the lowest level at which the scale averaged power spectrum $\overline{W_B}(b)$ shows a local maximum, exceeding a threshold value of 0.1. This threshold value is empirically chosen, based on the analysis of several cases both with well and less clearly pronounced mixing layer tops. MLH2 is optionally determined in the height range between MLH1 and the upper boundary of detection. A valid MLH2 is detected at the level with the strongest local maximum of $\overline{W_B}(b)$ provided that this maximum is larger than the value of $\overline{W_B}(b)$ at MLH1.

The Wavelet algorithm steps summarised:
- The original 1 minute LD-40 range and overlap corrected backscatter profiles (in Pr^2) are averaged over 10 minutes in time. The original vertical resolution of 7.5 m is kept.
- The vertical domain under consideration ranges between 90 and 3000 m, with an upper boundary, if below 3000 m, determined by the minimum of the lowest value of cloud base C1, vertical visibility VV and the maximum range of detection CX and the highest value of the SNR<1 height in the 10 minute interval.
- The scale averaged power spectrum $\overline{W_B}(b)$ is calculated from the 10 minutes averaged $\ln(\text{Pr}^2)$ profile on the valid vertical domain, by averaging all wavelet power spectrum coefficients $W_B(a,b)$ in this domain for 24 dilations between 15 and 360 m.

- Two significant aerosol layer tops are detected. MLH1 is determined as the lowest level at which $\overline{W_B}(b)$ exceeds a threshold of 0.1. MLH2 is estimated at the level of the strongest maximum in $\overline{W_B}(b)$ between MLH1 and the upper boundary of detection, provided that the value of $\overline{W_B}(b)$ is larger than at the MLH1 level.

4.3.3   Examples

An artificial backscatter profile is created to illustrate the principle of the wavelet transform, see Figure 4.3. Two aerosol layer tops are simulated by means of a region with strongly decreasing backscatter, between 450 and 600 m and between 750 and 825 m. Both of them have an absolute jump in backscatter (a.u.) of -2.5. An artificial cloud backscatter structure is also incorporated within the profile between 938 and 1020 m. In the wavelet analysis, dilations between 15 (2 range gates) and 360 m (48 range gates) are considered. It should be mentioned that the analysis presented here is not terminated at an upper boundary, determined by cloud base height or other significant levels in the backscatter profile.

The expected behavior of the wavelet power for the strongly decreasing and increasing regions in the backscatter profile is observed. The top of the aerosol layers coincide with an area with positive values of $W_B(a,b)$, while the region with increasing backscatter ('cloud base') coincides with significant minima in $W_B(a,b)$. Note the merging process that occurs for the wavelet power at dilations larger than approximately 300 m. This is caused by the fact that wider wavelet functions take into account more vertical levels. Therefore the wavelet power will be enhanced if the dilation is approximately as large as the height interval that separates two aerosol layers. On the other hand, the wavelet power resulting from the second aerosol layer also interferes with the negative power associated with the increasing backscatter due to the cloud, which lowers the wavelet power above the 2nd mixing layer top for dilations from around 200 m.

When the scale-average height series for different regimes of dilations is considered (smaller than 100 m, larger than 300 m, and the average of 15 – 360 m), it can be noted that a relatively large contribution to the wavelet power for the upper aerosol layer top MLH2 comes from dilations smaller than 100 m. This is caused by the vertical extent of 75 m, against 150 m for the top of the lower aerosol layer. The above mentioned merging process is also visible in the enhanced profile of wavelet power for dilations larger than 300 m, and in the average profile. Because all of the introduced layers are separated more than 100 m from each other, the profile for dilations smaller than 100 m only obtains values around the increasing and decreasing regions of the backscatter profile, whereas it is zero in between. The black triangles on the left and the right of the wavelet power spectrum in Figure 4.3, are caused by the boundaries introduced by the limitation that a Haar wavelet with dilation 'a' is only defined on the height interval $z = \left[90 + a/2, 3000 - a/2 \right]$.
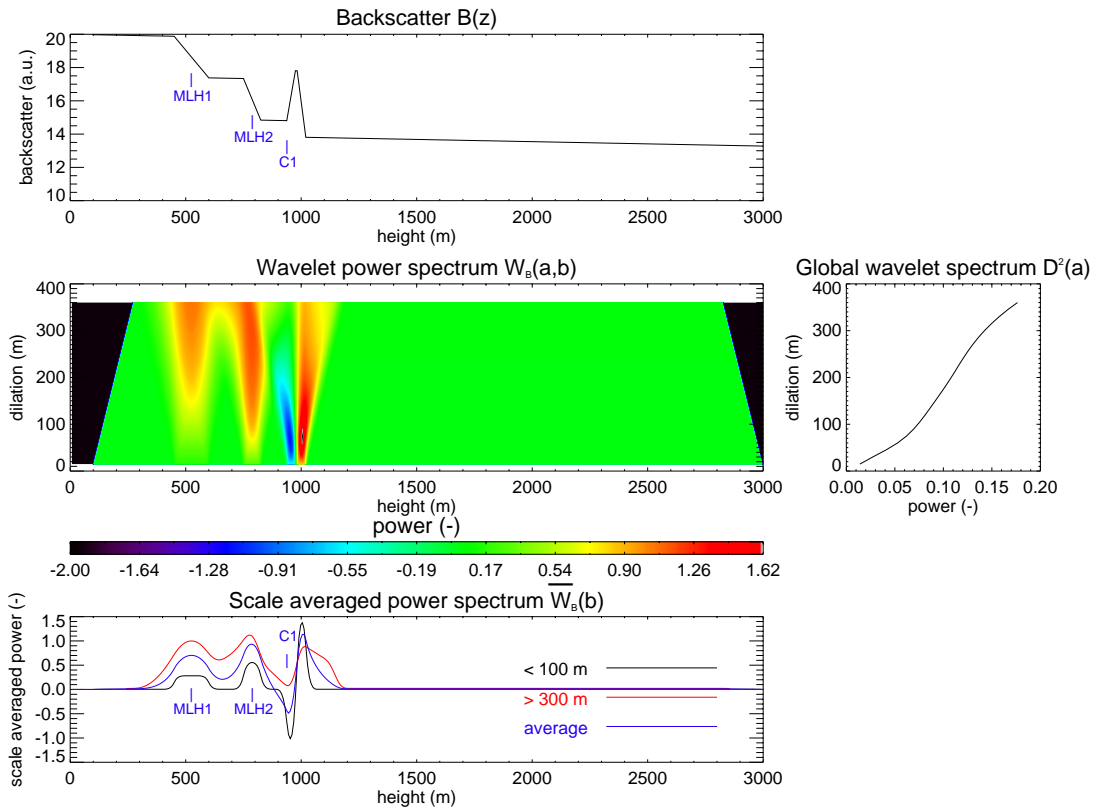
FIGURE 4.3 Wavelet analysis result for an artificial backscatter profile (upper panel). The Wavelet power spectrum (middle left) presents the wavelet power for the complete backscatter profile for all dilations. The global wavelet spectrum (middle right) sums these coefficients in height and shows the contribution of each dilation. The average contribution to wavelet power in height is presented in the lower figure (for dilations smaller than 100 m, larger than 300 m, and the average contribution of all 24 dilations between 15 and 360 m).

Figure 4.4 shows the wavelet analysis of a 10 minute averaged backscatter profile (in $\ln(Pr^2)$) for De Bilt at 10:00 UTC on August 29, 2005. The first thing to note is the large amount of noise in the measured profile compared to the noiseless artificial profile. Hence, the scale averaged power spectrum for dilations smaller than 100 m is strongly varying in height, as seen especially above 750 m. This is also expressed in the relatively large contribution of small dilations in the graph of $D^2(a)$.

Cloud base C1 as well as vertical visibility VV and maximum range of detection CX are all reported higher than 3000 m, which causes no further restrictions to occur for this case. The SNR stop level is located at 1469 m for this profile, therefore the calculation of $W_B(a,b)$ is terminated at the level corresponding to a height of 1463 m. As seen in the height series of $\overline{W_B}(b)$, the average for all dilations shows several significant local maxima, with respect to the threshold value of 0.1. The Wavelet algorithm estimates MLH1 at 518 m, whereas MLH2 is estimated at 1365 m. The latter coincides with the top of the residual layer.
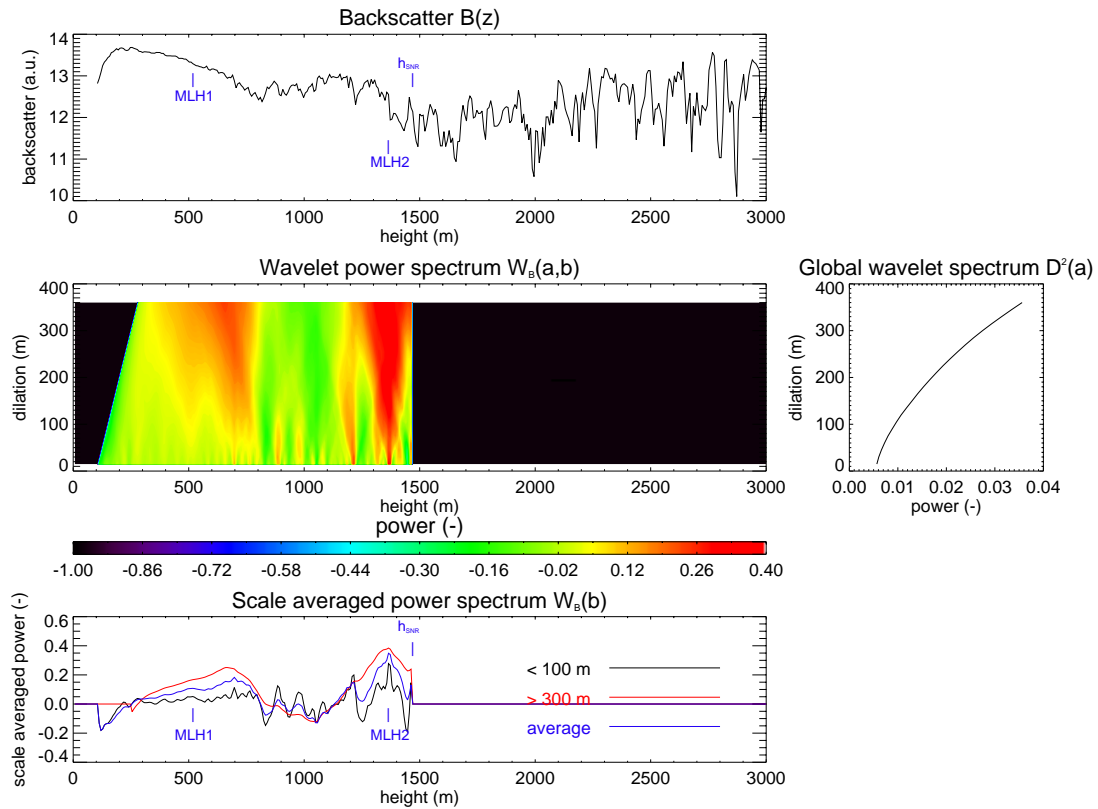
FIGURE 4.4 Same as Figure 4.3, but for the 10 minute averaged LD-40 backscatter profile measured in De Bilt at 10:00 UTC on August 29, 2005.

4.4 Quality index

A quality index is introduced to distinguish between detections of the top of well-pronounced and more doubtful mixing layers respectively. The magnitude of the jump in backscatter (in $\ln(Pr^2)$ units), centered on the MLH level is used as a measure for the quality of the detection. More specifically, the difference between the average backscatter from 150 m below MLH up to the last level below MLH (B_d) and the average backscatter from the first level above MLH up to 150 m above MLH (B_u) is used as a quantity for the quality index. If a MLH is found within the first 150 m above the lower boundary or the last 150 m below the SNR stop level, the corresponding value is calculated from a lower number of range gates. The quality index is divided into four classes, as presented in Table 4.2.

TABLE 4.2. Classification of the used quality indices for mixing layer height detection.

color code	trigger mechanism	description
White	No detection of MLH	No MLH detection
Red	$B_d - B_u < 0.25$	Poor MLH detection
Yellow	$0.25 \leq B_d - B_u < 0.50$	Weak MLH detection
Green	$B_d - B_u \geq 0.50$	Good MLH detection

The threshold values for the different quality index classes are to some extent chosen arbitrarily, and are estimated by assessing cases with transitions between well-

pronounced and ambiguous mixing layer heights. A disadvantage of this method is that the quality index of a MLH with another aerosol layer on top (either advected or residual) or closely below a cloud layer will be significantly suppressed due to the relatively high backscatter that is measured beyond this MLH. This may lead to the rejection of detections which are labeled unambiguous as inferred from a visual inspection of the backscatter profile.
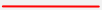
5 Case studies

5.1 Introduction

In this chapter a number of cases are discussed, representing a selection of typical atmospheric conditions that are found within the data set of the LD-40 ceilometer at the test field in De Bilt and the experimental site in Cabauw. A comparison between the two MLH algorithms is made for these cases. For several cases, mixing layer height estimates by radiosonde, wind profiler, RIVM lidar and the regional climate model RACMO (section 5.5) are incorporated. This provides some insight in the differences that occur in MLH determination between different types of measurement platforms. The cases are illustrated by means of contour plots, in which the LD-40 backscatter (in $\ln(\text{Pr}^2)$) is plotted on a fixed scale between 10.1 and 14.5. Table 5.1 lists the legend used for the variables in these plots.

TABLE 5.1. Legend of the backscatter contour plots in this chapter.

|	
X	LD-40 first cloud base C_1
———	LD-40 SNR<1 height
•	LD-40 MLH 1 Wavelet algorithm
•	LD-40 MLH 2 Wavelet algorithm
•	LD-40 MLH Peaks algorithm
Δ	Radiosonde MLH Richardson bulk method
Δ	Radiosonde MLH parcel method
□ or □	Wind profiler MLH
•	RIVM lidar first MLH
———	RACMO 1 boundary layer height
– – – –	RACMO 2 boundary layer height

5.2 Typical conditions

5.2.1 Convective mixing layer with clouds: Cabauw – July 27, 2002

A convective mixing layer was observed at Cabauw on July 27, 2002. This day has been used in a study on boundary layer budgets of trace gases, as a part of the RECAB campaign (e.g. De Arellano et al., 2004) in which KNMI participated. Figure 5.1 shows the aerosol backscatter that was measured by the LD-40, as well as values of the mixing layer height estimated from the LD-40 backscatter data and the wind profiler radar backscatter data. A strong decrease in aerosol backscatter is seen at the sharp interface between the mixing layer and the free atmosphere, especially during the period 02 – 14 UTC. Higher values of ceilometer backscatter are observed above the SNR stop level during daytime, this is generally caused by the enhanced amount of noise for this period.

Results from both methods for LD-40 MLH determination follow each other very closely during the largest part of the day. The development of the mixing layer can easily be observed from the LD-40 data, but is disturbed at 14 UTC by the presence of cumulus clouds, which cause the algorithms to stop processing the backscatter profiles at the

height of the first cloud base. Around 17:30 UTC a new aerosol layer is observed, which extends between 200 and 500 m during the evening. This layer is nearly always triggered by the Wavelet algorithm, whereas several of the coinciding Peaks MLH estimations are significantly higher. The occurrence of this new aerosol layer coincides with a change in wind direction in the wind profiler measurements (Figure 5.2). The prevailing southerly to southwesterly winds that are observed in the mixing layer during the day suddenly turn to a northerly direction between 17 and 18 UTC. This change marks the advection of an air mass containing aerosol from another source area to Cabauw, which causes the enhanced backscatter in the lowest 500 m during the evening period.
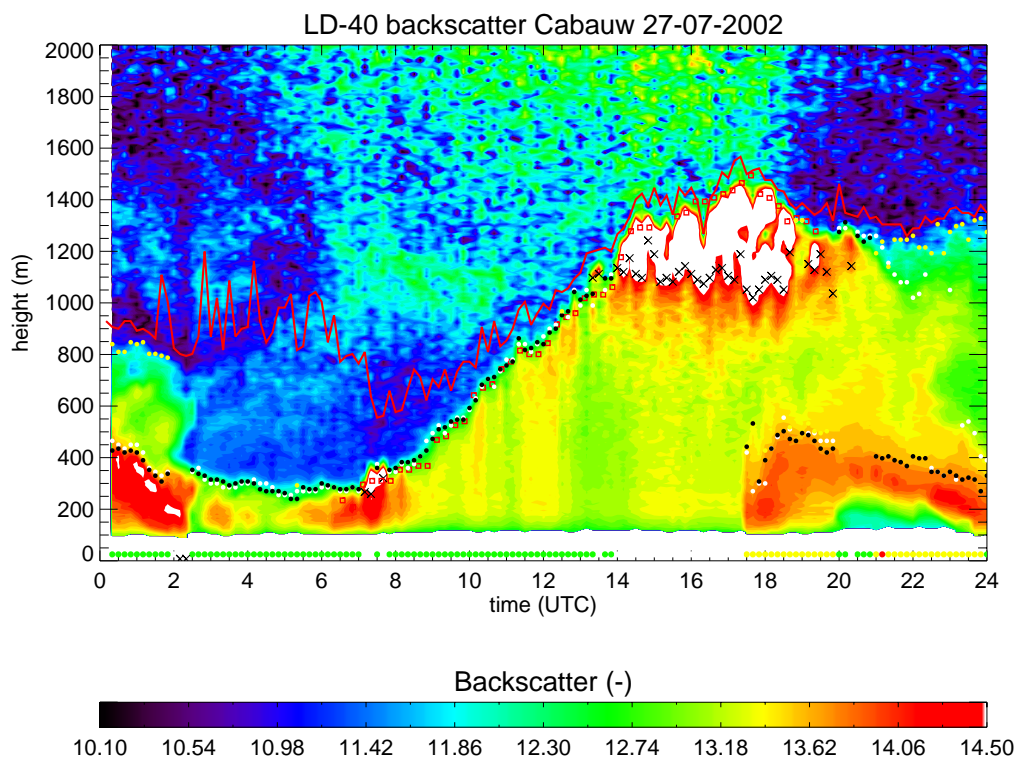
FIGURE 5.1. LD-40 backscatter contour plot (ln(Pr²) units) for Cabauw on July 27, 2002. The legend of included variables is presented in Table 5.1. The quality indices of Wavelet MLH1 detections are indicated below the backscatter contours, using the color code given in Table 4.2.

A significant residual layer persists around 1200 m during the evening above the lower aerosol layer (Figure 5.1). Between 20 and 21 UTC, both Peaks MLH and Wavelet MLH1 are elevated towards this residual layer because the backscatter profiles at the top of this lower aerosol layer do not meet the thresholds of the algorithms. Radiosonde measurements are not available for this day. The MLH estimates from the wind profiler data in Cabauw however show a good correlation with the heights detected by the LD-40. During the period 06 – 14 UTC the difference between the two instruments is around 75 m at most. The quality index of the Wavelet MLH1 is good for the whole day, except for one point (21:10 UTC), which demonstrates a 'Poor' (=red) quality index (section 4.4). The detected height of the lower aerosol layer during the evening has intermediate ('Weak') quality.
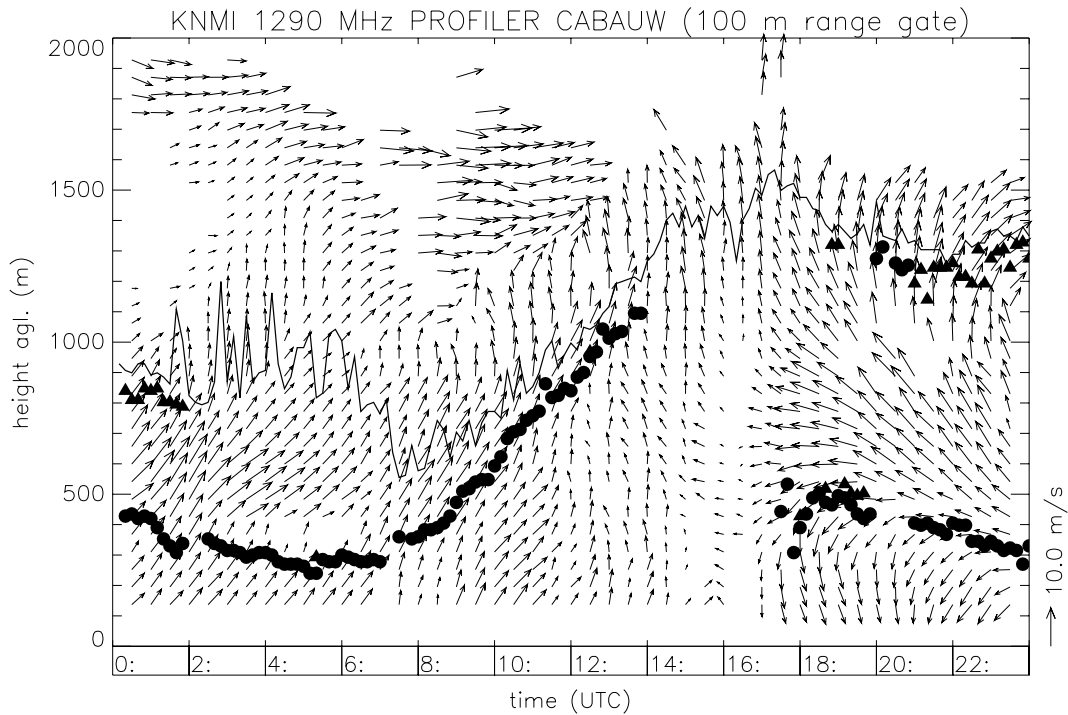
FIGURE 5.2. Wind vectors derived from wind profiler measurements at Cabauw on July 27, 2002. Dots denote Wavelet MLH1, triangles denote Wavelet MLH2 and the SNR stop level is indicated with the black solid line.
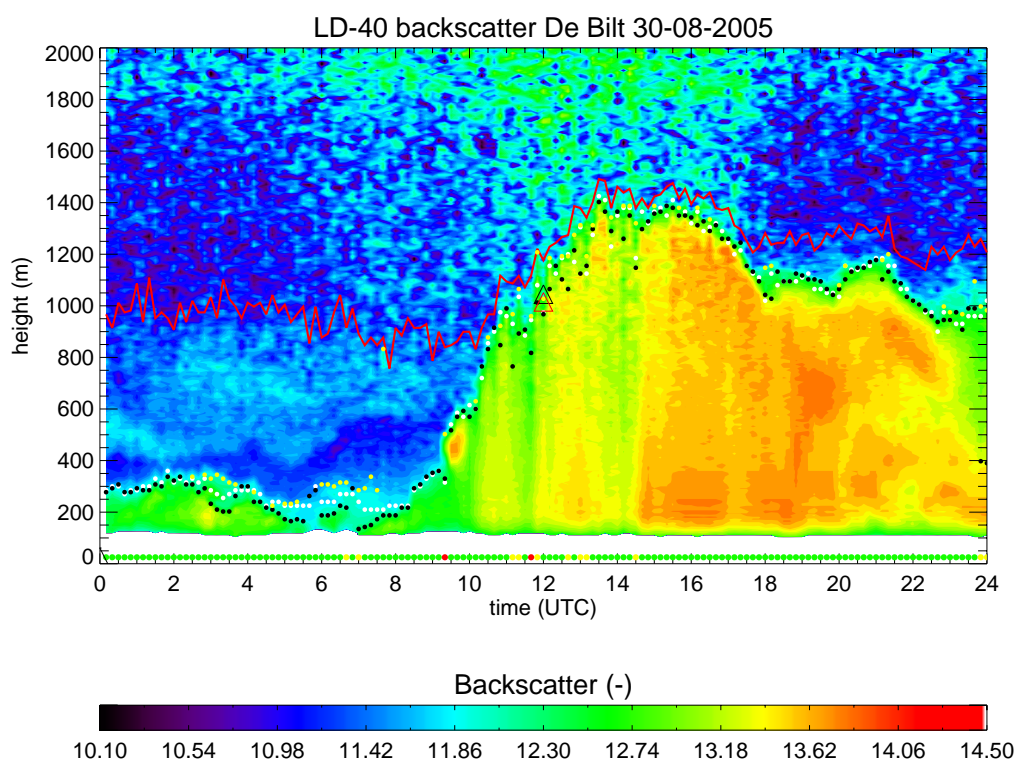
5.2.2 Strong reflecting nighttime residual layer: De Bilt – August 30, 2005

Figure 5.3 shows the backscatter contours and MLH estimates for De Bilt on August 30, 2005. Prevailing cloud-free conditions are observed for this day, which enhances the development of a pronounced mixing layer reaching heights up to 1400 m. The Wavelet MLH1 estimate is generally located lower than the Peaks MLH estimate for this day, and outliers in the MLH1 time series during the day period mostly coincide with a 'Weak' (=yellow) quality index. The 00 UTC radiosonde estimate (Richardson bulk) of MLH is reported at 25 m, which indicates the presence of a very shallow nocturnal mixing layer. Due to the lower boundary of 90 m of the algorithms, it is not possible to detect this shallow MLH correctly.

During the period 00 – 09 UTC a shallow aerosol layer is observed with the top between 135 and 360 m. The estimates made by the Peaks and Wavelet algorithms clearly diverge here up to 100 m with respect to each other, possibly due to the different averaging steps that are carried out in height (see section 4.2 and 4.3). The enhanced backscatter that is observed above this aerosol layer coincides with a layer of increased relative humidity as observed in the 00 UTC radiosonde profile (not shown). A gradual decrease in backscatter on a large vertical extent is seen for most of the profiles during the nighttime period, which might also explain the difference in MLH detections for the two algorithms. This phenomenon is also illustrated by means of the 06 UTC backscatter profile in Figure 5.4.

The growth of the mixing layer starts at approximately 07 UTC and reaches its highest top around 14 UTC. It is especially during this phase that a large variability between

MLH1s at consecutive time steps is noted for both algorithms. Because of the turbulent behavior inside the mixing layer a patchy pattern in aerosol backscatter is observed for the growth phase, which most likely causes this temporal variability of mixing layer height.

FIGURE 5.3. Same as Figure 5.1, but for De Bilt on August 30, 2005.

Where one would expect the mixing layer to decay some time before sunset, the top of a strong reflecting persistent residual layer is detected during the evening of August 30. Apparently, there is no reason for the Peaks and Wavelet algorithms to detect an aerosol layer top below 900 m until the end of the day, just before 24 UTC. This might be a direct consequence of the increasing aerosol backscatter which sets in the mixing layer around 14:30 UTC, and which causes other structures in backscatter that are caused by the thermodynamic behavior of the boundary layer to become less pronounced. Hence, the top of the decaying mixing layer is not detectable for this case. The 18 UTC backscatter profile in Figure 5.4 shows a structure around 300 m, but the algorithms are not triggered on a decrease of this extent.

The MLH estimates of both algorithms differ 100 to 150 m to the ones estimated from the radiosonde measurements in De Bilt. For the 12 UTC sounding, the Parcel method and Richardson bulk method report 1015 m and 1040 m respectively, whereas the Peaks method estimates MLH at 885 m and the Wavelet method reports a value of MLH1 of 908 m. The ceilometer estimates are taken at 11:30 UTC, the nearest time step to the launch of the radiosonde, at 11:27 UTC. However, the temporal variability of the ceilometer MLH estimates between 11 and 12 UTC is high. This is obviously related to an area of lower backscatter which is clearly observed in the backscatter contours for this time interval.
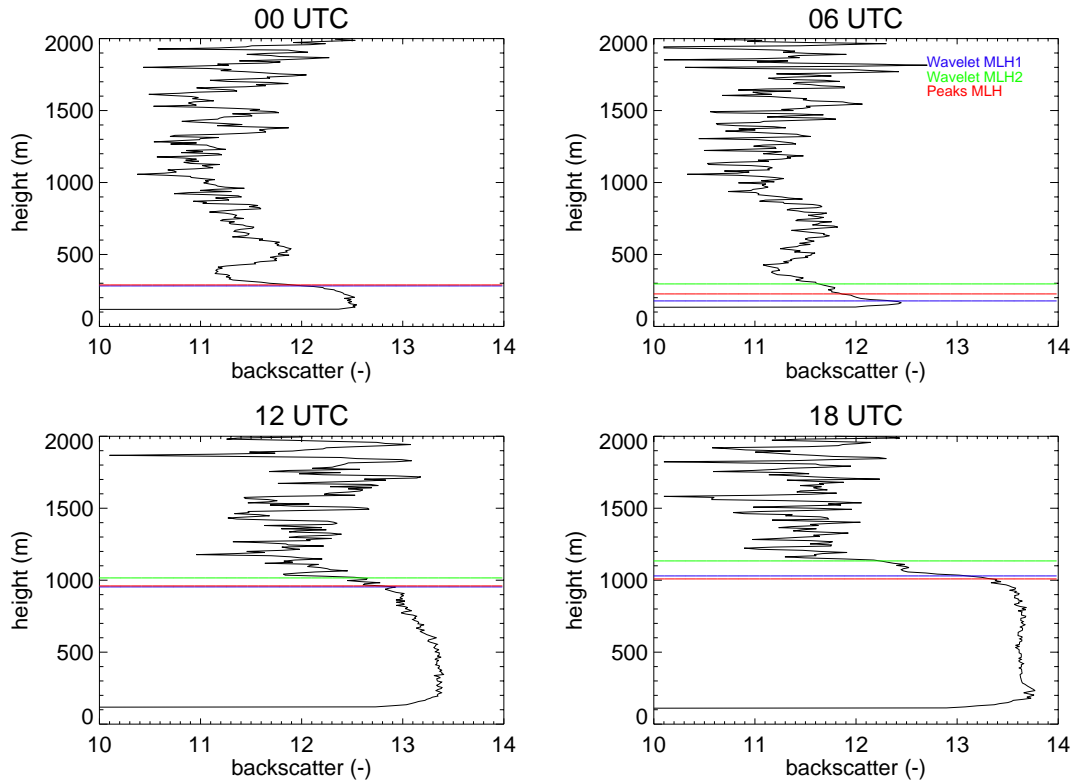
FIGURE 5.4. LD-40 backscatter profiles (ln(Pr²) units) for De Bilt on August 30, 2005, at 00, 06, 12 and 18 UTC. The height of the Peaks and Wavelet MLH determinations are reported by the horizontal lines.

5.2.3 Deep mixing layer: De Bilt – July 19, 2003

A deep convective mixing layer, topped with clouds as from 10:45 UTC, was observed in De Bilt on July 19, 2003. Backscatter contours and MLH estimates for this day are given in Figure 5.5. The backscatter data show no clear distinction between aerosol layers and the free atmosphere, except for the period until approximately 10 UTC. A high variability with height in the backscatter signal is present afterwards, resulting in a large temporal variation of MLH estimates of mainly 'Poor' (=red) quality.

The Richardson bulk method applied to the radiosonde profiles at 00 UTC reports a MLH of 35 m. Again, the LD-40 is not capable of detecting such a shallow layer. Instead, a relatively shallow but variable mixing layer top is detected by the Peaks and Wavelet algorithms for the period between 00 and 06 UTC, after which the incoming solar radiation causes the convective mixing layer to build up quickly. The Peaks MLH and Wavelet MLH1 are capable of tracing the top of the developing mixing layer correctly only until 10 UTC. Whereas the radiosonde Parcel and Richardson bulk methods and the wind profiler at Cabauw both report at 12 UTC a mixing layer height positioned around the clouds which are present around 2100 m, the aerosol backscatter signal measured by the LD-40 shows a lot of noise in the mixing layer. The SNR<1 height is located around 1200 m for the period around noon, which implies that no useful backscatter signal can be expected around the level at which the other instruments estimate the 'correct' MLH. Note that the wind profiler is operated at Cabauw, while radiosonde and LD-40 estimates are based on measurements carried out approximately 30 km to the northeast in De Bilt.

Nevertheless, the wind profiler estimates are believed to be representative for De Bilt for this situation.
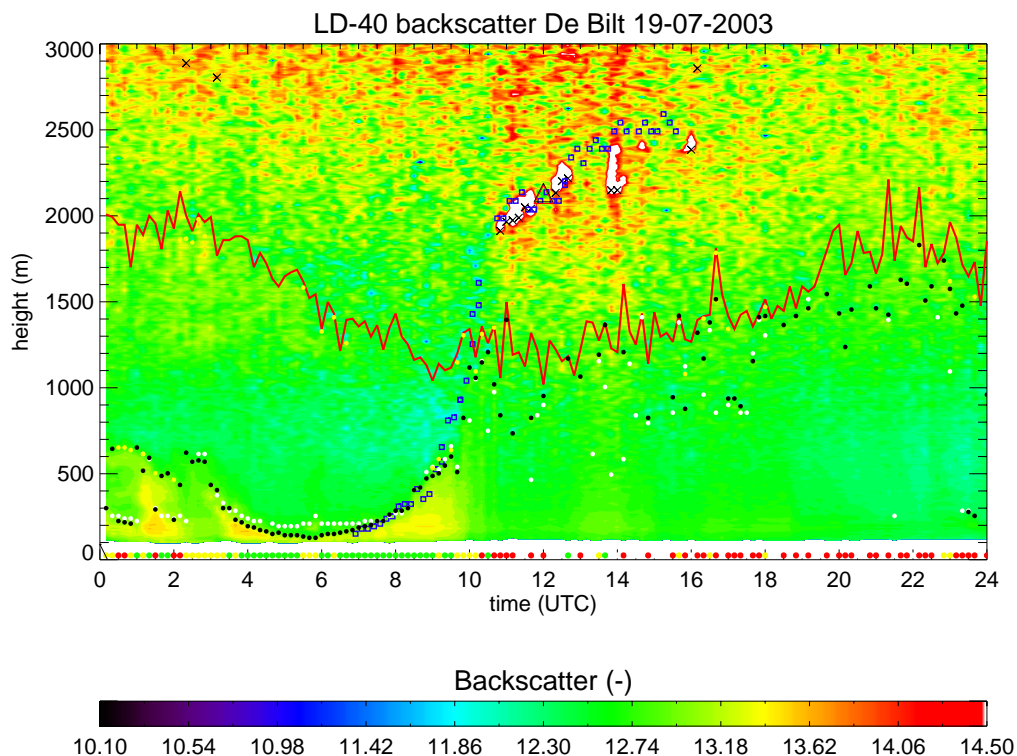
FIGURE 5.5. Same as Figure 5.1, but for De Bilt on July 19, 2003. Note that the wind profiler estimates for this day are presented by blue squares.

The radiosonde profiles of potential temperature and relative humidity for this case are shown in Figure 5.6. Note the obvious characteristics of a developing mixing layer, considering the difference between the 00 and 12 UTC measurements. A stable situation is clearly present in the lowest 100 m of the 00 UTC potential temperature profile, a significant unstable surface layer is observed at 12 UTC. In the 12 UTC profile of potential temperature a capping inversion is shown between approximately 1900 and 2300 m, which explains the radiosonde MLH estimates around 2100 m.

This day demonstrates a case in which the sensitivity of the ceilometer (see section 2.3.1) is clearly too low to obtain a reliable backscatter signal for the whole mixing layer. Detections of Peaks MLH and Wavelet MLH1 are correlated after 10 UTC, although strongly variable. The algorithms are triggered on small and weak structures that strongly vary in height. The largest part of the corresponding detections has a quality index 'Poor'. Hence, this indicates not to rely blindly on the ceilometer MLH determinations. A high power lidar will generally have less trouble detecting aerosol layers in the boundary layer in these conditions, because of the higher sensitivity of the instrument.
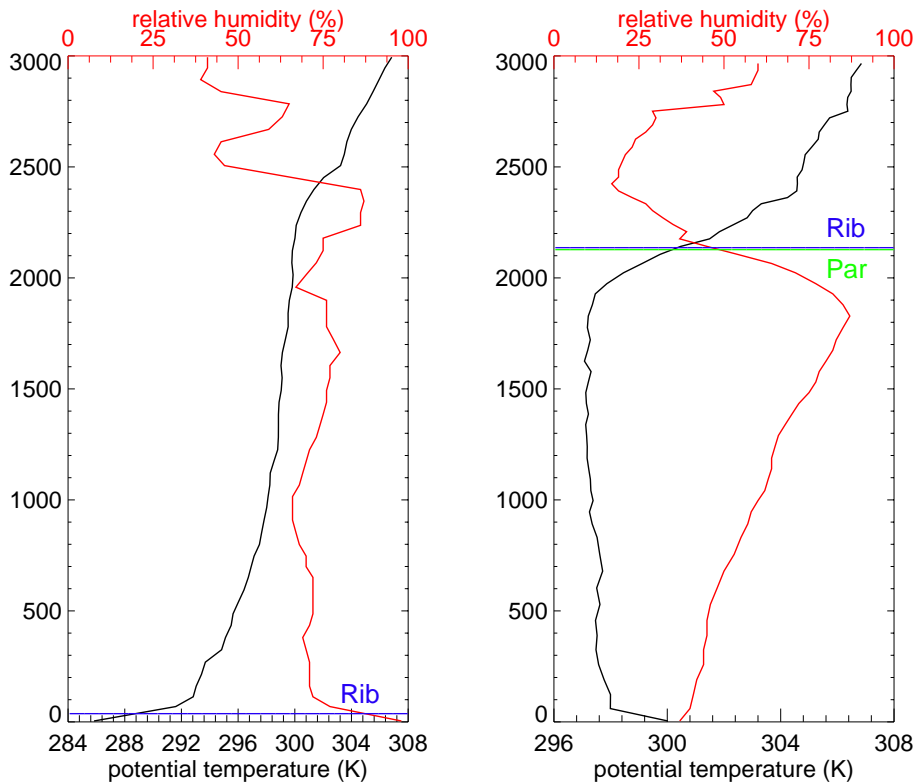
FIGURE 5.6. Radiosonde measurements of potential temperature (black) and relative humidity (red) for July 19, 2003, 00 UTC (left) and 12 UTC (right). The blue and green lines depict MLH estimates carried out with the Richardson bulk method and Parcel method, respectively.

5.2.4 Small diurnal cycle: De Bilt – January 14, 2006

Whereas convective mixing layers are generally characterised by a significant diurnal variation of MLH, days with a more neutral stratification in the surface layer tend to have a less pronounced diurnal variation. This is often the case in wintertime, e.g. for the example shown in Figure 5.7, where aerosol backscatter and estimates of mixing layer height are shown for De Bilt on January 14, 2006.

Peaks and Wavelet estimates are in good agreement for this case, showing a mixing layer that has its top around 300 m at 00 UTC and persists at this height almost continuously. The LD-40 MLH estimates at 00 UTC agree well with the radiosonde MLH estimate as reported by the Richardson bulk method (265 m), whereas the Parcel methods does not give a valid estimate because of the stable situation. Only little development is seen in the LD-40 MLH time series between 09 and 14 UTC, at which the maximum top height of 413 m (Wavelet MLH1) is reached. Above the mixing layer the top of a secondary aerosol layer is observed, which is in some cases detected as MLH2 by the Wavelet algorithm.

The capping inversion that is present in the radiosonde potential temperature profile at 12 UTC (not shown) ranges between 200 and 400 m. The Richardson bulk method reports the MLH at 235 m, against an estimate of only 95 m reported by the Parcel method. The latter is caused by the fact that the Parcel method only gives reliable estimates in marked convective conditions. In more stable conditions the surface

39

buoyancy of a rising parcel is very low, due to the fact that the surface potential temperature is generally closer to the potential temperature in the surface layer.
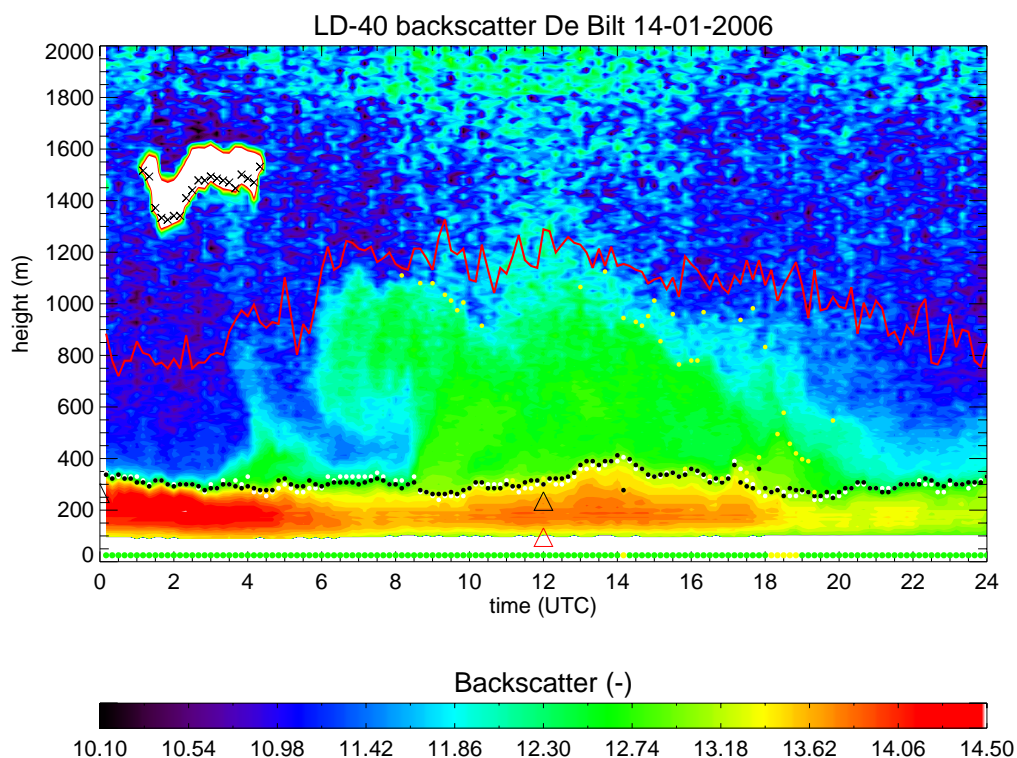

FIGURE 5.7. Same as Figure 5.1, but for De Bilt on January 14, 2006.

It is in general easier to detect the top of a wintertime mixing layer, because a shallow mixing layer implies MLH detections in a region with a more pronounced backscatter signal. This prevents ambiguous conditions, because the interface between the aerosol layer and the free atmosphere is much sharper and contains less small-scale structures. Hence, the algorithms will show more consistent and less variable results. This of course only holds if enough aerosols are available in the mixing layer. For the case considered here, this is expressed in the quality indices that are observed during the day. Good MLH detections are shown almost the whole day, with only a few 'Weak' (=yellow) detections around 14 and 18 UTC.

5.3 Comparison with wind profiler Cabauw

As discussed in chapter 3, wind profilers are also commonly used measurement platforms for determining the (convective) mixing layer height. The LAP-3000 wind profiler in Cabauw is routinely operated by the Atmospheric Research Department (KS/RK) of KNMI. Estimates of MLH from wind profiler radar backscatter profiles were already shown in two of the typical cases in the previous section. It was noted that large differences in the MLH determinations between wind profiler and ceilometer can occur, for example in the case of a deep mixing layer with a lot of noise in the ceilometer backscatter signal, like on July 19, 2003 (section 5.2.3). On the other hand, in case of a well defined mixing layer top, like on July 27, 2002, wind profiler and ceilometer estimates show very good agreement.

Figure 5.8 shows the backscatter contour plot for the LD-40 in Cabauw, on August 29, 2001. After the morning period, that is characterised by fog and clouds around 600 m, the development of the mixing layer starts around 07 UTC. The growth of the mixing layer can clearly be seen in both the ceilometer and the wind profiler estimates. The agreement is good until approximately 13 UTC, at which the LD-40 contour plot shows an area with reduced aerosol backscatter in the upper part of the mixing layer, lowering the upper boundary of high values of aerosol backscatter down to around 700 m. Therefore, the Peaks and Wavelet estimates of MLH do also occur in this height region. The difference between the ceilometer and wind profiler varies between 100 and 200 m for the afternoon until the last available wind profiler estimate at 15:50 UTC. The considerable good agreement of Wavelet MLH2 with the wind profiler estimates proves that a second significant decrease in aerosol backscatter is present above the MLH1 estimates during this period. It appears that for this case the large vertical extent of the inversion layer and the presence of multiple patchy structures in aerosol backscatter around the height of the inversion layer again causes the large temporal variability in mixing layer height reported by the ceilometer algorithms and the difference that is observed compared to the wind profiler estimates. This was noted before in the period around noon for August 30, 2005 (Figure 5.3). These detections have mostly a 'Weak' quality index.
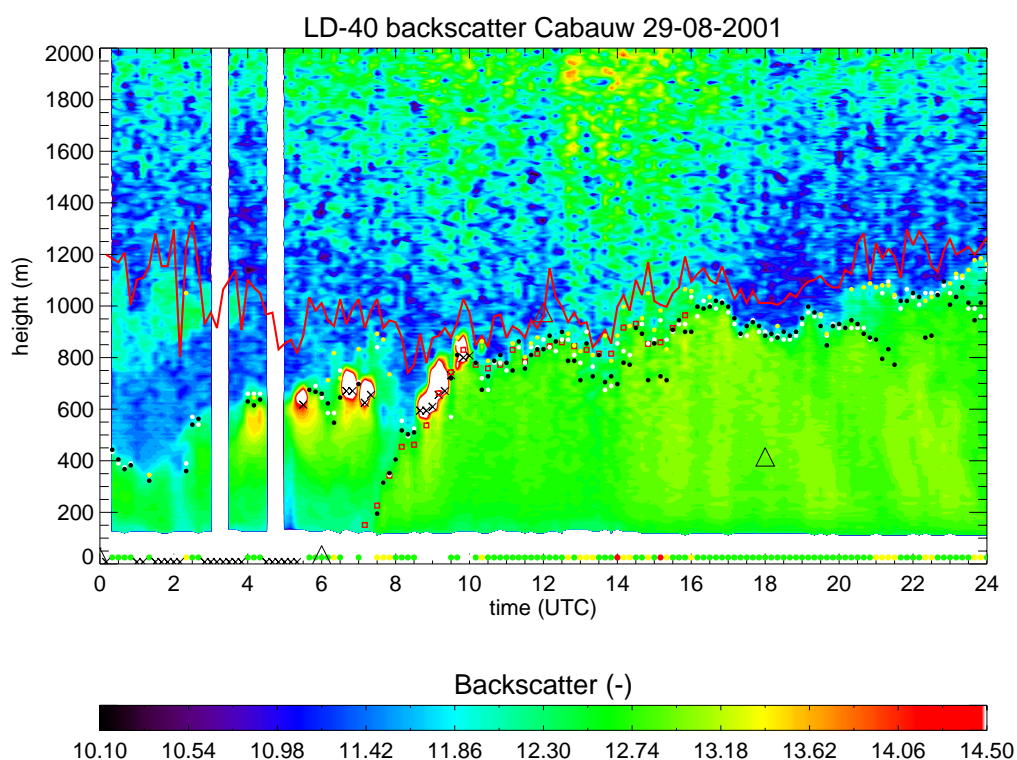
FIGURE 5.8. Same as Figure 5.1, but for Cabauw on August 29, 2001. Note the data gaps in the morning period, indicated by the vertical white bars in the plot.

The ceilometer MLH estimates in the convective mixing layer are generally lower for this afternoon period, with respect to the wind profiler MLH estimates. This difference can be explained to some extent by the characteristics of the LD-40 backscatter signal around the inversion layer. If the backscatter signal is very noisy or shows secondary structures upon

the large scale backscatter structure which is caused by the inversion layer itself, both the Peaks and Wavelet algorithms are triggered too low. On the other hand, in case the mixing layer under consideration is not too deep, and a sufficient amount of aerosol is available at the surface for a reliable backscatter signal throughout the whole layer, the detection of the MLH by the algorithms is in much better agreement with wind profiler observations.

5.4 Comparison with RIVM lidar Bilthoven

The 1064 nm backscatter lidar of the Laboratory for Environmental Monitoring of the National Institute for Public Health and the Environment (RIVM) has operated automatically since the mid-nineteen eighties. Mixing layer heights were determined manually up to 1992, when an automatic algorithm (De Ruiter and Swart, 1991) was installed. The same system was operational in Bilthoven up to 2001, and has been operational at Cabauw since. For this study, overlapping time series of automatic MLH estimates from the RIVM lidar in Bilthoven (January, 1999 – February, 2001) were available.
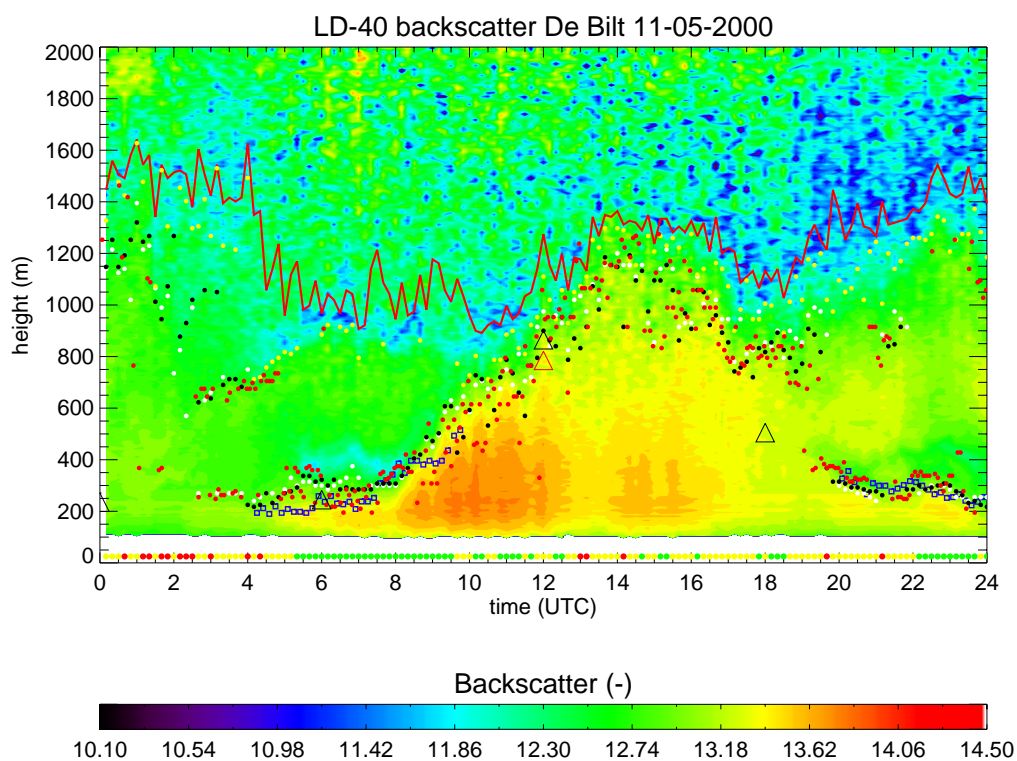
FIGURE 5.9. Same as Figure 5.1, but for De Bilt on May 11, 2000. The lowest of the three MLHs reported by the RIVM lidar MLH algorithm is depicted by the red dots. Note that the wind profiler estimates for this day are presented by blue squares.

Backscatter contours and MLH estimates by the ceilometer algorithms and the lowest MLH estimate by the RIVM lidar are depicted in Figure 5.9 for May 11, 2000. During the first two hours no clearly marked mixing layer is present, which results in elevated detections by both the LD-40 and the RIVM lidar. The 00 UTC radiosonde estimate of MLH is located at 235 m (Richardson bulk), but apparently the jump in aerosol backscatter at the nocturnal ML top is too weak. Between 04 and 08 UTC the temporal

variability of the detections decreases and a mixing layer loaded with a relative high amount of aerosol is observed, with its top between 200 and 400 m. Above this shallow layer MLH2 is estimated at the top of a secondary aerosol layer that is clearly visible in the contours, obtaining a height of between approximately 600 and 900 m. The development of a convective mixing layer without clouds is observed for the daytime period.

The LD-40 and RIVM MLH detections are consistent at a first glance, but during the period of convective development (roughly between 08 and 15 UTC) the variability of the time series derived by both instruments is large. Whereas during the first phase (08 – 12 UTC) the RIVM lidar reports generally a lower mixing layer height than the LD-40, it appears that for the period between 12 UTC and 15 UTC the situation is reversed. The Peaks and Wavelet algorithm estimate MLH considerably lower than the RIVM algorithm in this period, with a difference of about 200 to 300 m at maximum. After 15 UTC, the agreement between the LD-40 and the RIVM lidar estimates increases again. Note the shallow mixing layer during the evening period, topped again by a well developed residual layer. Around 21 UTC, the LD-40 algorithms and the RIVM algorithm report some coinciding elevated estimates between 700 and 1000 m. Note that the 06 UTC and 12 UTC and – to less extent 18 UTC – estimates of MLH from the Richardson bulk method support the MLH as determined by the LD-40 and RIVM lidar algorithms.

The 00, 06, 12 and 18 UTC backscatter profiles for this day are plotted in Figure 5.10, together with the Peaks and Wavelet detections of MLH. Note the high consistency between the Peaks MLH and Wavelet MLH1 detections. For an explanation of the above mentioned difference between the estimates of the LD-40 and the RIVM lidar, the 12 UTC backscatter profile is considered here, because it is the most representative for the afternoon period. A relatively deep inversion layer with large variability in the backscatter signal is observed, ranging from approximately 800 m up to 1150 m.

This could explain to a large extent why the RIVM lidar reports higher values of MLH for the corresponding afternoon period. Whereas the LD-40 algorithms are triggered at the level for which the first steep decrease in backscatter within this inversion layer is seen, the RIVM algorithm may have detected MLH at the same time at another level within this layer. Possible causes for this behavior have to be found within the specifications the algorithms, the quality (SNR) or applied averaging of the backscatter signals, or local meteorological influences on the vertical distribution of aerosol content. Note that the better agreement between the LD-40 and the RIVM lidar for the other conditions that are depicted in Figure 5.10 coincides with the observation of thinner inversion layers in the corresponding backscatter profiles.
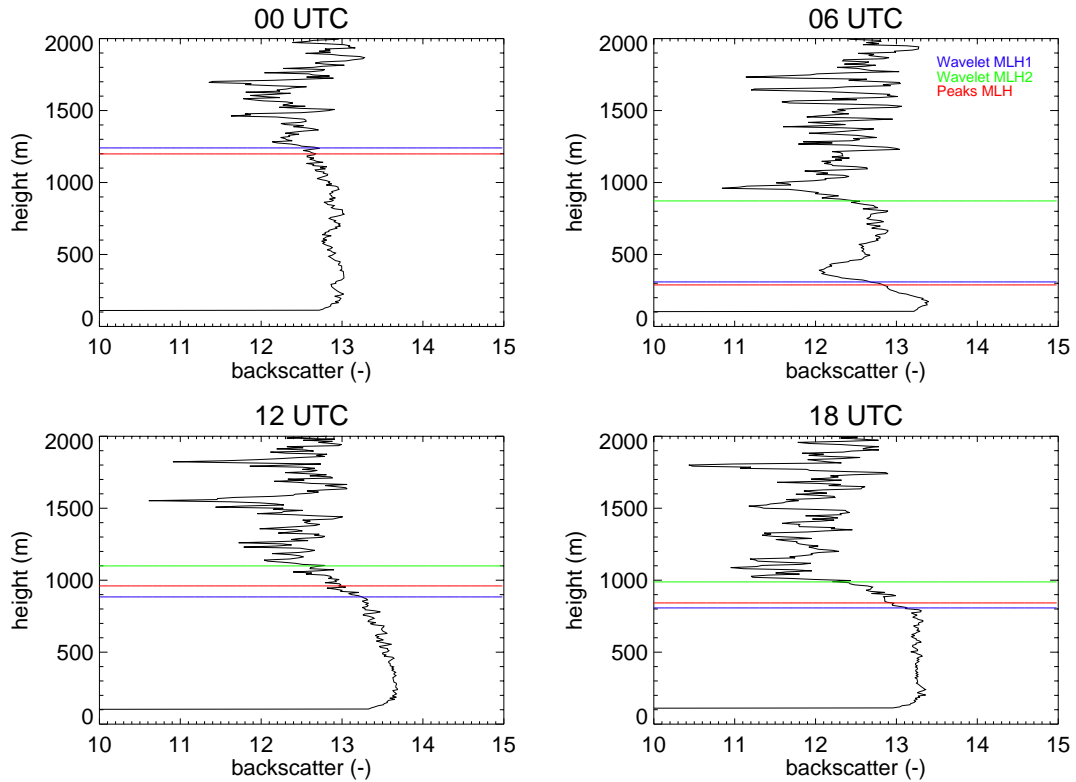
FIGURE 5.10. LD-40 backscatter profiles for De Bilt on May 11, 2000, at 00, 06, 12 and 18 UTC. The height of the Peaks and Wavelet MLH determinations are reported by the horizontal lines.

5.5 Comparison with RACMO

The Atmospheric Research Department (KS/RK) of KNMI uses the Regional Atmospheric Climate Model (RACMO) primarily as a research model for the development of parameterisations for large-scale weather and climate models. Additionally, it is used also as a semi-operational weather forecast model.

Two different versions of RACMO exist. The first one, RACMO1, is operational since 1995, and contains the dynamical core of the HIRLAM weather forecast model version 2.3, together with ECHAM4 physics. Planetary boundary layer height is evaluated following the scheme of Vogelezang and Holtslag (1996), very similar to the method described as the advanced Parcel method in section 2.3. RACMO2, operational since 2002, consists of the dynamical core of the HIRLAM version 5.0.6 and the physics of the ECMWF model cycle CY23R4. For this version, the calculation of planetary boundary layer height is based on the Richardson bulk method described by Troen and Mahrt (1986). It is defined as the height at which the Richardson bulk number, based on the difference between quantities at that level and the lowest model level, reaches the critical value R_{ibc} of 0.25.

Time series of planetary boundary layer height for the 50x50 km grid box Cabauw are available for both versions, for RACMO1 from November 1996 to March 2006, and for RACMO2 from January 2003 to March 2006. The daily RACMO output is a result of a forecast run which starts every day at 12 UTC, in which the temperature, moisture,

pressure and wind fields are initialised with the ECMWF analysis. Prognostic variables, like surface and soil temperatures, snow cover, as well as cloud cover and liquid water content, are imported from the previous day 24 hour forecast. The lateral boundaries are forced with ECMWF forecasts.

As mentioned above, the RACMO1 and RACMO2 calculations of the boundary layer heights are based on the thermodynamic state of the boundary layer and therefore resemble radiosonde determinations to a large extent. The ceilometer algorithms estimate mixing layer height from aerosol backscatter profiles. Complicated deep inversion layers without sufficient aerosol load for reliable detection or mixing layers with a strongly variable backscatter signal are sometimes disturbing the ceilometer MLH algorithms. This should be taken into account in the comparison between model predictions of boundary layer height and the LD-40 mixing layer height.
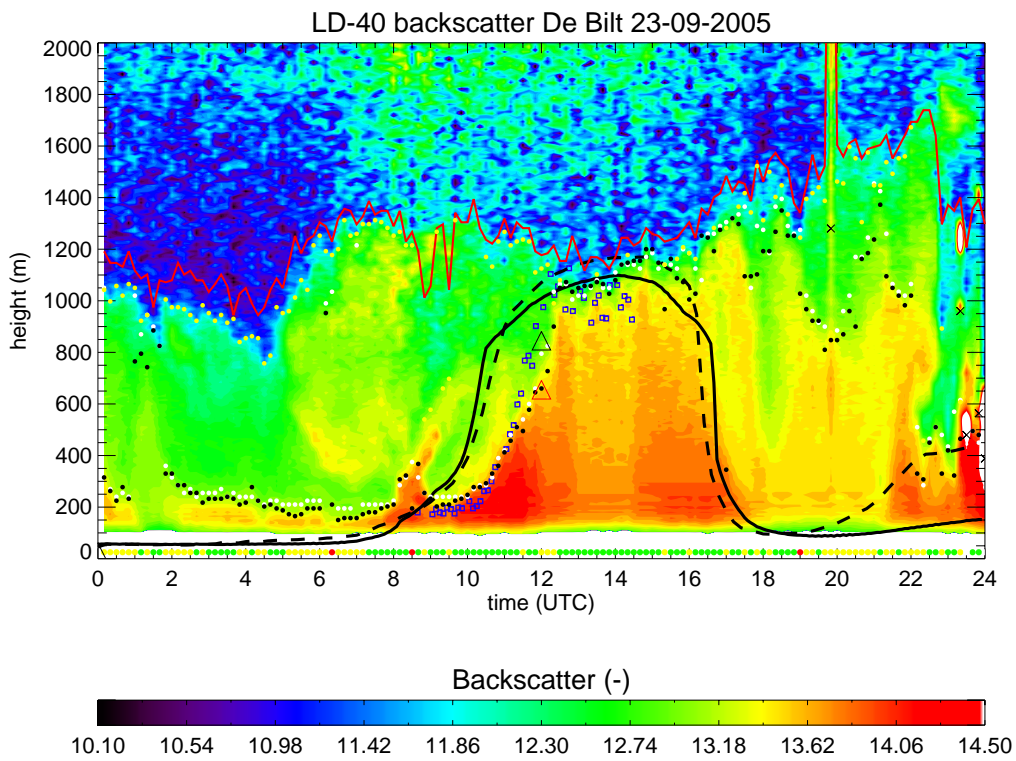
De Bilt – September 23, 2005
The LD-40 backscatter contours and MLH estimates by the Peaks and Wavelet algorithms for De Bilt on September 23, 2005, are plotted in Figure 5.11, together with the planetary boundary layer height that was calculated by RACMO1 and RACMO 2.

A good agreement is observed with respect to the maximum mixing layer height that is reached in the afternoon (1000 – 1200 m), but note that the development of the RACMO boundary layer height seems to set in too early. Whereas the RACMO PBL height knows its maximum growth rate (440 and 510 m/hour for RACMO1 and 2, respectively) between 10 and 11 UTC, the MLH reported by the ceilometer algorithms grows only 180 (Peaks) and 165 m (Wavelet) on the same time interval. The good agreement with the development of MLH from the wind profiler in Cabauw and with the 12 UTC MLH estimate by the radiosonde supports the evolution of MLH as derived from the LD-40 measurements.

When turbulence weakens and the RACMO PBL height shows the characteristic decay after approximately 14 UTC, the LD-40 MLH does not collapse and the large amount of aerosol higher in the mixing layer results in MLH detections by the LD-40 algorithms even above 800 m. Only from 22 UTC onwards, an aerosol layer with its top between 300 and 500 m contrasts enough with the layer above to be detected by the algorithms. This layer roughly coincides with an increase of the RACMO2 PBL height.

De Bilt – July 12, 2005
A completely different case is depicted in Figure 5.12, showing the situation for De Bilt on July 12, 2005. A significant amount of aerosol is again observed in the mixing layer during daytime, and the LD-40 algorithms report an almost constant afternoon mixing layer height of 600 to 700 m. On the other hand, both the RACMO1 and RACMO2 boundary layer heights during the same period show a major diurnal cycle, reaching maximum heights of 1800 to 2100 m around 14 UTC. The large difference between the model and the ceilometer is probably the result of the persisting low cloud deck with a cloud base height around 300 m in the morning.

FIGURE 5.11. Same as Figure 5.1, but for De Bilt on September 23, 2005. PBL heights predicted by the RACMO1 and RACMO2 models for the grid box Cabauw are depicted by the solid and dashed black line, respectively.
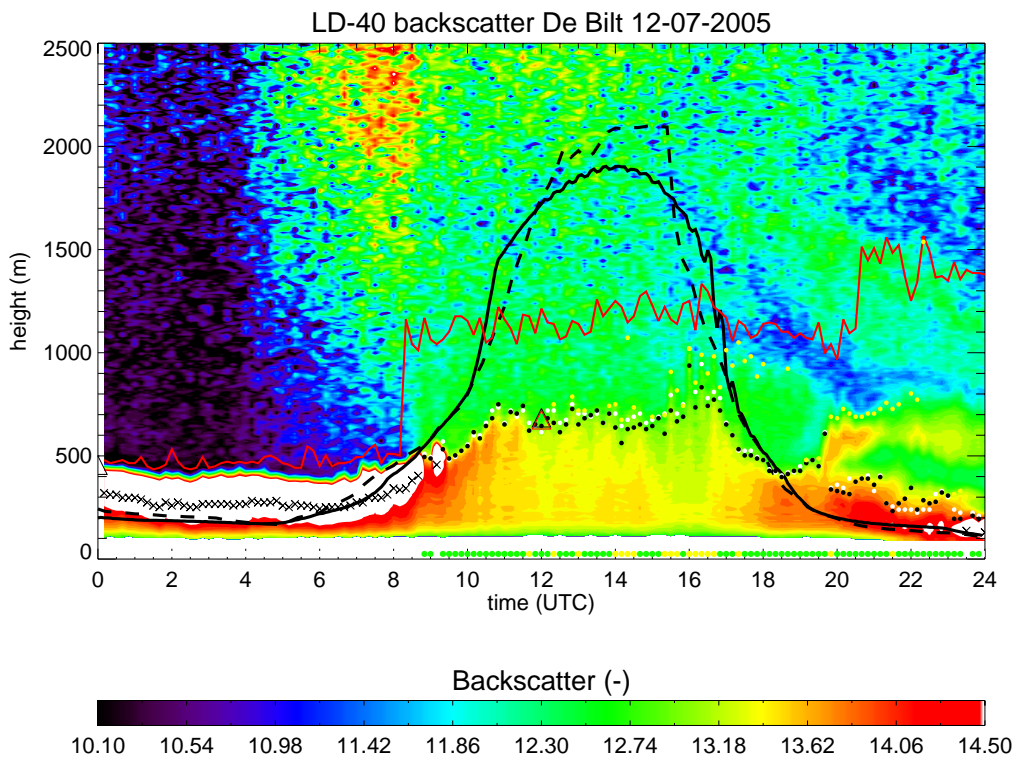
FIGURE 5.12. Same as Figure 5.11, but for De Bilt on July 12, 2005.

This decreases the amount of solar radiation that is available at the surface during the first hours after sunrise. Hence, the growth of the convective mixing layer is tempered for this case. RACMO however did not predict this persisting cloud deck, which resulted in an overestimation of the height of the boundary layer during daytime. The Wavelet MLH1 quality indices derived for this day are mostly 'Good' (=green) with some periods of 'Weak' (=yellow) detections. This implies reliable LD-40 MLH1 estimates. This is supported by both the Richardson bulk method and the Parcel method applied to the radiosonde measurements at 12 UTC, which report a mixing layer height in very good agreement with the LD-40.

5.6 Summary of the case studies

The cases discussed in this chapter provide insight in the capabilities of MLH estimation from LD-40 backscatter data under various atmospheric conditions. Furthermore, the comparison with MLH derived from other measurement platforms indicates the advantages and disadvantages of using the LD-40 ceilometer for MLH estimation. The RIVM research lidar has a special position within this comparison because MLH estimation from this instrument uses the same atmospheric variable, i.e. aerosol backscatter, for detection.

5.6.1 Case studies

Most important feature observed in the case studies is the strong dependence of the quality of the detection (of Wavelet MLH1, but also in general) on the variability of the signal in the mixing layer. For pronounced backscatter profiles, time series variability of MLH is often very small and detections obtain a 'Weak' or 'Good' quality index in most cases. On the other hand, strongly varying time series of MLH indexed with a 'Poor' (=red) quality index are often the result of a variable backscatter signal with height, containing a lot of small-scale structures. This problem occurs in particular for deeper mixing layers, and is e.g. observed for July 19, 2003. In these cases the sensitivity of the ceilometer is too low to obtain a reliable backscatter signal throughout the whole mixing layer, given the total aerosol load present in the layer. For July 19, 2003, the SNR<1 height was found about 1000 m lower than the radiosonde estimate of MLH at 12 UTC.

The lower boundary of the MLH estimation in both ceilometer algorithms is 90 m. This is a result of the lowest range gate of the LD-40, combined with the applied overlap correction (section 3.2.1). In a number of cases (e.g. August 30, 2005 and July 19, 2003) a poor agreement was observed between the thermodynamically derived 00 UTC radiosonde MLHs and the LD-40 estimates of MLH. Apparently, the LD-40 is not able to detect very shallow MLHs. This shortcoming is especially observed for nocturnal (stable) mixing layers.

Both algorithms also have problems during the afternoon decay phase of the (convective) mixing layer. Whereas a well-developed convectively driven mixing layer usually decays in height during the afternoon, a persisting deep mixing layer is observed for some cases, e.g. for August 30, 2005 and August 29, 2001. This is mainly caused by the large aerosol content that resides in the residual layer which results in suppressed contrast with aerosol structures underneath.

On the other hand, the Peaks and Wavelet algorithms have performed well in the other cases and provided reliable estimates of the MLH, based on the visual inspection of aerosol contours, and compared to radiosonde, wind profiler, RIVM lidar and RACMO estimates. It was shown that the ceilometer MLH algorithms generate very similar results, in particular for well-defined mixing layers which grow not too deep and which are characterised by a homogeneous vertical profile with a high value of aerosol backscatter. These conditions provide the opportunity to make a reliable estimate of MLH, in spite of the low sensitivity of the ceilometer system. The considered winter case (i.e. January 14, 2006) is a nice example of such an 'easier' case, demonstrating an almost constant MLH time series with hardly any diurnal variation.

The estimates of MLH2 by the Wavelet algorithm are a good indicator of a residual layer (e.g. July 27, 2002 and May 11, 2000) but sometimes the MLH2 estimate is located only some tens of metres higher than MLH1. Apparently, in these cases the MLH1 is sometimes estimated too low or the inversion layer in which it is embedded is deep and contains more than one significantly decreasing backscatter levels. The corresponding quality index of MLH2 should be considered to assess the reliability of the detection.

5.6.2 Other measurement platforms

In general, a good resemblance was observed for the LD-40 MLH and the MLH derived from radiosonde profiles at 12 UTC. The Parcel method generally gives a lower estimate of MLH than the Richardson bulk number method when applied to the same radiosonde observations. It was shown that in particular for estimates with a 'Good' quality index, the LD-40 and radiosonde estimates of the MLH show good agreement. The latter is for example seen on August 30 and July 12, 2005. Nevertheless, for the case with the shallow mixing layer and a small diurnal cycle on January 14, 2006, the agreement between LD-40 and radiosonde is less good. Section 6.3.1 describes a statistical comparison of LD-40 and radiosonde estimates of mixing layer height.

The LD-40 estimates were also compared with MLH estimates from the wind profiler in Cabauw. For the five cases for which the profiler estimates were analysed, the agreement seems good if the quality index of the ceilometer MLH estimate is 'Weak' or 'Good'. An example for which the agreement is poor is the case of July 19, 2003. The wind profiler follows the radiosonde MLH and reports the complete development of the MLH up to around 2500 m, whereas the LD-40 results consist of an extremely variable MLH time series with mainly 'Weak' and 'Poor' quality indices, approximately 1500 m lower than the wind profiler estimates. For the other cases described in this chapter, the agreement is good, and as well the morning development as the afternoon values of the MLH for both instruments follow each other closely. Even if the instruments are not closely collocated, as in the case of the comparison of the LD-40 in De Bilt with the wind profiler in Cabauw (approximately 30 km southwest of De Bilt), the results are satisfactory. A further comparison with wind profiler estimates is discussed in section 6.3.2.

One case was discussed concerning the comparison with RIVM lidar MLH estimates for Bilthoven (May 11, 2000). LD-40 estimates in De Bilt show roughly the same evolution of MLH, but the variability in the afternoon is large for both instruments and hence the

agreement is expected to change from case to case. The large variability in the time series was caused here by a deep inversion which enhances the ambiguity in MLH detection for all measurement platforms. The frequency of occurrence of RIVM MLHs is presented in section 6.3.3.

Finally, time series of planetary boundary layer height predicted with two versions of the regional climate model RACMO were considered for two summer cases with well-pronounced mixing layers. It was shown that the morning development of the boundary layer height predicted by the model sets in too early compared to the MLH estimated by the LD-40 and the wind profiler, as particularly observed on September 23, 2005. The maximum height reached in the afternoon however agrees very well. At the end of the afternoon, RACMO predicts a strong decay of the convective mixing layer, but the LD-40 still reports a high value for MLH because of the large amount of aerosol which resides in the residual layer. This is a known problem in the detection of mixing layer height from lidar systems. For the second case, on July 12, 2005, the LD-40 and radiosonde match perfectly at 12 UTC, while both versions of RACMO overestimate the development and the maximum height of the mixing layer significantly. The latter is probably caused by a persistent cloud deck in the early morning, which reduces the shortwave heating at the surface.

6 Results

6.1 Introduction

In chapter 5 a number of cases was discussed to illustrate the capabilities of the ceilometer MLH algorithms in some typical atmospheric conditions. A statistical analysis of the results of the MLH detection by both algorithms for a six year period is presented in this chapter. This analysis is also extended to the intercomparison of the MLH detection by three other measurement platforms, i.e. radiosonde, wind profiler and RIVM lidar.

6.2 Ceilometer MLH algorithm intercomparison

The Peaks and Wavelet MLH algorithms did not differ very much for the case studies discussed in the previous chapter. In this chapter some statistical aspects of the MLH estimation by both algorithms will be considered for a longer period, in order to assess the advantages and disadvantages of both algorithms and to decide which MLH algorithm will be used in the further stages of this project. To this end the data set of the LD-40 at the KNMI test field in De Bilt is used as LD-40 backscatter profiles were continuously stored in the period 2000 – 2005.

6.2.1 Monthly mean diurnal cycle of the MLH

The monthly mean diurnal cycle of the Peaks and Wavelet mixing layer heights and the SNR stop level for the six year period are shown in Figure 6.1. Note the strong agreement between Peaks MLH and Wavelet MLH1 for most of the months. The largest differences are observed for the mean diurnal cycles in April.

Furthermore, an annual cycle of the amplitude of the diurnal variation is observed, with the smallest amplitude for both methods found in December (140 and 136 m for Wavelet MLH1 and Peaks MLH, respectively) and the largest ones observed in May (669 and 606 m for Wavelet MLH1 and Peaks MLH, respectively), as seen in Figure 6.2. The larger diurnal variations which are observed for the spring and summer months are not only visible in the evolution of Peaks MLH and Wavelet MLH1, but also in Wavelet MLH2 and the SNR stop level. The latter shows an inverse-like shape with respect to MLH1, probably caused by the larger amount of background noise in the backscatter signal during the day. Furthermore, the (frequent) appearance of convective clouds during daytime and the coinciding SNR decrease because of extinction of the backscatter signal could contribute to this specific shape.

The monthly mean MLH during daytime for spring and summer months is lower than expected. This is related to the inability of the algorithm to detect most of the deep mixing layers heights (section 5.2.3). The intercomparison with the noon radiosonde MLH estimates quantifies the effect to some extent (section 6.3.1, Figure 6.10). The SNR stop level is characterised by large day to day variability with respect to its mean value, with a standard deviation between 30 and 60 % of the mean value, resulting in typical values of 450 to 650 m (not shown).
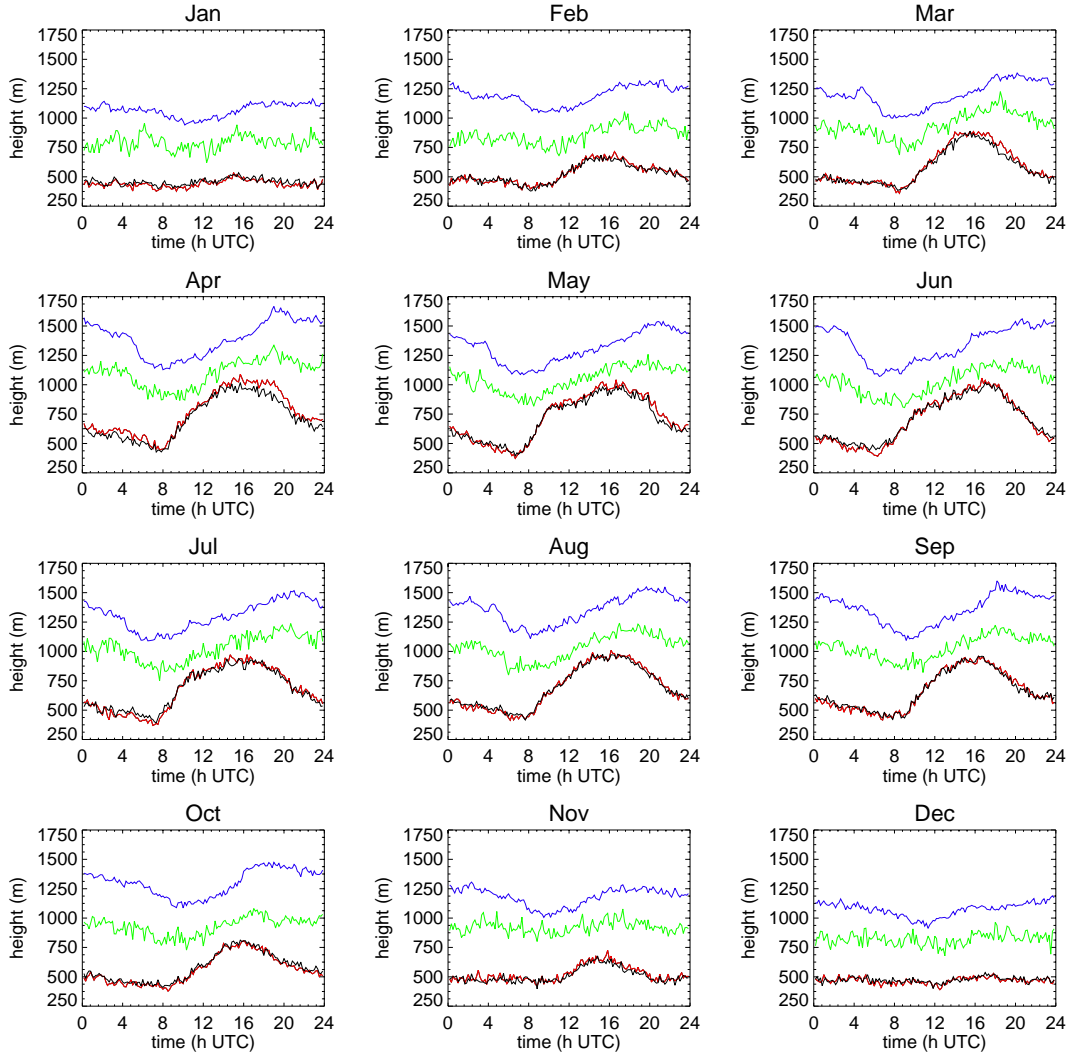
FIGURE 6.1. Monthly mean diurnal cycle for De Bilt, of Peaks MLH (black), Wavelet MLH1 (red), Wavelet MLH2 (green) and SNR stop level (blue) applied to 10 minute averaged LD-40 backscatter profiles. The considered period is 2000 – 2005.

The monthly mean MLH amplitude is calculated as the difference between afternoon maximum MLH and morning minimum MLH and is shown in Figure 6.2 for both methods. Particularly during the autumn and winter months, the mean diurnal amplitude of Peaks MLH and Wavelet MLH1 show good agreement. For the other months, the largest difference is observed in June (88 m). The monthly mean MLH growth time is determined as the duration (in hours) between the time of the morning minimum MLH and afternoon maximum MLH. The value of this growth time ranges between 5.2 h (Dec) and 11.5 h (Jun) for Peaks MLH, and between 5.3 h (Dec) and 10.3 h (Jun) for Wavelet MLH1. The monthly mean growth time is strongly connected to the average length of day in the respective month and hence to the start and decay of convective activity at the surface. The estimated MLH growth times for the winter months are however doubtful, since the diurnal cycle is not clearly visible for these months. Note furthermore that the calculated growth times for May and June are likely overestimated, because the location of the maximum mixing layer height within the diurnal cycle seems to be shifted as a result of the inability to detect high MLHs in these months.
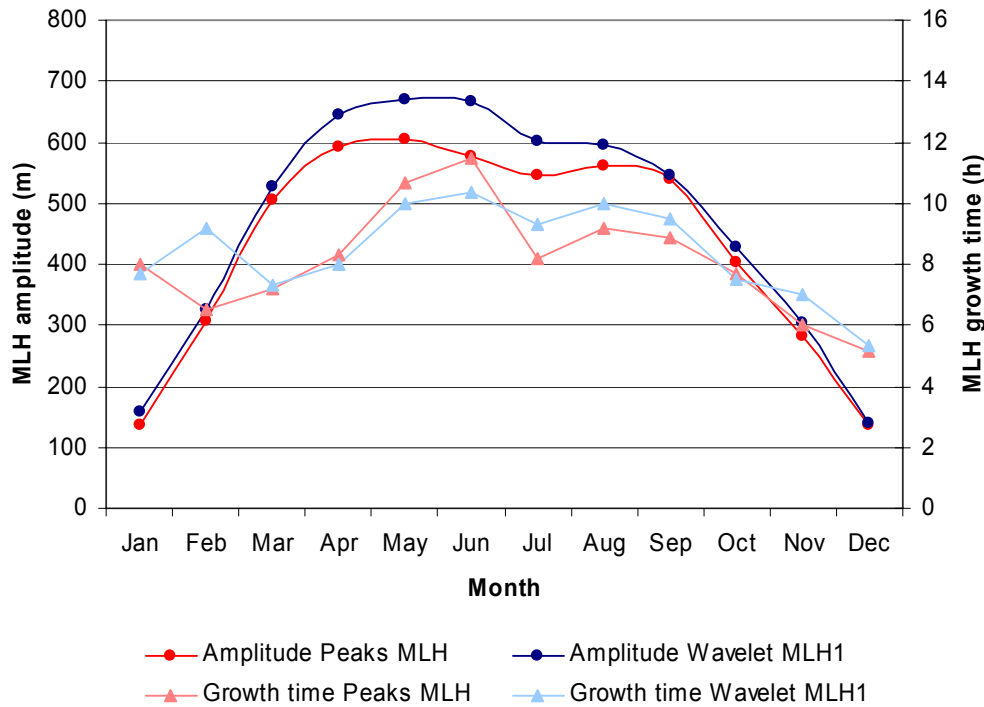
FIGURE 6.2. Monthly mean diurnal amplitude and growth time for Peaks MLH and Wavelet MLH1.

6.2.2   Monthly mean detection rates

An overview of the performance of the Wavelet MLH1 algorithms in the period 2000 – 2005 is listed in Table 6.1. The results in this table are based on the total number of available backscatter profiles for each month; periods with no data are not included in the analysis. The overall detection rate for MLH1 is between 42.0 % (Dec) and 60.8 % (Aug), but note that the contribution of 'Poor' (=red) detections also increases with increasing detection rate. The most important reason for the lower detection rates during the winter months is the larger amount of weather conditions like fog, rain and clouds, which inhibit a successful MLH detection. Whereas in January fog, precipitation (PI) and clouds (C1) terminate the algorithm in 3.9 %, 8.5 % and 45.0 % of the total number of cases respectively, in June these percentages are only 0.6 %, 5.0 % and 30.4 %.

The same statistical results for all MLH detections by the Peaks algorithm are listed in Table 6.2. The most important difference is the contribution of the algorithm termination by a too weak mean backscatter gradient (column 'Grad'), as described in the algorithm description in section 4.2. Apparently, this situation often coincides with cases in which the detection of Wavelet MLH1 is not possible due to the presence of a cloud, because its contribution compensates for the lower termination due to the presence of a cloud base (column 'C1'). Note that the overall detection rate is lower than the detection rate of Wavelet MLH1, with an average difference between the two methods of 3.2 %. The Peaks MLH shows slightly more 'Good' and 'Poor' detections. On the other hand, the contribution of the 'Weak' quality index is significantly higher for the Wavelet MLH1 estimates. Note that generally, the nighttime detection rate is higher than the daytime detection rate for both methods (not shown here).

TABLE 6.1. Monthly mean detection rates for Wavelet MLH1 determinations in De Bilt, period 2000 – 2005. Percentages are based on the total number of available cases for each month.

	cases	MLH1 (%)	Good (%)	Weak (%)	Poor (%)	None (%)	Fog (%)	PI (%)	VV (%)	C1 (%)	SNR (%)
Jan	25917	**42.3**	27.6	12.6	2.0	**57.7**	3.9	8.5	0.0	45.0	0.2
Feb	24180	**46.1**	26.7	16.4	3.1	**53.9**	2.9	8.4	0.0	41.8	0.7
Mar	24573	**49.5**	24.5	20.6	4.4	**50.5**	2.2	4.7	0.0	42.9	0.5
Apr	25579	**57.6**	17.7	26.7	13.2	**42.4**	0.7	6.0	0.0	31.8	3.9
May	25015	**56.5**	19.5	23.6	13.3	**43.5**	0.8	5.4	0.1	32.7	4.6
Jun	23354	**59.7**	23.8	24.0	11.9	**40.3**	0.6	5.0	0.1	30.4	4.3
Jul	25016	**49.4**	19.9	20.1	9.4	**50.6**	1.6	7.1	0.1	38.1	3.6
Aug	25710	**60.8**	24.7	25.7	10.3	**39.2**	1.8	4.8	0.1	29.8	2.8
Sep	24420	**58.4**	23.0	27.7	7.8	**41.6**	2.1	6.6	0.2	30.4	2.3
Oct	24709	**60.2**	29.5	25.9	4.8	**39.8**	1.9	6.5	0.1	30.7	0.6
Nov	25086	**46.3**	23.6	18.6	4.1	**53.7**	4.8	9.3	0.0	39.0	0.6
Dec	26199	**42.0**	24.1	14.8	3.0	**58.0**	4.6	8.3	0.0	44.5	0.6
Total	299758										
Average		**52.3**	23.7	21.3	7.3	**47.7**	2.3	6.7	0.1	36.5	2.0

TABLE 6.2. Monthly mean detection rates for Peaks MLH determinations in De Bilt, period 2000 – 2005. Percentages are based on the total number of available cases for each month.

|	cases	MLH (%)	Good (%)	Weak (%)	Poor (%)	None (%)	Fog (%)	PI (%)	Grad (%)	C1 (%)	SNR (%)
Jan	25917	**41.5**	27.5	9.8	4.2	**58.5**	3.9	8.5	10.3	35.5	0.1
Feb	24180	**44.2**	26.8	12.4	5.0	**55.8**	2.9	8.4	14.0	30.3	0.2
Mar	24573	**47.5**	24.1	15.6	7.8	**52.5**	2.2	4.7	14.4	31.0	0.1
Apr	25579	**50.1**	17.4	18.1	14.6	**49.9**	0.7	6.0	23.8	18.0	1.4
May	25015	**50.9**	19.4	17.1	14.3	**49.1**	0.8	5.4	21.5	19.4	1.9
Jun	23354	**55.2**	24.5	17.8	13.0	**44.8**	0.6	5.0	21.2	16.1	1.9
Jul	25016	**46.5**	20.0	15.0	11.5	**53.5**	1.6	7.1	20.2	22.9	1.6
Aug	25710	**57.3**	25.1	19.8	12.4	**42.7**	1.8	4.8	18.8	15.9	1.3
Sep	24420	**54.5**	24.0	20.2	10.3	**45.5**	2.1	6.6	18.7	17.4	0.7
Oct	24709	**57.7**	30.1	20.5	7.2	**42.3**	1.9	6.5	14.8	18.7	0.3
Nov	25086	**43.8**	23.3	14.2	6.3	**56.2**	4.8	9.3	13.0	28.9	0.1
Dec	26199	**40.7**	24.6	11.1	5.0	**59.3**	4.6	8.3	10.8	35.5	0.1
Total	299758										
Average		**49.1**	23.9	15.9	9.3	**50.9**	2.3	6.7	16.8	24.2	0.8

Both tables are summarised in Figure 6.3. Here it can again clearly be seen that the contribution of the 'Weak' and 'Poor' quality indices in the total number of MLH detections increases rapidly in April and remains high until the autumn sets in. Note the large contribution of C1 in the number of algorithm terminations for July, with respect to the surrounding months. This is most likely caused by the very cloudy and precipitative July months in the period 2000 – 2005. Except for the year 2003, all July months in De Bilt had a precipitation amount and cloud cover above normal conditions.

The higher daytime values of mixing layer height observed for the spring and summer months generally coincide with lower quality indices. This is related to the enhanced vertical variability in the backscatter signal and hence the increased chance on a MLH detection on a less pronounced jump in the aerosol backscatter.
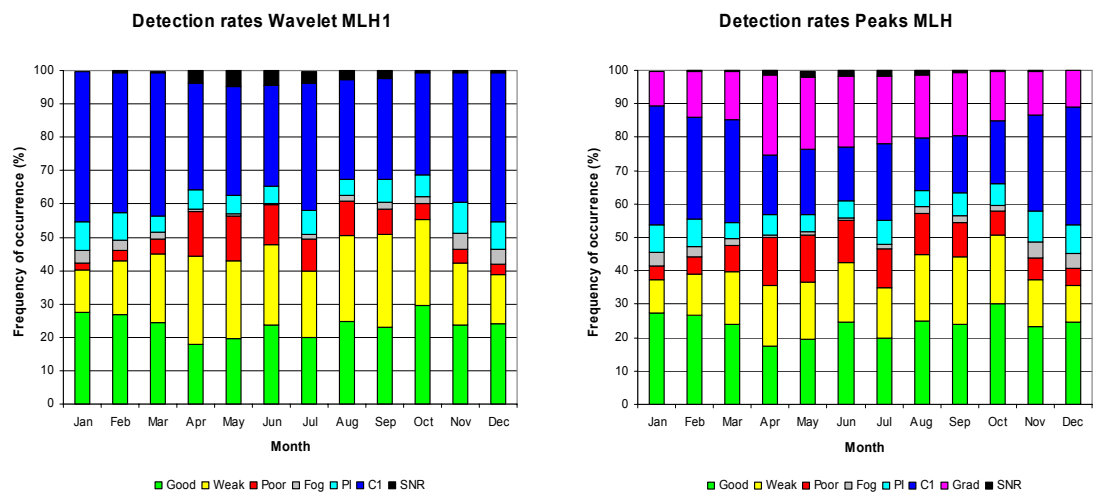
FIGURE 6.3. Monthly mean detection rates for Wavelet MLH1 (left) and Peaks MLH (right), in De Bilt (2000 – 2005). Successful MLH detections are subdivided in the three quality classes ('Good', 'Weak' and 'Poor'); terminations of the MLH algorithm are ascribed to the cause: 'Fog', 'PI' (precipitation), 'C1' (cloud base), 'Grad' (too weak mean backscatter gradient), 'SNR' (SNR stop level). The small number of terminations caused by 'VV' and 'CX' are not incorporated in the plots.

### 6.2.3 Noon intercomparison: quality assessment

The comparison of all simultaneous Peaks MLH and Wavelet MLH1 detections at 12 UTC is presented in Figure 6.4. Actually, this figure contains all detections at 11:40 UTC, because this data will later be used for a comparison with estimates of MLH from radiosonde profiles. All detections, irrespective of quality index, are plotted in the left panel. The l.s.q. linear fit $y = ax + b$ has coefficients $a = 0.90$ and $b = 48$ m, with a value for R^2 of 0.82. Both the methods reported mixing layer height in 683 (34.9 %) of the 1958 possible MLH detections at 12 UTC. In the right panel, only simultaneous detections with the highest quality index are compared. Only 271 (13.8 %) of the total number of points remain for this selection. The linear fit now has coefficients a = 0.98 and b = 2, with a value for R^2 of 0.99. Peaks MLH is generally higher at 12 UTC than the Wavelet MLH1 estimate for both selections, as observed from the coefficient a, which is lower than 1.
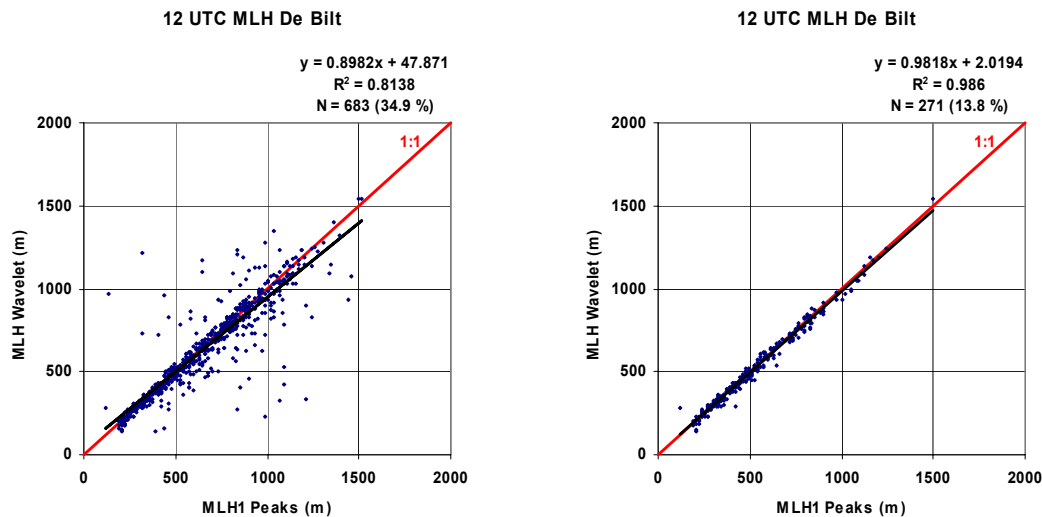
FIGURE 6.4. Scatter plots of Peaks MLH vs. Wavelet MLH1 for simultaneous detections at 12 UTC in De Bilt for 2000 – 2005: all detections (left) and detections with a 'Good' (=green) quality index (right).

Note that the agreement increases if only detections of the highest quality index are taken into account. This is also shown in the four scatter plots in Figure 6.5. For all detections in April in the period 2000 – 2005, a rough distinction is made between nighttime (18 – 06 UTC) and daytime (06 – 18 UTC) detections for both methods. April is considered here because the agreement of the mean diurnal cycles for the two methods is the lowest in this month, as observed in Figure 6.1. The figures in the left panels of Figure 6.5 contain all detections. Generally, a lot of scatter is observed for these figures. The abundance of points within 100 m of the $y = x$ line is 79.3 % and 80.7 % for the nighttime and daytime periods, respectively. A band without any coinciding MLH detections is present, about 100 to 150 m higher than the $y = x$ line. The reason for this artifact is unknown. Furthermore, note a band of increased density around the line Peaks MLH = 250 to 300 m, especially during nighttime. These estimates mostly coincide with low (nighttime) ML tops with a 'Poor' quality, for cases in which Wavelet MLH1 is triggered at the top of a secondary aerosol layer aloft. For the simultaneous 'Good' detections (right panels), it disappears almost completely for both nighttime and daytime. The regression coefficients tend more towards the $y = x$ line for this selection, but the amount of points in the scatter plot reduces significantly. The number of simultaneous detections decreases from 7198 (56.2 % of total) to 2268 (17.7 %) for the nighttime period and from 5179 (40.4 %) to 1271 (9.9 %) for the daytime period.

Linear regression coefficients and resulting values for R^2 for the months January, April, July and October (2000 – 2005) are listed in Table 6.3. The results are based on all cases that occurred in this period for the quality index indicated in the column header and detections with higher quality indices. Thus for the 'Poor' results, all detections are taken into account, whereas for the 'Weak' results both 'Weak' and 'Good' detections are taken into account.
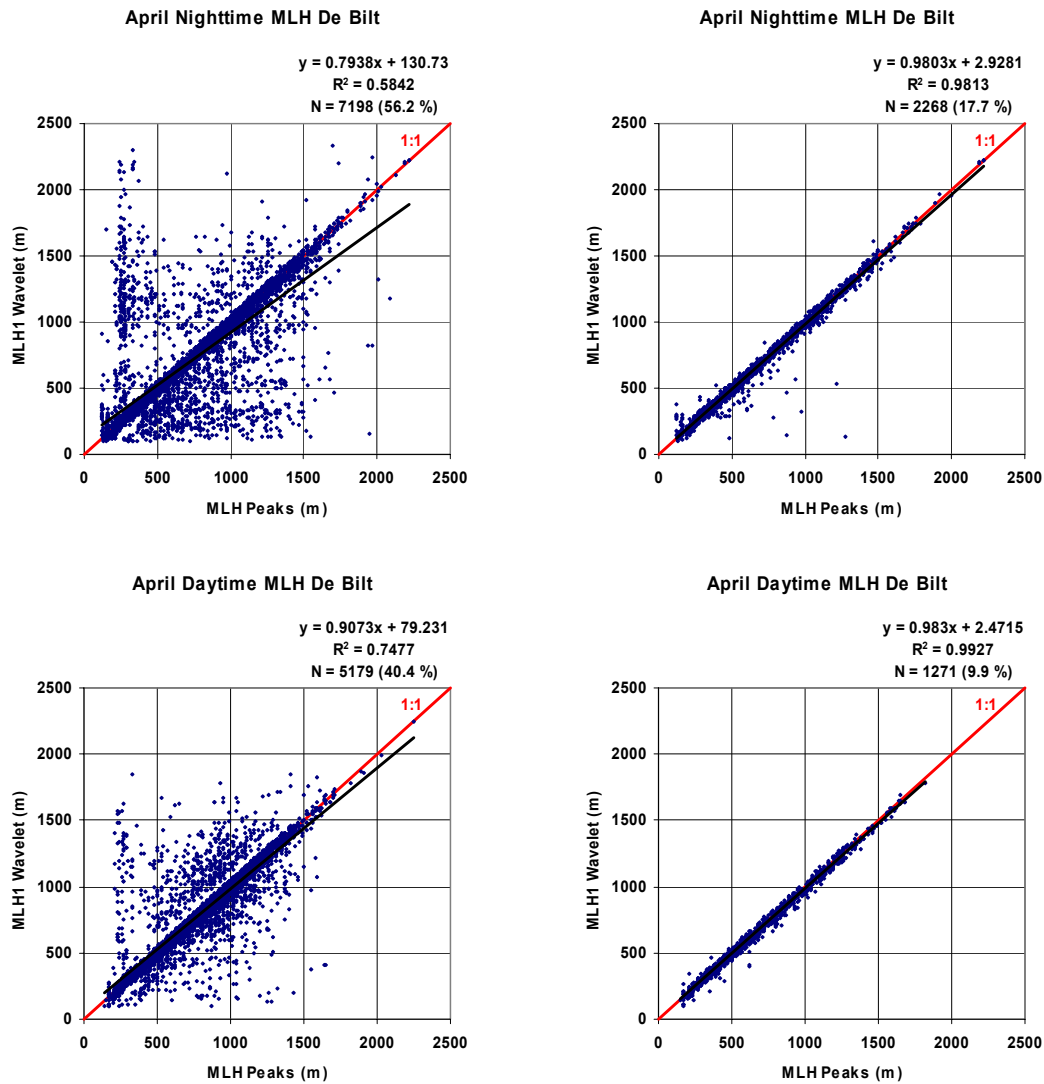
FIGURE 6.5. Scatter plots of Peaks MLH vs. Wavelet MLH1 for simultaneous detections in April in De Bilt for 2000 – 2005, for the period 18 – 06 UTC (upper panels) and 06 – 18 UTC (lower panels). Left panels show all detections, right panels only show detections with a 'Good' quality index.

The agreement between the algorithms based on all coinciding detections (see column 'Poor'), is generally better during daytime, according to the better agreement of regression coefficients to the line $y = x$ and higher correlation. This is possibly caused by the frequent problematic detection of low nighttime MLHs and the presence of multiple (e.g. residual) layers during nighttime. Note again the strongly increasing agreement for increasing quality index. Correlation coefficients in the last column ('Good') range between 0.94 and 0.99, while at the same time regression coefficient a is between 0.95 and 0.98 and b is ranging between 2 and 12 m. Note that the l.s.q. linear fit assumes that the x-ordinate is the independent variable without error. In this case this assumption is not valid and an underestimation of the slope a may be the result.

TABLE 6.3 Results of the regression analysis for Peaks MLH vs. Wavelet MLH1 for the months January, April, July and October in the period 2000 – 2005. Results for each quality index are calculated by using the detections of the respective quality index and higher quality indices.

	Nighttime					
	Poor		**Weak**		**Good**	
	a, b, R^2	# cases	a, b, R^2	# cases	a, b, R^2	# cases
Jan	0.82, 54, **0.70**	5368 (41.2 %)	0.83, 45, **0.79**	4794 (36.8 %)	0.95, 12, **0.94**	3017 (23.2 %)
Apr	0.79, 130, **0.58**	7198 (56.2 %)	0.89, 32, **0.85**	5381 (42.0 %)	0.98, 3, **0.98**	2268 (17.7 %)
Jul	0.81, 88, **0.67**	6886 (54.7 %)	0.85, 48, **0.83**	5441 (43.2 %)	0.97, 9, **0.97**	2740 (21.7 %)
Oct	0.73, 114, **0.58**	7821 (62.8 %)	0.79, 66, **0.74**	6588 (52.9 %)	0.97, 7, **0.97**	3105 (24.9 %)
	Daytime					
	Poor		**Weak**		**Good**	
	a, b, R^2	# cases	a, b, R^2	# cases	a, b, R^2	# cases
Jan	0.82, 55, **0.74**	5103 (39.2 %)	0.83, 47, **0.80**	4702 (36.1 %)	0.96, 11, **0.94**	3262 (25.0 %)
Apr	0.91, 79, **0.75**	5179 (40.4 %)	0.94, 11, **0.93**	3197 (24.9 %)	0.98, 2, **0.99**	1271 (9.9 %)
Jul	0.88, 76, **0.77**	4269 (33.9 %)	0.90, 35, **0.88**	2866 (22.7 %)	0.97, 5, **0.98**	1366 (10.8 %)
Oct	0.87, 53, **0.79**	6245 (50.1 %)	0.89, 31, **0.87**	5509 (44.2 %)	0.97, 8, **0.98**	2955 (23.7 %)

The detection rate for the simultaneous 'Good' detections is between 10 and 25 %, with the smallest rates observed during daytime in April and July. Apparently, this results from the enhanced presence of daytime boundary layer convective clouds in the spring and summer months and the occurrence of deep convective layers with a too small aerosol load to cause a reliable backscatter signal.

6.2.4 MLH frequency distributions

Mixing layer height distributions for the two ceilometer MLH algorithms during daytime (06 – 18 UTC) and nighttime (18 – 06 UTC) in January and July are shown in Figure 6.6. A bin size of 60 m is used to avoid irregularities in the results caused by an unequal number of gates in each height bin. The similar shape for the daytime and nighttime histograms in January is evident, showing maxima for both algorithms around 300 m. Significantly more lower MLH detections are observed during nighttime than during daytime. A clear difference in histogram shape is observed for daytime and nighttime in July. The daytime histograms for the two MLH algorithms show a higher frequency of occurrence for higher MLHs. The maximum can however not be unambiguously determined, since the frequency of occurrence has a broad maximum and is very variable between 240 and 960 m.

Although the enhanced convective development in summer is obviously observed in the nighttime/daytime differences in July, the number of daytime detections above 1250 m is very low. This is remarkable, as one would expect a larger contribution of deep MLHs for this period. As already noted in some of the cases in chapter 5, the detection of MLH at higher levels can get heavily disturbed or impossible due to the high variability of the backscatter profile in height. In general, the detection of MLH is only unambiguously possible for very well-mixed deep layers with a significant and vertically uniform profile of aerosol backscatter.
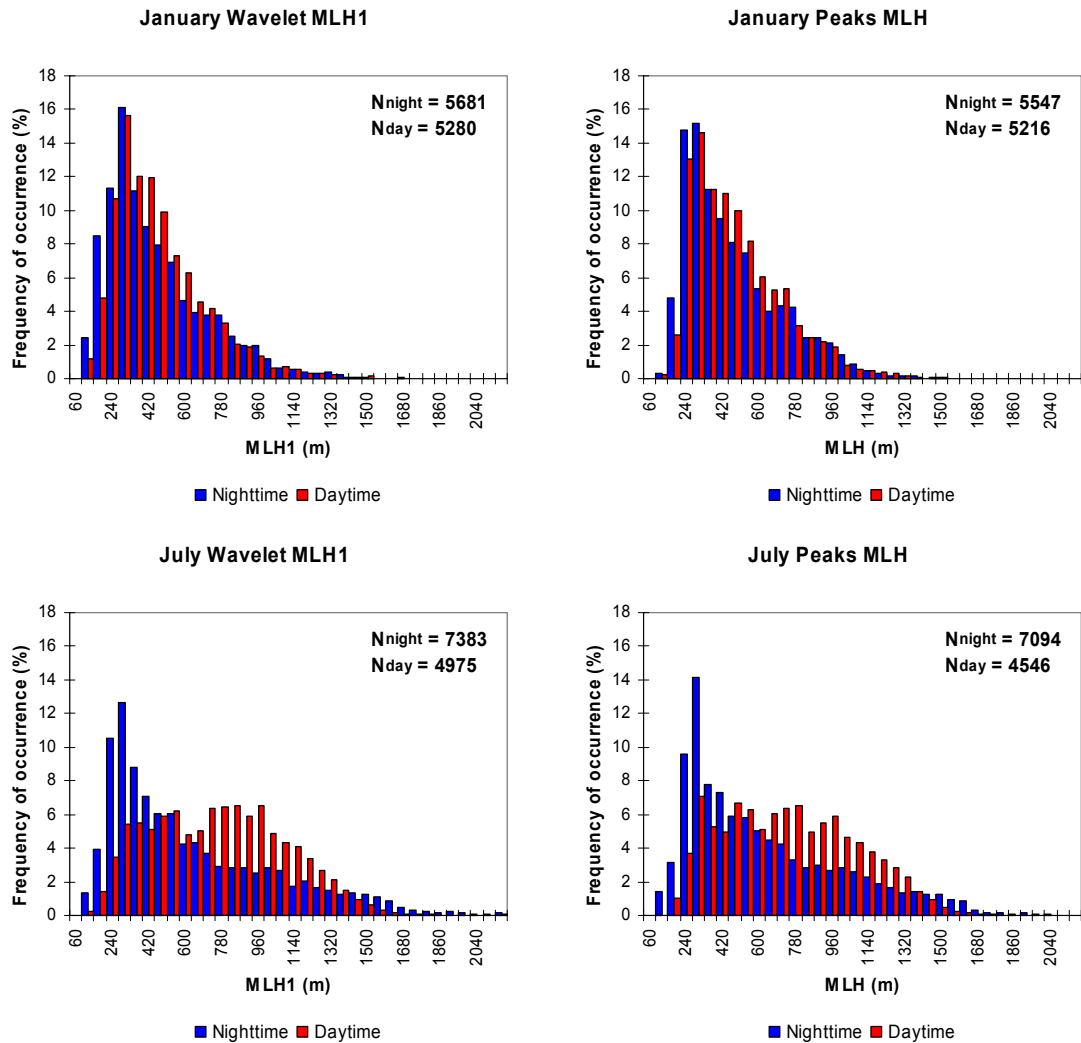
FIGURE 6.6. Histograms of the MLH frequency of occurrence for January (upper panels) and July (lower panels) in De Bilt, 2000 – 2005. MLH detections are carried out with MLH algorithms Wavelet (left) and Peaks (right). A distinction is made between nighttime (18 – 06 UTC) detections, depicted by the blue bars, and daytime (06 – 18 UTC) detections, depicted by the red bars. A bin size of 60 metres is used. The first bin consists of detections between 0 and 60 m.

The histograms in Figure 6.6 do not contain any information about the distribution of the quality indices, as all detections are considered. For the July daytime detections of Wavelet MLH1, the frequency of occurrence of the three different quality indices within this total picture is shown in Figure 6.7. It is clear that mainly the detections with a 'Poor' and 'Weak' quality index contribute to the specific shape and the observed maxima in the total distribution. The frequency of occurrence of the 'Good' quality index shows more shallow MLH detections, with a maximum in the bin between 300 and 360 m. This implies that deeper mixing layers generally coincide with MLH detections of a lower quality. This supports the assumption of a more reliable mixing layer height estimation for shallow cases in autumn and winter The Peaks MLH detections (not shown) show the same general behavior with respect to the quality indices as the Wavelet MLH1 in Figure 6.7.
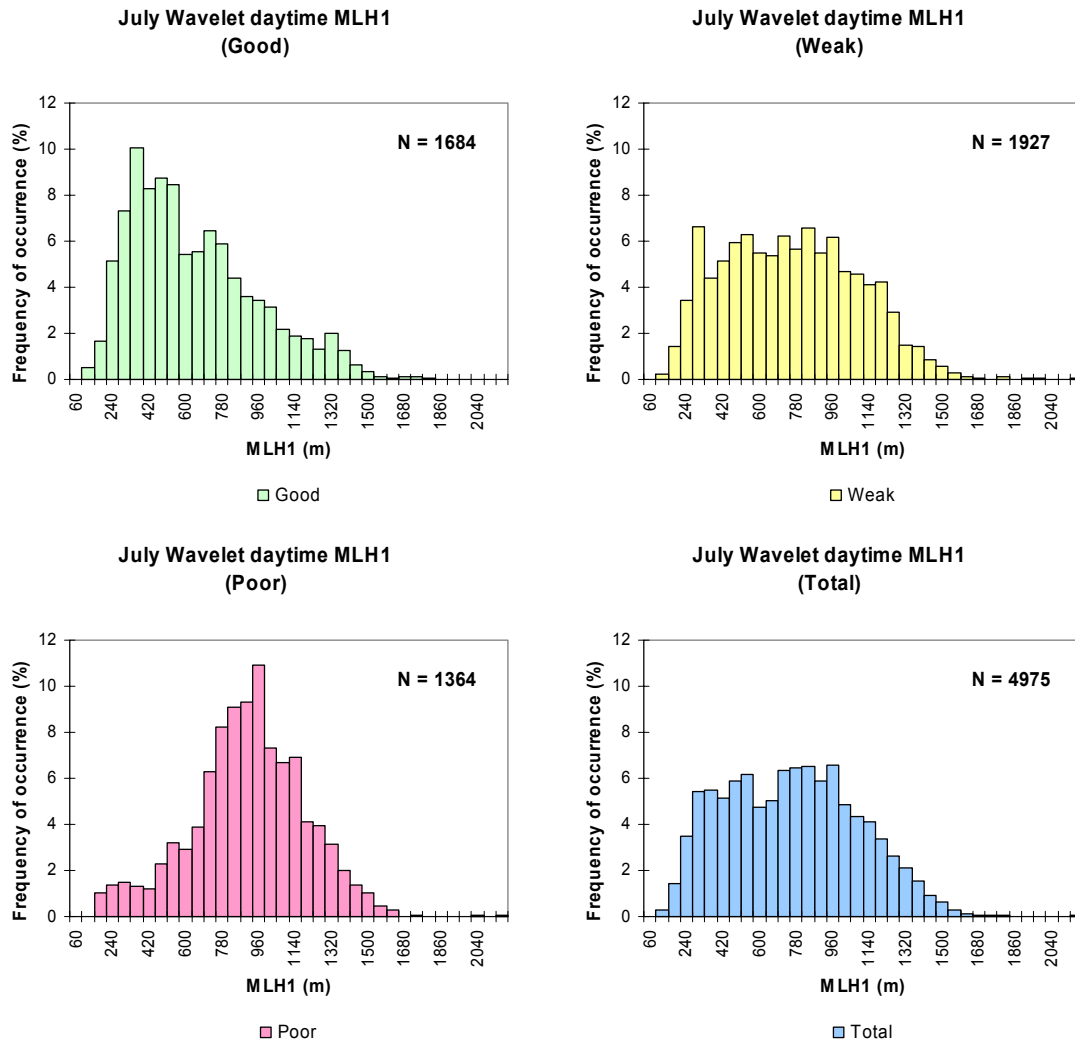
FIGURE 6.7. Histograms of MLH distributions for July in De Bilt, 2000 – 2005. Results are depicted for daytime detections, for 'Good' (=green), 'Weak' (=yellow) and 'Poor' (=red) quality indices, and for the total number (=blue) of detections.

6.2.5   Summary of the algorithm intercomparison

The overall performance assessment of the ceilometer MLH algorithms has indicated that there is no distinct advantage for one of the two algorithms. The overall detection rate, i.e. irrespective of the quality index, ranges between 40.7 % and 57.7 % for Peaks MLH and between 42.0 % and 60.8 % for Wavelet MLH1. The lowest detection rates are observed in winter, then the number of events with clouds and precipitation is the largest. On the other hand, the relative contribution of detections with the highest quality index ('Good') is the largest in autumn and winter months, roughly 40 to 65 % of the total number of detections. The most important reason for this enhanced quality is the shallow MLH which is generally observed for these months. The LD-40 backscatter signal often shows an enhanced variability in height for higher levels (especially for 750 m and higher), which implies that the detection of MLH is more reliable for shallow mixing layers.

6.3 Comparison with other measurement platforms

The previous section gave insight in the internal consistency and detection rates of the two algorithms under different circumstances. In this section a comparison to some other platforms for mixing layer height estimation is presented to assess the skills of the LD-40 MLH detections. Firstly, MLH estimates from the 12 UTC radiosonde observations in De Bilt for the period 2000 – 2005 are used. Secondly, MLH observations carried out by the wind profiler in Cabauw and the frequency of occurrence distributions of RIVM MLH are discussed.

6.3.1 Radiosonde

A comparison of MLHs estimated by the LD-40 algorithms and by the Richardson bulk method and Parcel method applied to 12 UTC radiosonde profiles in De Bilt, is shown in Figure 6.8. The same period as before is considered, i.e. 2000 – 2005.
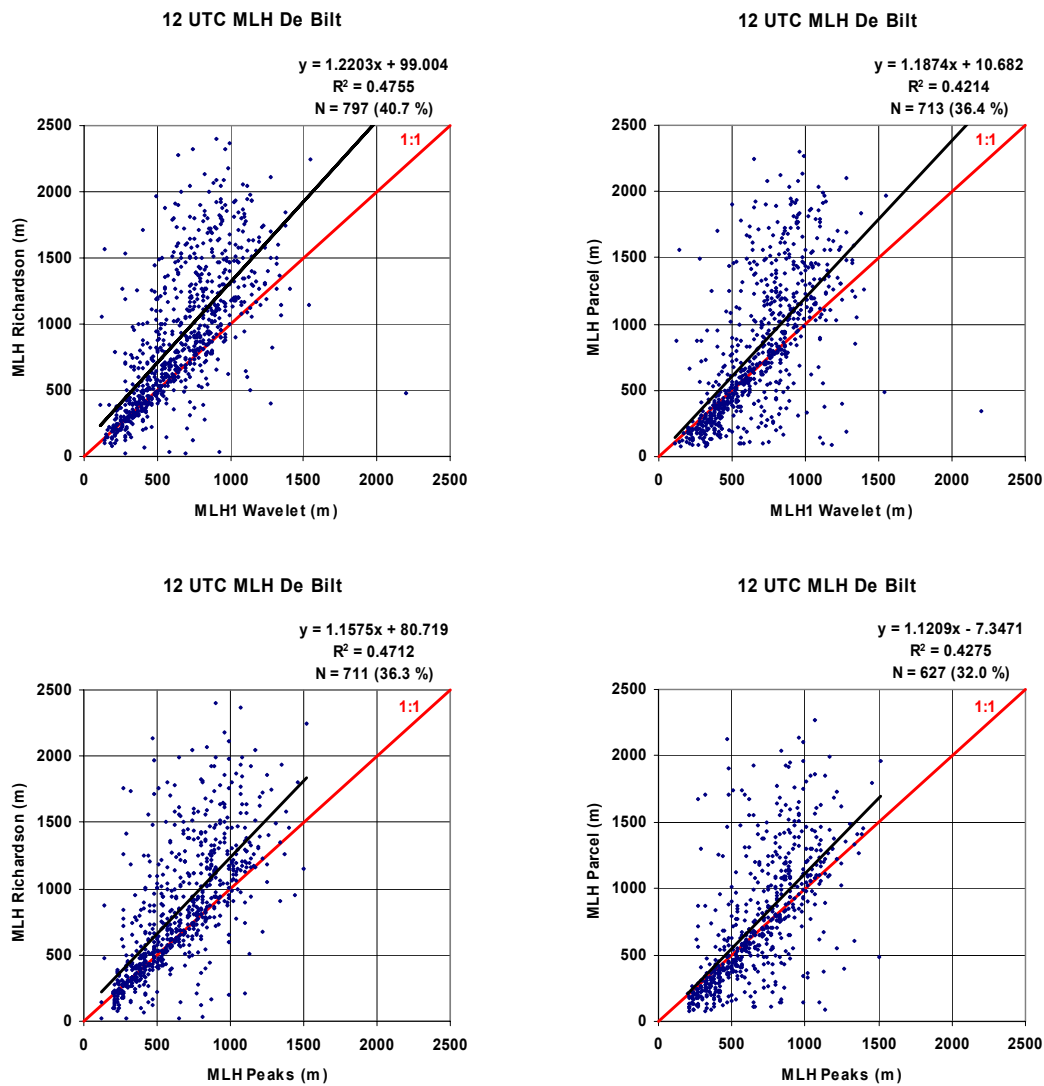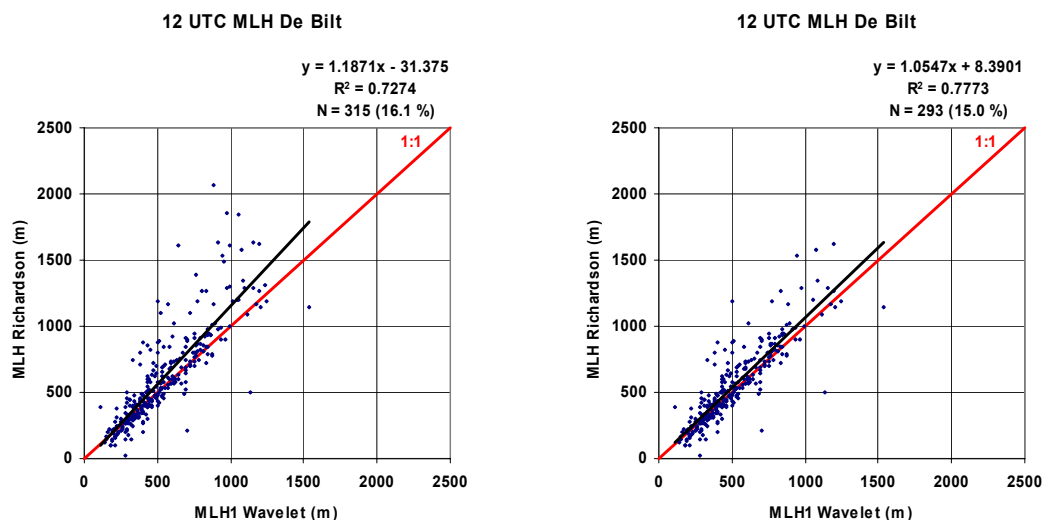

FIGURE 6.8. Scatter plots for LD-40 Wavelet MLH1 (upper panels) and Peaks MLH (lower panels) vs. 12 UTC radiosonde MLH estimates by the Richardson bulk method (left) and Parcel method (right), for De Bilt, period 2000 – 2005. LD-40 estimates are considered at 11:40 UTC, shortly after the launch time of the 12 UTC radiosonde.

The 12 UTC radiosonde is mostly launched between 11:15 and 11:30 UTC, so that it arrives at the 500 hPa level around 12:00 UTC. Therefore, the 11:40 UTC MLH estimates from the LD-40 are used in the comparison to guarantee a better collocation of measurements in the boundary layer.

From Figure 6.8 it is clear that the agreement between the LD-40 and the radiosonde is poor, in particular for values of LD-40 MLH above 500 m a lot of scatter is observed. The MLH derived by the radiosonde methods is mostly higher with respect to the LD-40 estimates. A significant amount of scatter is also seen on the other side of the $y = x$ line for the comparison of the LD-40 MLH algorithms with the Parcel method. Correlation coefficients calculated for the regression analyses are very similar, with values of 0.42 and 0.43 for the comparison Wavelet (LD-40) and Peaks (LD-40) vs. Parcel (radiosonde) to 0.48 and 0.47 for the comparison Wavelet (LD-40) and Peaks (LD-40) vs. Richardson bulk (radiosonde). Note that the number of Wavelet detections coinciding with a valid radiosonde estimate is larger than the number of Peaks detections, while the slope of the linear fit deviates more from the $y = x$ line.

12 UTC MLH De Bilt

y = 1.1871x - 31.375
R² = 0.7274
N = 315 (16.1 %)

12 UTC MLH De Bilt

y = 1.0547x + 8.3901
R² = 0.7773
N = 293 (15.0 %)

FIGURE 6.9. Scatter plots for LD-40 Wavelet MLH1 vs. 12 UTC radiosonde MLH estimates by the Richardson bulk method, for De Bilt, period 2000 – 2005. In the left panel only detections with a 'Good' quality index are shown. In the right panel, in addition detections are omitted if the coinciding estimate of radiosonde MLH is above the SNR stop level of the ceilometer.

In the left panel of figure 6.9 only the Wavelet MLH1 detections with the highest ('Good') quality index are shown. A major improvement in agreement between the LD-40 and the radiosonde is seen compared to Figure 6.8. A lot of the scatter has disappeared, resulting in a value for R² of 0.73, while the linear fit $y = ax + b$ obtains parameters $a = 1.19$ and $b = -31$ m. 'Good' LD-40 MLH detections for which the radiosonde MLH was reported above the LD-40 SNR stop height are additional omitted in the right panel of the figure. This selection is made in order to gain insight in the improvements that can be made in the intercomparison by the rejection of a certain class of detections. The linear fit and correlation coefficient again get better, obtaining values of $a = 1.05$, $b = 8$ m and R² = 0.78. The results of the regression analyses carried out for other combinations of LD-40 and radiosonde methods than those shown in Figure 6.9, are listed in Table 6.4.

Generally, the correlation coefficient R^2 of the l.s.q. linear fit is slightly higher for Wavelet MLH1 than for Peaks MLH, whereas the fit for the analyses of Wavelet MLH1 is steeper and deviates more from the $y = x$ line. The behavior for more strict quality criteria is similar for all combinations of methods. For the LD-40 MLHs with a 'Good' quality index (QI) the correlation coefficient ranges between 0.59 and 0.73. However, the analysis is based only on 14 to 17 % of the total number of detections. For the additional criterion introduced above ('Good QI and $MLH_{sonde} < h_{SNR}$'), a small increase of the correlation coefficient is again achieved, for a relative low number of additionally rejected points. In general, it appears that a lot of scatter observed above the $y = x$ lines in Figure 6.8 coincide with cases in which LD-40 MLH was underestimated with respect to radiosonde MLH because the SNR stop level was too low due to the variable character of the aerosol backscatter signal. This is seen in the results for the linear fit and correlation coefficient for the criterion '$MLH_{sonde} < h_{SNR}$'. Between 6 and 12 % of all 1958 cases analysed at 12 UTC in the period 2000 – 2005 are affected by the limited vertical range of the LD-40 for MLH estimation ($MLH_{sonde} < h_{SNR}$). That corresponds to 20 to 30 % of 'All detections', but on the other hand only 3 to 8 % of the 'Good' detections are affected.

TABLE 6.4 Results of the regression analysis for various combinations of LD-40 (Wavelet, Peaks) and radiosonde (Parcel, Richardson) MLH estimation algorithms, for coinciding 12 UTC detections in De Bilt, period 2000 – 2005. Criteria for selection of the cases are listed in the first column.
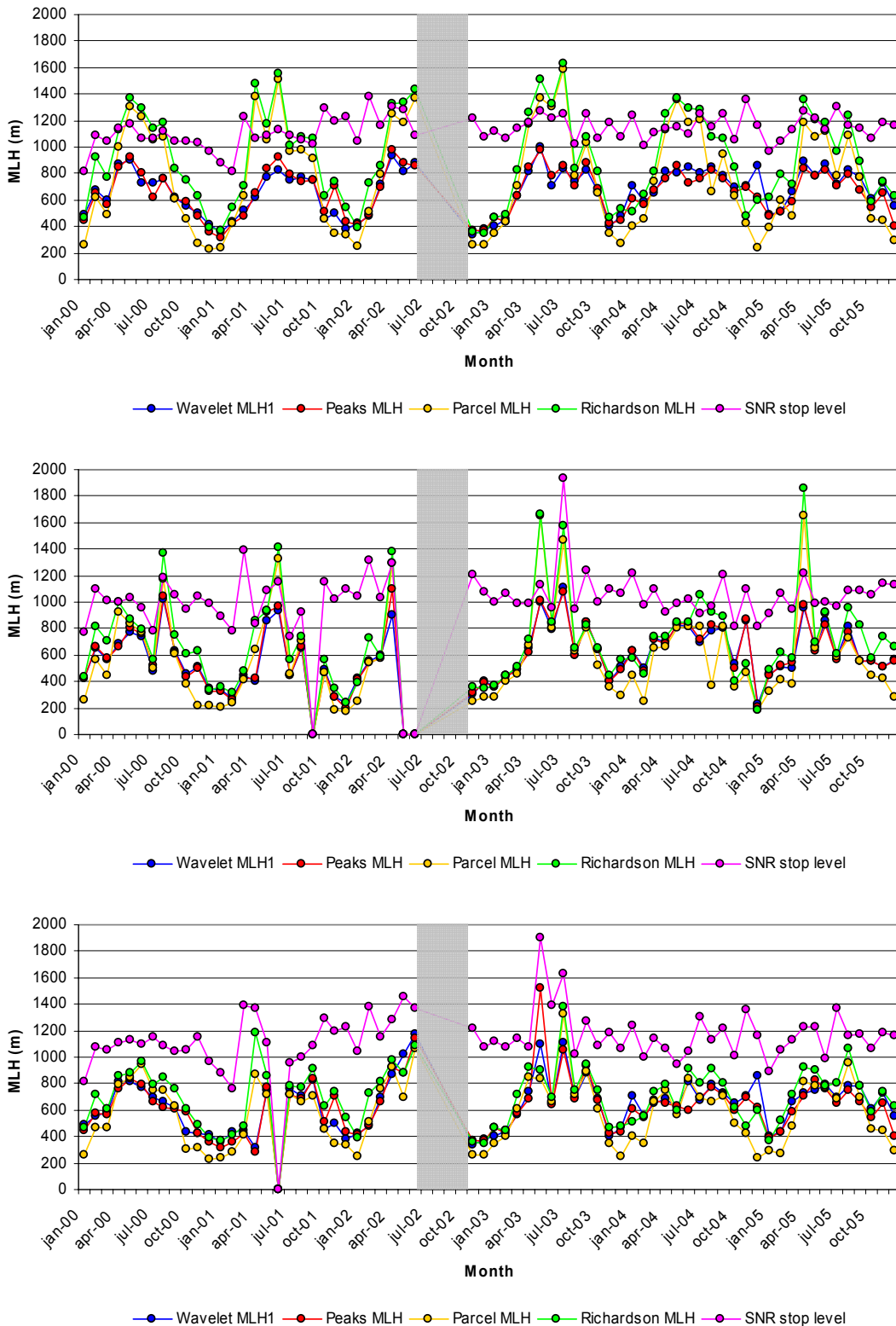
	Radiosonde			
	Parcel MLH		Richardson MLH	
	a, b, R^2	# cases (of total)	a, b, R^2	# cases (of total)
LD-40 ceilometer				
All detections				
Wavelet MLH1	1.19, 11, **0.42**	713 (36.4 %)	1.22, 99, **0.48**	797 (40.7 %)
Peaks MLH	1.12, -7, **0.43**	627 (32.0 %)	1.16, 81, **0.47**	711 (36.3 %)
'Good' QI				
Wavelet MLH1	1.09, -97, **0.67**	275 (14.0 %)	1.19, -31, **0.73**	315 (16.1 %)
Peaks MLH	0.91, -29, **0.59**	295 (15.1 %)	0.97, 54, **0.62**	338 (17.3 %)
$MLH_{sonde} < h_{SNR}$				
Wavelet MLH1	0.82, 69, **0.47**	525 (26.8 %)	0.88, 133, **0.56**	558 (28.5 %)
Peaks MLH	0.87, 26, **0.51**	501 (25.6 %)	0.90, 106, **0.56**	538 (27.5 %)
'Good' QI and $MLH_{sonde} < h_{SNR}$				
Wavelet MLH1	0.93, -33, **0.68**	262 (13.4 %)	1.05, 8, **0.78**	293 (15.0 %)
Peaks MLH	0.84, -5, **0.59**	285 (14.6 %)	0.88, 75, **0.64**	312 (15.9 %)

Besides the enhanced variability of the backscatter signal, a second possible source for differences in MLH estimation is related to the different principles of measurement. The ceilometer needs an atmospheric constituent as a tracer and directly measures the height up to which this tracer is dispersed, while the radiosonde determinations are made from an analysis of the profiles of potential temperature and horizontal wind speed. If other sources than local ones contribute to the measured backscatter, e.g. caused by advected or accumulated aerosol layers or cloudy air, the two methods can disagree very easily.

Furthermore, the presence of a deep inversion or a decoupled layer, as well as an inaccurate collocation of the measurements in time or space, can generate errors in MLH estimation.

Finally, time series of monthly mean 12 UTC mixing layer height as estimated by the LD-40 and radiosonde are shown in Figure 6.10, for De Bilt in the period 2000 – 2005. All coinciding cases have been used, and are split up in three classes according to the different criteria that were introduced above. Only the combination of criteria that is listed in the last three rows of Table 6.4, 'Good' QI and $MLH_{sonde} < h_{SNR}$, is not considered here because it is almost similar to the 'Good' QI. The shaded area in the summer and autumn of 2002 coincides with a period during which KNMI did not launch radiosondes frequently. Hence, this period is not considered.

Note the annual cycle in MLH that is visible in all of the panels in Figure 6.10. It should be remarked that the lines for Wavelet and Peaks MLH are often on top of each other. If no coinciding cases are available in the considered month, all MLHs and the SNR stop level are set to zero in the figure. The upper panel shows an overestimation of LD-40 MLH in winter compared to the Parcel method and a very evident underestimation of LD-40 MLH in summer with respect to the MLH determined by the Parcel and Richardson bulk methods. The value of the mean radiosonde MLH is also beyond the mean SNR stop level for most of the spring and summer months. An improvement is seen in the middle and lower panels where the LD-40 and radiosonde MLHs are much closer to each other throughout the complete period. Hence, the application of quality criteria improves the intercomparison results. The outliers which are seen in the middle and lower time series coincide with months in which only a few detections are available.
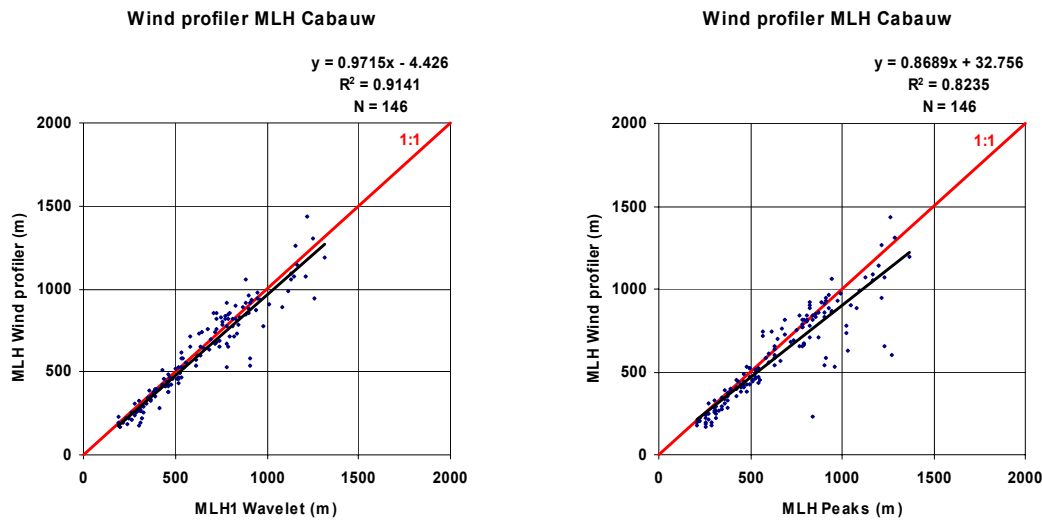
FIGURE 6.10. Monthly mean 12 UTC MLH time series for coinciding detections of LD-40 Wavelet MLH1 (blue), LD-40 Peaks MLH (red), radiosonde Parcel MLH (purple) and radiosonde Richardson MLH (green). Shown are: all coinciding detections (upper panel, N = 602), detections with the highest ('Good') quality index for Wavelet MLH1 (middle panel, N = 270), detections for which Richardson MLH is below the SNR stop level (lower panel, N = 444). The shaded area coincides with a period with almost no radiosonde data, and is therefore left out of consideration.
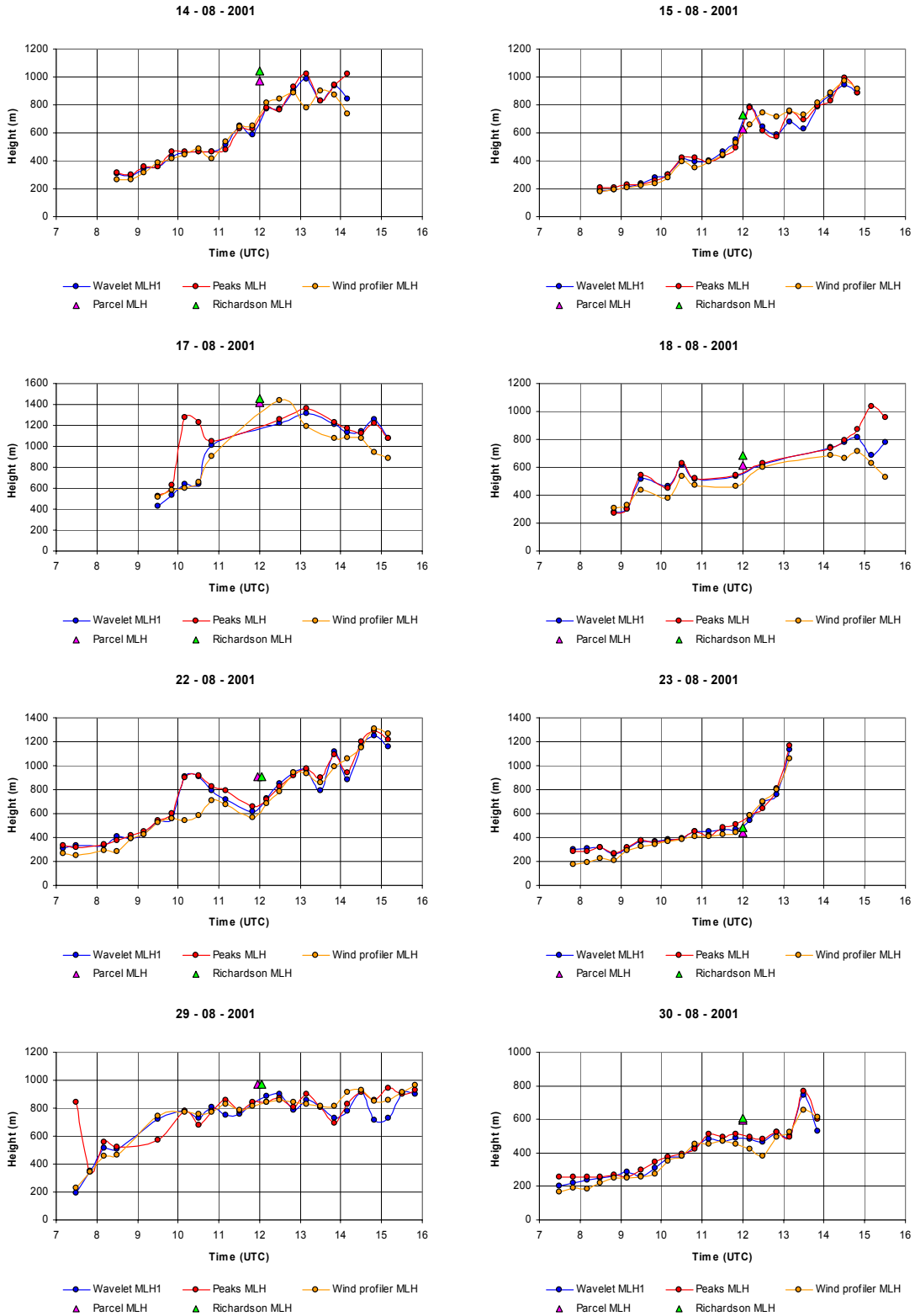
6.3.2 Wind profiler

Eight days in August 2001 are used for the comparison between MLH estimated by the LD-40 and the wind profiler, both located in Cabauw. Days were only selected if at least half of the number of wind profiler detections during the period 07 – 16 UTC were present simultaneously with MLH detections from either the Peaks or the Wavelet algorithm. Only days containing a well-defined development of the mixing layer remained in the analysis. Wind profiler estimates of MLH are available continuously for the months August and September 2001, because of the first BBC (Baltex Bridge Campaign) campaign that was organised around Cabauw during this period (Crewell et al., 2004). The eight days considered here are August 14, 15, 17, 18, 22, 23, 29 and 30, 2001.

Wind profiler MLH Cabauw

$y = 0.9715x - 4.426$
$R^2 = 0.9141$
$N = 146$

Wind profiler MLH Cabauw

$y = 0.8689x + 32.756$
$R^2 = 0.8235$
$N = 146$

FIGURE 6.11. Scatter plots for LD-40 Wavelet MLH1 (left) and Peaks MLH (right) vs. wind profiler MLH, in Cabauw. A total of 146 detections are used during August 14, 15, 17, 18, 22, 23, 29 and 30, 2001.

The scatter plots for all 146 simultaneous detections during these days are shown in Figure 6.11. Again note the small scatter for low MLHs up to approximately 500 m. For higher MLHs, the amount of scatter increases, particularly for the comparison with LD-40 Peaks MLH. The regression coefficients for the l.s.q. fit over the entire range are $a = 0.97$ and $b = -4$ m for Wavelet MLH1 and $a = 0.87$, $b = 33$ m for Peaks MLH respectively. Corresponding correlation coefficients are 0.91 and 0.82, respectively. If only the LD-40 detections with a 'Good' quality index are taken into account, the correlation coefficients become 0.95 for Wavelet MLH1 and 0.77 for Peaks MLH. So in general, the comparison with Wavelet MLH1 has less scatter and shows better agreement with the wind profiler estimates than the Peaks MLH detections.

An overview of all cases used is presented in the MLH time series in Figure 6.12. Note the high consistency of the estimates for low MLHs (< 500 m), which is nicely illustrated on August 15, 22 and 30. Whereas the early morning (low) detections agree very well, the higher detections that follow later on the day diverge more. This is possibly partly the result of the aforementioned increasing variability of the aerosol backscatter signal with height, measured by the LD-40.

FIGURE 6.12. MLH time series for the eight days for which the LD-40 and wind profiler MLH are compared in Figure 6.11. Indicated are: coinciding estimations of LD-40 Wavelet MLH1 (blue dots), Peaks MLH (red dots) and wind profiler MLH (orange dots), all in Cabauw, and the radiosonde MLH estimated by the Parcel (purple triangle) and Richardson bulk (green triangle) methods in De Bilt.

The LD-40 measurements on August 17 report a developing cloud layer between 10:30 and 14:00 UTC, with its cloud base located between approximately 1030 and 1400 m. Between 10:50 and 12:30 UTC, no coinciding detections occur for the considered methods. The building up of this cloud layer also seems to be the direct cause for the disagreement of Peaks MLH compared to Wavelet MLH1 and the wind profiler MLH, showing an absolute difference of roughly 600 m at 10:10 and 10:30 UTC. These detections are also observed at the right side of the $y = x$ line in the right panel of Figure 6.11, as main cause of the lower correlation coefficient for Peaks MLH, together with the outliers on August 18 and August 29.

Another remarkable feature in Figure 6.12 is the fluctuating and diverging LD-40 MLH with respect to the wind profiler MLH between 10 and 12 UTC on August 22. A pronounced advected aerosol layer confuses the LD-40 algorithms here. The base of this layer sets in near the top of the preceding mixing layer top around 09:30 UTC and slowly merges with the mixing layer during the following two hours. Eventually, after 12 UTC, the MLH estimates of both instruments again agree well.

6.3.3 RIVM lidar

The frequency of occurrence of the lowest RIVM lidar MLH estimate during the observational period in Bilthoven (January, 1999 – February, 2001) is presented in Figure 6.13, for all available detections in January and July. The overall detection rate for this mixing layer height, not corrected for periods without data, is 81 % for January and 85 % for July. Because the MLH estimates are not checked on quality, only the frequency of occurrence of the MLH is considered here. This gives a global impression of the behavior of the RIVM MLH algorithm. The large number of detections in the RIVM histogram with respect to the histograms of LD-40 MLH (Figure 6.6) is related to the higher detection rate as well as to the higher temporal resolution of the RIVM algorithm (section 4.2).
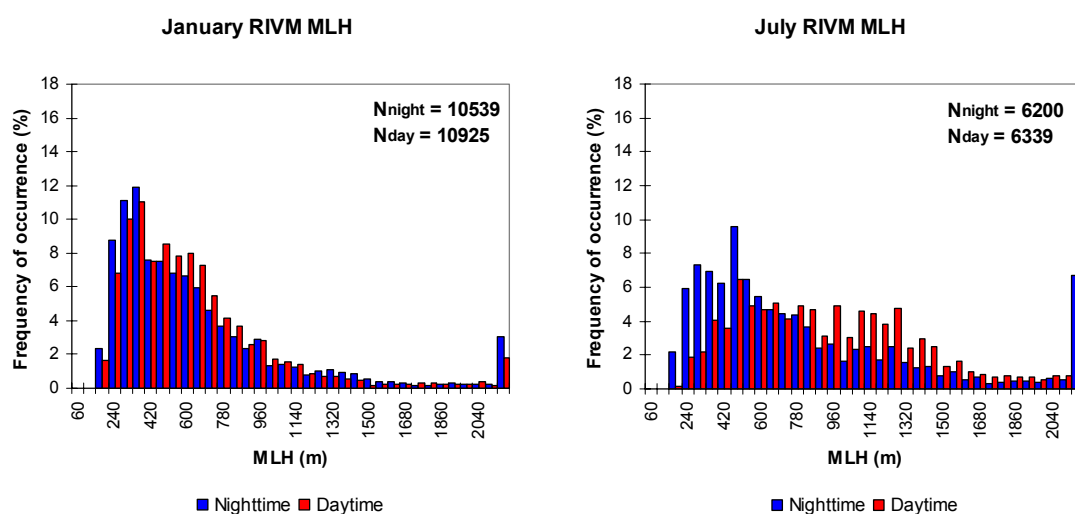

FIGURE 6.13. Same as Figure 6.6, but for the RIVM first MLH. The bars at the right end of the histograms denote the contribution of detections between 2100 and 3000 m.

Compared to the frequency distributions of Peaks and Wavelet in the same months, the graphs for the RIVM MLH are much more spread out and also show a significant contribution of higher MLHs. Not only is the amount of daytime RIVM detections between 2100 and 3000 m substantially higher (approximately 2 % for January and 7 % for July), the daytime MLH detections in July between 1080 and 1500 m also show a striking difference with respect to the LD-40 MLH values. The difference is less evident for January.

A possible explanation of the high detection rates and shift towards higher MLH in the summer histogram of the RIVM MLH is the ability of the RIVM algorithm to detect MLH in or beyond cloud layers. Whereas the LD-40 MLH algorithms are terminated if the MLH is not detected below the first cloud base, the RIVM algorithm often reports MLH around decreasing backscatter signatures on top of detected cloud bases. More specifically, 10 % and 19 % of all RIVM (lowest) MLH detections in January and July are detected above the estimated RIVM cloud base, respectively. However, if a correction is applied for the RIVM MLH estimates above a cloud base, the histogram resembles the LD-40 histogram only slightly better (not shown). The lower sensitivity of the ceilometer compared to the sensitivity of the research lidar probably also partly explains these differences.

6.3.4 Summary of the comparison with other measurement platforms

The overall comparison of LD-40 MLH estimates with radiosonde MLH estimates gives poor results. In particular for values of LD-40 MLH above 500 m much scatter is observed. The MLH derived by the radiosonde methods is mostly higher with respect to the LD-40 estimates. This is related to the inability of the LD-40 MLH algorithms to detect the top of deep mixing layers, caused by the enhanced variability of the backscatter signal in height. Many of the corresponding LD-40 detections have a 'Weak' or 'Poor' quality index. Hence, a distinction can be made between reliable and unreliable detections. The agreement (value of R^2) between both measurement platforms increases if only detections with a 'Good' quality index are considered. On the other hand, this selection reduces the detection rate from 30 – 40 % to about 10 – 20 %. The best agreement is generally achieved in the comparison between LD-40 Wavelet MLH1 and radiosonde MLH estimated by the Richardson bulk method, although the differences with the Peaks and Parcel methods are very small.

Diverging detections in the MLH comparison between the LD-40 and wind profiler in Cabauw have an assignable cause, at least for the 8 days considered in this section. A good agreement is seen for low MLHs (up to approximately 500 m), for higher values the variability of the LD-40 backscatter signal seems to deteriorate the accuracy of the detections. For the 146 cases considered, correlation coefficients of 0.91 and 0.82 are found for Wavelet MLH1 and Peaks MLH, respectively.

The MLH frequency of occurrence in January and July has been discussed with respect to the RIVM lidar. Because the RIVM MLH time series are not checked on quality the analysis of the absolute values is difficult to interpret. Compared to the histograms for Peaks MLH and Wavelet MLH1, much more high MLHs are found particularly for the

July daytime detections. Whereas the LD-40 reports hardly any occurrence of MLHs above 1500 m, the RIVM lidar shows a significant contribution above this height, and even about 7 % of the MLHs is reported between 2100 and 3000 m. This striking difference is possibly partly caused by the fact that the RIVM algorithm is able to report MLH on top of a cloud base, whereas the LD-40 algorithms do no report MLH beyond a cloud base. Furthermore, the ceilometer is less sensitive than the RIVM lidar, which frequently hinders the estimation of higher MLHs, as we have seen in the case studies in chapter 5. These reasons possibly also explain the high detection rates of 80 to 85 % for the RIVM lidar lowest MLH estimate.

6.4   Summary MLH algorithm assessment

The Peaks and Wavelet algorithms for MLH determination from the LD-40 ceilometer backscatter profiles give very similar results compared to each other (section 6.2) and also in comparison with other measurement platforms (section 6.3). Together with the small differences between both algorithms in the case studies (chapter 5), this strong agreement gives confidence in the MLH estimation from the LD-40 backscatter profiles. On the other hand it is therefore more difficult to select one of the two MLH algorithms for operational implementation, because of the minor advantages and disadvantages of both algorithms.

The most important problem, which exists for both algorithms, is the limited range of detection. This is mainly observed in spring and summer season, when the aerosol backscatter profile shows more often a strongly enhanced variability in the mixing layer with increasing height. This causes the algorithms to detect faulty MLH levels, particularly for deep convective mixing layers. E.g., a typical example was shown in section 5.2.3 for which the radiosonde and wind profiler MLH estimates were significantly higher than the SNR<1 stop level. This implies the inability of the LD-40 to detect mixing layer height in these cases. In section 6.3, it was shown that the correlation between the LD-40 and radiosonde MLH at 12 UTC increases if these cases are omitted.

Because of the incomplete overlap of the LD-40 beams in the lowest 1125 m of its vertical domain, a correction is applied to the measured backscatter profiles. The lowest range gate used for the Peaks and Wavelet MLH algorithms in this study is set to 90 m. Therefore, the algorithms are not able to detect mixing layer tops below this level, which is a commonly known problem with the detection of very shallow (e.g. nocturnal, stable) MLHs by a bi-axial lidar system. Furthermore, for the Wavelet algorithm, a distance of a/2 must be added to this height of 90 m to obtain the height at which a wavelet transform with a dilation 'a' is defined. On the other hand, the Peaks algorithm is preceded by a vertical smoothing over 135 m which decreases the strength of the negative aerosol gradients corresponding to the MLH. This can result in an inability of the algorithm to detect MLH successfully at lower levels. Summarised, both ceilometer MLH algorithms have problems with the detection of a mixing layer height below approximately 150 m, although this is also dependent on the available amount of aerosol near the surface.

There exists also no clear distinction between the two MLH algorithms when the monthly mean diurnal cycle (section 6.3.1) and the monthly mean MLH detection rates (section 6.3.2) are considered. The mean diurnal cycles resemble each other well, but are both significantly lower than expected in spring and summer due to the inability of the detection of the top of deep mixing layers. The Peaks and Wavelet algorithms report a successful MLH detection in roughly 40 – 60 % of the total number of cases, dependent on the considered month. The Wavelet algorithm shows slightly higher correlation coefficients in the comparison with other measurement platforms (radiosonde and wind profiler) although the differences are only small (section 6.3). On the other hand, Wavelet MLH1 deviates more from the $y = x$ line in the comparison with the radiosonde over the entire range, but more estimations are taken into account than for Peaks MLH. MLH estimates as derived from measurements of these other instruments also contain uncertainties, but as there is no better reference material available, the assessment of the LD-40 MLH algorithms is based on these results.

An advantage of the Wavelet MLH algorithm is the possibility to derive the entrainment zone thickness (EZT) at the same time (e.g. Brooks, 2003). Using the Wavelet power spectrum, it was shown that the lower and upper boundary of the EZT can be estimated from the distance between the levels showing a certain fixed percentage of the maximum wavelet power that is observed at the MLH itself. Furthermore, the Wavelet algorithm is capable of detecting small-scale structures in the convective mixing layer for some specific conditions, although in this case the backscatter data from the LD-40 has to be averaged over a smaller time interval than 10 minutes. The corresponding detections of mixing layer height are assumed to coincide with separate updraft/downdraft patterns which are seen in the aerosol backscatter contours. A discussion and some cases illustrating this special feature are presented in Appendix C.

Concerning the required CPU time for both algorithms, the Peaks algorithm is less expensive than the Wavelet algorithm. For the analysis of 20 arbitrarily chosen daily files of the LD-40 backscatter in De Bilt, all necessary calculations for one file require 0.6 ± 0.1 s for the Peaks algorithm and 2.2 ± 0.4 s for the Wavelet algorithm on a HP XW6000 workstation with a Xeon 2.4 GHz processor. This implies an average MLH calculation time of the Wavelet algorithm of almost four times the processing time of the Peaks algorithm per backscatter profile. The larger load for the Wavelet algorithm is mainly caused by the wide range of dilations and accompanying calculations which are required. The time needed for the storage of output from the MLH routines is also taken into account in the estimation of the required CPU time. These steps are very similar for both algorithms.

Based on the case studies and statistical analysis presented in chapter 5 and 6, it was shown that the quality index defined in section 4.4 is a suitable parameter to derive the reliability of the detections. It was shown that the 'Poor' detections coincide with conditions in which the mixing layer height is not unambiguously determined. Therefore, the user is advised to use data with 'Poor' quality index very reserved. The 'Weak' quality index spreads out over a large grey area of detections, in which the reliability changes from the one case to the other as was assessed by eye from the backscatter contours, the

variability of the MLH time series and by comparison to other measurement platforms. Generally, it is assumed that the 'Weak' index contains mostly reliable detections. However, without a visual inspection it can not be guaranteed that the determined mixing layer height is the correct one. Concerning the highest quality index 'Good', a strong decrease in backscatter is generally observed at the MLH and the reported value is reliable. However, when only the 'Good' index is taken into account, an estimate of the mixing layer height will be available only 20 to 30 % of the time, as is listed also in Table 6.1.

A second layer characterised by a negative backscatter gradient, MLH2, is also reported by the Wavelet algorithm. However, the MLH2 time series often shows a strong variability which is considered to be doubtful. Therefore, it is advised to consider the 'Good' detections of MLH2 only. It is observed in a large number of cases that these detections mainly coincide with the top of marked residual and advected aerosol layers. By taking into account only the 'Good' detections, the estimates of MLH2 which are caused by a strongly variable backscatter signal in height, are omitted. The Wavelet algorithm reports a detection rate for MLH2 between 15 % and 40 %, with the lowest rates in winter and the highest rates in summer. The annual cycle shows similar behavior as the evolution of the MLH1 detection rate (Table 6.1). After a selection on 'Good' detections only, the MLH2 detection rate decreases to values between 10 and 25 %. It should be noted that a 'Poor' or 'Weak' MLH1 detection can directly be followed by a 'Good' MLH2 detection, as described in the algorithm description in section 4.3.

7 Conclusions and recommendations

7.1 Conclusions

7.1.1 Mixing layer height estimation

In this report the results of a feasibility study on the retrieval of the mixing layer height (MLH) from the backscatter profiles of the LD-40 ceilometer are presented. The principle of the retrieval is based on the difference in aerosol concentration between the mixing layer with usual high aerosol concentrations, and the relative clean free atmosphere aloft. Hence, a marked negative backscatter gradient is observed at the top of the mixing layer. The maximum in the negative backscatter gradient is commonly used in ceilometer/lidar algorithms for MLH estimation. Furthermore, in the entrainment zone at the top of the (convective) mixing layer one finds alternating updrafts with high aerosol load, and relative clean downdrafts from the free atmosphere. This will result in a high variance of the time series of the aerosol backscatter signal at this level. Therefore a maximum in the variance can be used as a secondary indicator of the top of the mixing layer.

Two algorithms were developed for the estimation of MLH from backscatter profiles measured by the Vaisala-Impulsphysik LD-40 ceilometer. The LD-40 is the operational sensor for cloud base detection in the KNMI meteorological measurement network in The Netherlands, and operated at around 20 different locations. The first algorithm, called "Peaks", is based on an existing algorithm for MLH detection from lidar backscatter profiles (De Ruiter and Swart, 1991). The MLH detection is triggered on a collocation of a minimum in backscatter gradient and a maximum in backscatter variance. The second algorithm, called "Wavelet", uses the Haar wavelet function with a wide range of dilations to estimate the MLH. Both algorithms are applied to LD-40 backscatter data which are overlap corrected according to a correction profile provided by the manufacturer. The vertical range on which the algorithms are applied is limited from 90 to 3000 m. Furthermore, the upper range limit is restricted by the lowest cloud base, vertical visibility, and maximum range of detection if either of these parameters has a value lower than 3000 m. The signal-to-noise-ratio is also used for the rejection of range gates containing an unreliable signal for MLH estimation. A quality index has been introduced for the reliability of the estimated mixing layer height. Three quality classes are distinguished, 'Poor', 'Weak' and 'Good', based on the difference between the mean aerosol backscatter in a fixed height interval above and below the estimated MLH.

7.1.2 MLH algorithm performance

It is feasible to determine the MLH from LD-40 ceilometer backscatter profiles using either of the two algorithms developed, i.e. "Peaks" and "Wavelet". The findings from an assessment of the performance of the algorithms are summarised below:

- The reliability of the MLH detection is strongly connected to the variability of the backscatter signal in height in the mixing layer itself. Enhanced variability of the backscatter signal is mainly caused by the low sensitivity of the LD-40 ceilometer. This often causes problems in cases with deep mixing layers and a low aerosol load. Especially in strong convective conditions in spring and summer, the

vertical range of reliable MLH detection by the LD-40 is too limited. On the other hand, backscatter profiles that show a fairly constant and sufficient amount of aerosol backscatter in the mixing layer result most of the time in a reliable (i.e. quality index 'Good' or 'Weak') detection of the MLH.

- A deep inversion layer at the top of the mixing layer can cause a high temporal variability of MLH estimates.
- The afternoon decay of the convective mixing layer is a problem for both ceilometer MLH algorithms. The large amount of aerosol in the residual layer on top of the decaying mixing layer reduces the contrast with the mixing layer and hence decreases the possibility of a correct MLH detection.
- The ceilometer MLH algorithms have a problem with the detection of very shallow MLHs. This is especially observed during periods with a nocturnal (stable) layer. The problem is probably caused by the lowest detection height of the LD-40 (i.e. 90 m) and perhaps also by the poor numerical resolution and truncation of the backscatter values in the KNMI data format.

A statistical analysis of the results of both algorithms was carried out for a period of six years (2000 – 2005) of ceilometer data from De Bilt, leading to the following conclusions:

- The shape of the mean diurnal cycle of MLH estimates satisfies the expected shape, but the afternoon values are significantly underestimated during spring and summer months. This is mainly caused by the limited range of the LD-40 in these months. This conclusion is supported by the frequency of occurrence distributions of LD-40 MLH estimates, which lack values above 1250 m.
- The success rate for Peaks MLH and Wavelet MLH1 for all detections is between 40 and 60 % during the year. Highest success rates are found in summer, but this season also has the largest relative contribution of 'Weak' and 'Poor' detections. If only 'Good' detections of MLH are considered, the success rate decreases to 15 to 30 %.
- The overall agreement of LD-40 MLH and radiosonde MLH at 12 UTC is poor. Correlation coefficients for the comparison with the Richardson bulk method for all cases are very similar, i.e. 0.48 (Wavelet) and 0.47 (Peaks). The fit for Wavelet MLH1 deviates more from the $y = x$ line. The main reason for the poor agreement is that for high values of radiosonde MLH (i.e. above 500 m), the LD-40 MLH shows significantly lower values. This is again primarily caused by the limited vertical range of the ceilometer in spring and summer. The value for R^2 increases to 0.73 if only 'Good' detections of Wavelet MLH1 are considered, whereas a value of 0.78 is found if detections are omitted with a coinciding radiosonde MLH above the SNR stop level of the ceilometer. Around 10 % of all 1961 cases analysed at 12 UTC (period 2000 – 2005) demonstrate a limited vertical range for MLH estimation due to this problem, as recognised by a SNR stop level which is below the MLH estimate of the Richardson bulk method applied to radiosonde profiles.
- A comparison with wind profiler estimates of the MLH in Cabauw (8 days, 146 estimates) shows good agreement, expressed in correlation coefficients R^2 of 0.91

(Wavelet MLH1) and 0.82 (Peaks MLH). Scatter increases also in this comparison especially for higher values of ceilometer MLH (i.e. above 500 m).

- The MLH frequency of occurrence histograms of the RIVM lidar in Bilthoven show evident differences with the MLH histograms from the LD-40 ceilometer algorithms. Much more high RIVM MLHs are found, particularly for the summer daytime detections. However, the comparison between the two algorithms is difficult, e.g. because the RIVM algorithm has the ability to report MLH in or above cloud layers, whereas the LD-40 MLH algorithms are terminated if they are not triggered below the height of the first cloud base.

7.1.3 Algorithm selection

The cases studied in chapter 5 and the performance assessment in chapter 6 have indicated that there is only a marginal advantage of the Wavelet algorithm with respect to the Peaks algorithm. The advantages of both algorithms can be summarised as follows:

Wavelet algorithm
- Higher correlation coefficients in the comparison with MLH from radiosonde and wind profiler.
- Possibility to derive EZT from high resolution MLH estimates (Appendix C).

Peaks algorithm
- Requires less CPU time.

Taking into account these small differences and the more general nature of the Wavelet algorithm, the Wavelet algorithm is selected for the determination of mixing layer height from the Vaisala-Impulsphysik LD-40 ceilometer.

7.1.4 Use of the MLH product

Concerning the use of MLH estimates some issues should be kept in mind:

- The LD-40 ceilometer needs aerosol as a tracer for dispersion. The presence of atmospheric constituents may be also caused by other sources than local ones.
- The quality index provides a good estimate of the reliability of the MLH results. In any case the user of the MLH product should use the MLH1 estimates with a 'Good' quality index as mean mixing layer height, possibly complemented with MLH1 estimates with 'Weak' and 'Poor' quality indices. Estimates with the lowest quality index 'Poor' should be used very reserved. The variability of the MLH time series and if available the backscatter contour plot also provide an additional indication for the reliability of the MLH product.
- Jumping between different layers mostly occurs during nighttime and generally lowers the reliability of the estimated MLH time series
- In a large number of cases, MLH2 is not detected, but if present it can provide a good estimation of the top of an elevated advected layer or residual layer.

7.2 Recommendations for future research

The recommendations for future research are the following:

- The measured aerosol backscatter decreases due to the enhanced extinction of the signal above a cloud base. On the other hand, boundary layer clouds may provide a good proxy for the estimate of the actual boundary layer height. A further assessment can be helpful to distinguish between conditions in which MLH detection in the presence of clouds is possible or not.
- The raw data format (Appendix D) of the LD-40 backscatter has a higher resolution than the KNMI format. Furthermore, the backscatter values are not truncated at a lower limit of the data range. The use of this raw data format may mainly improve the reliability of the backscatter profile in the lowest 200 m of the atmosphere. A disadvantage is the inability to use the raw data within the possible future implementation of the algorithm in the KNMI sensor interface SIAM. An assessment should be made of the difference in MLH estimation for the two different types of backscatter data.
- A refined overlap correction and a correction for the ringing artifact (see Appendix D) for the LD-40 were derived by Schäfer et al. (2004) from the raw data. As the overlap correction is sometimes crucial for a proper detection of a shallow MLH and the ringing process can confuse the algorithms in the detection, further attention should be given to an appropriate correction for these instrumental artifacts.
- An assessment of the added value of additional information about the evolution of the mixing layer should be made. The user of the LD-40 MLH product plays a significant role in this process, and should give feedback to the algorithm developers whether information like e.g. MLH2, 1 minute MLH1 and EZT (Appendix C) is useful.
- An extended comparison of LD-40 and wind profiler MLH at Cabauw is desirable, to build up statistics and trace the source of failing of one or the other instrument and algorithms. Furthermore, the installation of a new SODAR system by KNMI at Schiphol Airport in April, 2006, offers the opportunity to compare SODAR MLH estimates with the estimates of MLH by a collocated LD-40. This could in particularly provide more knowledge on the capabilities of the LD-40 algorithm for estimating the shallow nocturnal boundary layer height.

7.3   Acknowledgements

8   References

Arellano, de, J.V.-G., B. Gioli, F. Miglietta, H.J.J. Jonker, H. Klein Baltink, R.W.A. Hutjes and A.A.M. Holtslag, 2004: Entrainment process of carbon dioxide in the atmospheric boundary layer. *J. Geophys. Res.*, **109**, D18110.

Asimakopoulos, D.N., C.G. Helmis and J. Michopoulos, 2004: Evaluation of SODAR methods for the determination of the atmospheric boundary layer mixing height. *Meteorol. Atmos. Phys.*, **85**, pp. 85-92.

Beyrich, F., 1997: Mixing height estimation from sodar data – a critical discussion. *Atmos. Environ.*, **31**, pp. 3941-3953.

Beyrich, F. and S.-E. Gryning, 1998: Estimation of entrainment zone depth in a shallow convective boundary layer from sodar data. *J. Appl. Meteorol.*, **37**, pp. 255-268.

Bianco, L. and J.M. Wilczak, 2002: Convective boundary layer depth: improved measurements by Doppler radar wind profiler using fuzzy logic methods. *J. Atmos. Ocean. Technol.*, **19**, pp. 1745-1758.

Bijma, J.R., 1999: XC4-SIAM Impulsphysik LD40 Ceilometer, versie 1.0, 19 oktober 1999. *Internal KNMI report*, KNMI, De Bilt, The Netherlands.

Bijma, J.R., 2006: DC4-SIAM Impulsphysik LD40 Ceilometer, versie 1.0, 15 augustus 2006. *Internal KNMI report*, KNMI, De Bilt, The Netherlands.

Brooks, I.M., 2003: Finding boundary layer top: application of a wavelet covariance transform to lidar backscatter profiles. *J. Atmos. Ocean. Technol.*, **20**, pp. 1092-1105.

Cohn, S.A., and W.M Angevine, 2000: Boundary layer height and entrainment zone thickness measured by lidars and wind-profiling radars. *J. Appl. Meteorol.*, **39**, pp. 1233-1247.

Crewell, S., H. Bloemink, A. Feijt, S. G. García, D. Jolivet, O. A. Krasnov, A. Van Lammeren, U. Löhnert, E. Van Meijgaard, J. Meywerk, M. Quante, K. Pfeilsticker, S. Schmidt, T. Scholl, C. Simmer, M. Schröder, T. Trautmann, V. Venema, M. Wendisch and U. Willén, 2004: THE BALTEX BRIDGE CAMPAIGN: An Integrated Approach for a Better Understanding of Clouds. *Bull. Am. Meteorol. Soc.*, **85**, pp. 1565-1584.

Davis, K.J., N. Gamage, C.R. Hagelberg, C. Kiemle, D.H. Lenschow and P.P. Sullivan, 2000: An objective method for deriving atmospheric structure from airborne lidar observations. *J. Atmos. Ocean. Technol.*, **17**, pp. 1455-1468.

Deardorff, J.W., G.E. Willis and B.H. Stockton, 1980: Laboratory studies of the entrainment zone of a convectively mixed layer. *J. Fluid Mech.*, **100**, pp 41-64.

Dolman, A.J., R. Ronda, F. Miglietta and P. Ciais, 2004: Regional measurement and modeling of carbon balances. in: H. Griffiths & P.J. Jarvis (Eds), The Carbon Balance of Forest Biomes.

Emeis, S., C. Münkel, S. Vogt, W.J. Müller, and K. Schäfer, 2004: Atmospheric boundary-layer structure from simultaneous SODAR, RASS, and ceilometer measurements. *Atmos. Environ.*, **38**, pp. 273-286.

Emeis, S. and M. Türk, 2004: Frequency distributions of the mixing height over an urban area from SODAR data. *Meteorol. Z.*, **13**, pp. 361-367.

Eresmaa, N., A. Karppinen, S.M Joffre, J. Räsänen and H. Talvitie, 2006: Mixing height determination by ceilometer. *Atmos. Chem. Phys.*, **6**, pp. 1485-1493.

Fischer, B.E.A., J.J. Erbrink, S. Finardi, P. Jeannet, S. Joffre, M.G. Morselli, U. Pechinger, P. Seibert and D.J. Thomson (Eds.), 1998: COST Action 710-Final Report. Harmonisation of the pre-processing of meteorological data for atmospheric dispersion models. L-2985 European Commission, Luxemburg. EUR 18195 EN (ISBN 92-828-3302-X).

Garrett, A.J., 1981: Comparison of observed mixed-layer depths to model estimates using observed temperatures and winds, and MOS forecasts. *J. Appl. Meteorol.*, **20**, 1277-1283.

Grimsdell, A.W. and W.M. Angevine, 1998: Convective boundary layer height measurement with wind profilers and comparison to cloud base. *J. Atmos. Ocean. Technol.*, **15**, pp. 1331-1338.

Hayden, K.L., K.G. Anlauf, R.M. Hoff, J.W. Strapp, J.W. Bottenheim, H.A. Wiebe, F.A. Froude, J.B. Martin, D.G. Steyn and I.G. McKendry, 1997: The vertical chemical and meteorological structure of the boundary layer in the Lower Fraser Valley during Pacific '93. *Atmos. Environ.*, **31**, pp. 2089-2105.

Hennemuth, B. and A. Lammert, 2006: Determination of the atmospheric boundary layer height from radiosonde and lidar backscatter. *Boundary-Layer Meteorol.*, **120**, pp 181-200.

Hutjes, R.W.A., 2005: Integrated observations and modeling of Greenhouse Gas budgets at the national level in The Netherlands. *Project proposal BSIK ME2 project*, Wageningen, The Netherlands.

Impulsphysik, 1998: User manual for laser ceilograph LD-25/40 Explorer/Tropopauser. Jenoptik Impulsphysik GmbH, Schenefeld, Germany.

Impulsphysik, 1999: Supplement 1 to User manual for laser ceilograph LD-25/40 Explorer/Tropopauser. Software Version V 3.4 15.12.1999 or higher. Jenoptik Impulsphysik GmbH, Schenefeld, Germany.

Lammert, A. and J. Bösenberg, 2006: Determination of the convective boundary-layer height with laser remote sensing. *Boundary-Layer Meteorol.*, **119**, pp 159-170.

Lokoshchenko, M.A., 2002: Long-term sodar observations in Moscow and a new approach to potential mixing determination by radiosonde data. *J. Atmos. Ocean. Technol.*, **19**, pp. 1151-1162.

Martucci, G., R. Matthey, V. Mitev and H. Richner, 2005: Lidar determination of mixing layer height with high resolution. *Remote Sensing of Clouds and the Atmosphere X, Proceedings of SPIE, Bellingham, WA, USA*, **Vol. 5979**, pp. 599-608.

Menut, L., C. Flamant, J. Pelon and P.H. Flamant, 1999: Urban boundary layer height determination from lidar measurements over the Paris area. *Appl. Opt.*, **38**, pp. 945-954.

Münkel, C. and J. Räsänen, 2004: New optical concept for commercial lidar ceilometers scanning the boundary layer. *Remote Sensing of Clouds and the Atmosphere IX, Proceedings of SPIE, Bellingham, WA, USA*, **Vol. 5571**, pp. 364-374.

Münkel, C., S. Emeis, W.J. Müller and K. Schäfer, 2004: Aerosol concentration measurements with a lidar ceilometer: results of a one year measuring campaign. *Remote Sensing of Clouds and the Atmosphere VIII, Proceedings of SPIE, Bellingham, WA, USA*, **Vol. 5235**, pp. 486-496.

Pul, van, W.A.J., A.A.M. Holtslag and D.P.J. Swart, 1994: A comparison of ABL heights inferred routinely from lidar and radiosondes at noontime. *Boundary-Layer Meteorol.*, **68**, pp 173-191.

RIVM, 2003: Vuurwerk tijdens de jaarwisseling van 2002/2003. *Online report*, RIVM, Bilthoven, The Netherlands.

Ruiter, de, A. and D.P.J. Swart, 1991: Automatische menghoogtebepaling met lidar. *M. Sc. Thesis Universiteit van Amsterdam*, The Netherlands.

Schäfer, K., S. Emeis, A. Rauch, C. Münkel and S. Vogt, 2004: Determination of mixing layer heights from ceilometer data. *Remote Sensing of Clouds and the Atmosphere IX, Proceedings of SPIE, Bellingham, WA, USA*, **Vol. 5571**, pp. 248-259.

Seibert, P., F. Beyrich, S.-E. Gryning, S. Joffre, A. Rasmussen and P. Tercier, 2000: Review and intercomparison of operational methods for the determination of the mixing height. *Atmos. Environ.*, **34**, pp. 1001-1027.

Sicard, M., C. Pérez, A. Comeron, J.M. Baldasano and F. Rocadenbosch, 2004: Determination of the mixing layer height from regular lidar measurements in the Barcelona area. *Remote Sensing of Clouds and the Atmosphere VIII, Proceedings of SPIE, Bellingham, WA, USA*, **Vol. 5235**, pp. 505-516.

Steyn, D.G., M. Baldi and R.M. Hoff, 1999: The detection of mixed layer depth from lidar backscatter profiles. *J. Atmos. Ocean. Technol.*, **16**, pp. 953-959.

Stull, R.B., 1988: An Introduction to Boundary Layer Meteorology. *Kluwer Academic Publishers*, Dordrecht, 665 pp.

Troen, I. and L. Mahrt, 1986: A simple model of the planetary boundary layer: Sensitivity to surface evaporation. *Boundary-Layer Meteorol.*, **37**, pp 129-148.

Vogelezang, D.H.P. and A.A.M. Holtslag, 1996: Evaluation and model impacts of alternative boundary-layer height formulations. *Boundary-Layer Meteorol.*, **81**, pp 245-269.

Wauben, W.M.F., R. Ivens and P.Y. de Vries, 2001: Specificaties AVW, versie 1.0, 13 november 2001. *Internal KNMI report*, KNMI, De Bilt, The Netherlands.

Appendix A   Spatial variation of MLH

In this section a first assessment is made of the spatial variation of MLH derived by a network of 4 LD-40- stations in The Netherlands. The spatial variation of the MLH is of particular interest to the overall BSIK ME2 WP1 goal of tracing sources and sinks of greenhouse gases on a regional scale. LD-40 backscatter data has been archived during the BBC1 measurement campaign (Crewell et al., 2004). The four stations with LD-40 backscatter measurements available for this period are Cabauw, De Bilt, Hoogeveen and Schiphol (Figure A.1). The same selection of days used in the wind profiler comparison in section 6.3.2 will be considered. This selection is extended with five more days showing a developing mixing layer without clouds in the period October 12 – 16, 2001.

FIGURE A.1. Overview of the national meteorological measurement network of KNMI in The Netherlands, 2001 (from: www.knmi.nl/˜meulenvd). The four considered stations in this section are indicated by the large blue dots.

In Figure A.2, backscatter contour plots for one case (August 30, 2001) are presented together with the Wavelet mixing layer height estimates. Cabauw, De Bilt and Schiphol are relative well collocated in the central-western part of the Netherlands, while Hoogeveen is located further eastward. Concerning the mixing layer during daytime, note that all four stations report the ML development from approximately 08 UTC until the maximum MLH1 is reached between 12 and 14 UTC.
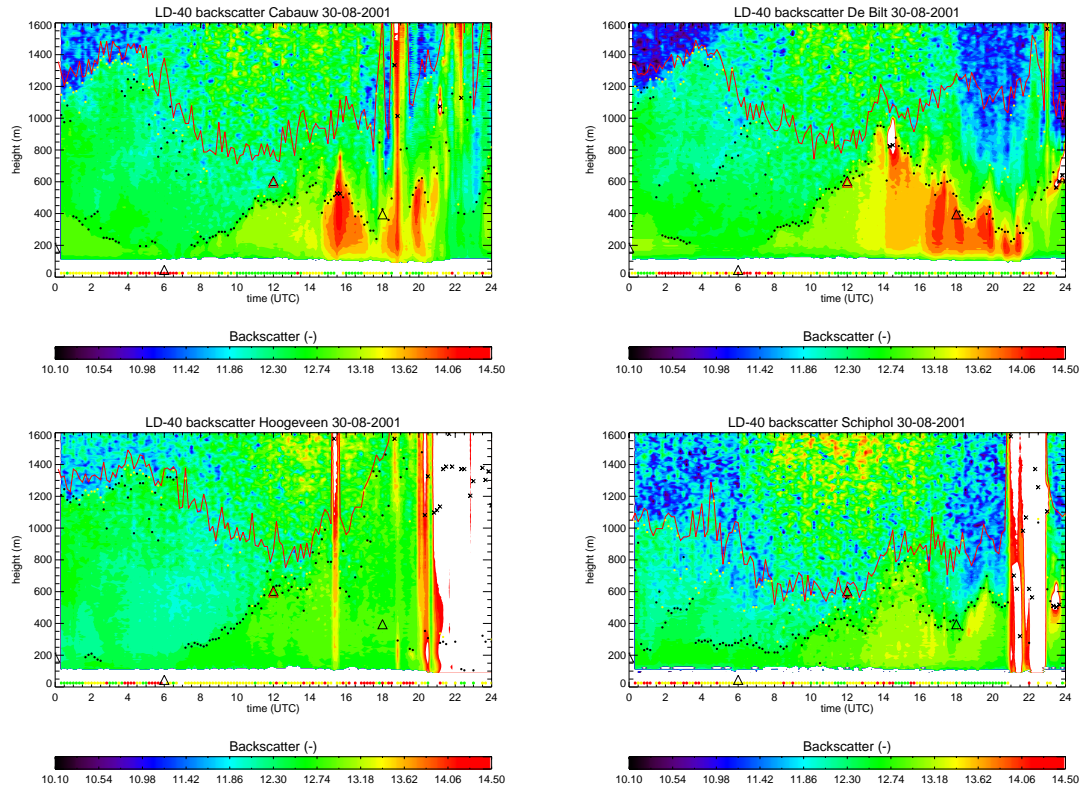
FIGURE A.2. Backscatter contour plots and corresponding Wavelet MLH estimates for Cabauw, De Bilt, Hoogeveen and Schiphol on August 30, 2001. The used symbols are listed in Table 5.1.
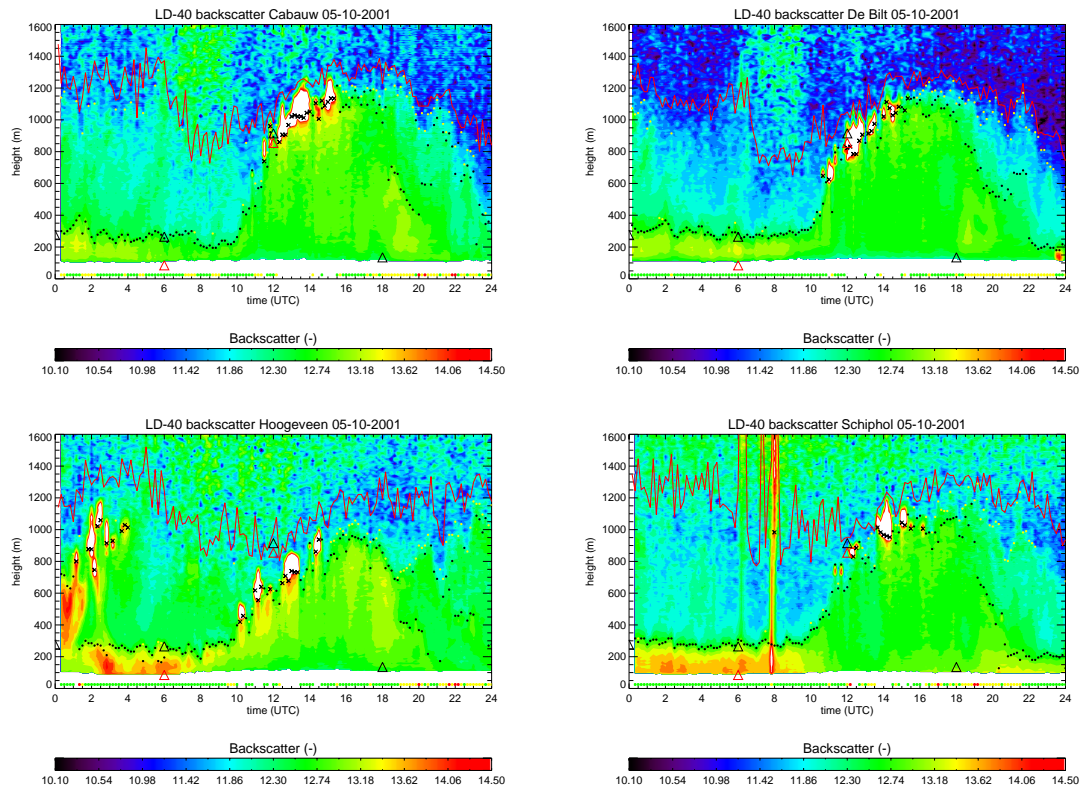

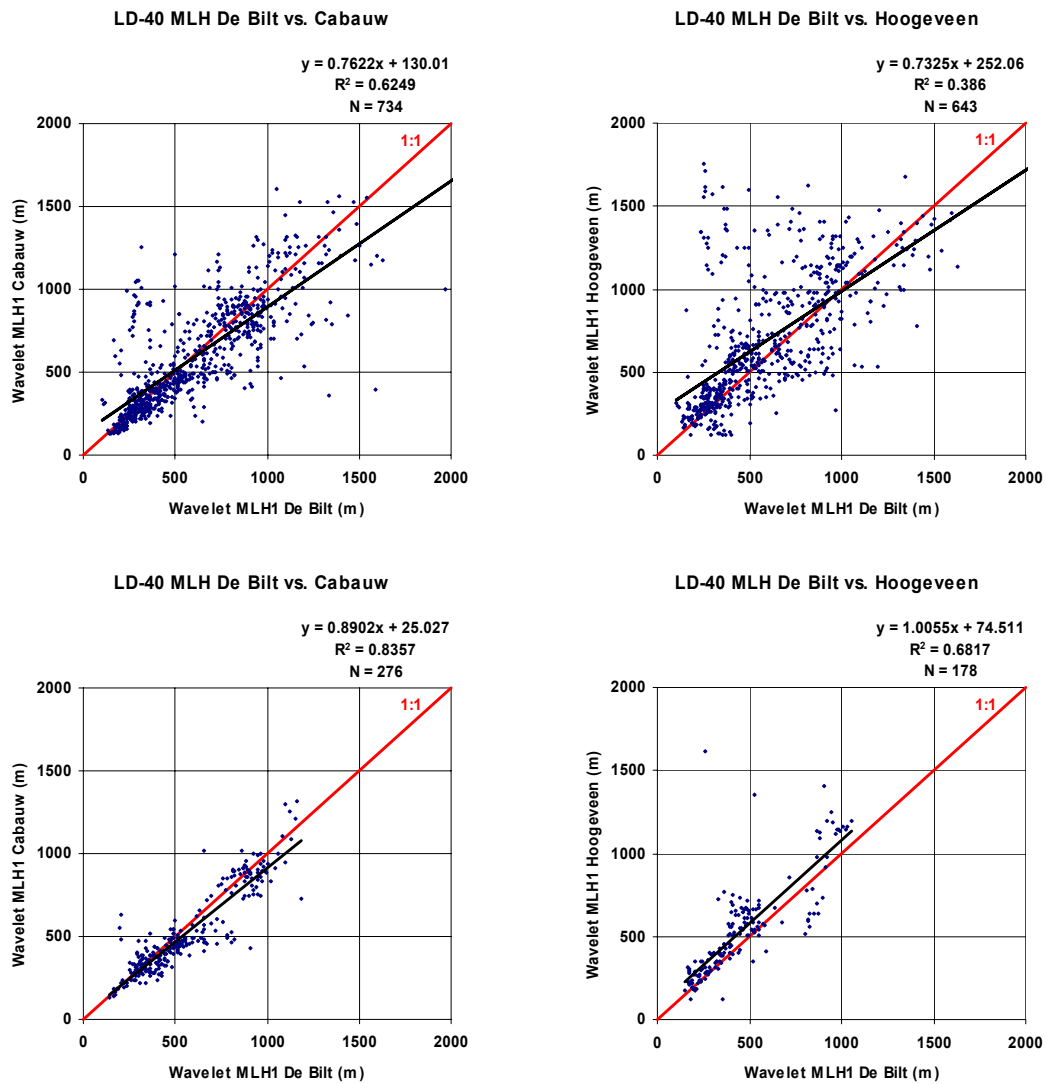**FIGURE A.3.** Same as Figure A.2, but for October 5, 2001.

The LD-40 in De Bilt detects a marked maximum Wavelet MLH1 at 953 m, while at the same time Cabauw, Hoogeveen and Schiphol report a MLH1 between 743 and 990 m. The ML growth rate during the morning period shows similar characteristics for all four stations, but it is fairly lower at Schiphol compared to the others. This is assumed to be the result of the older internal LD-40 software version of the Schiphol LD-40 that was yet upgraded at the time. This is also observed in an overall comparison for all cases in August (not shown), and is supported by an improved agreement for the newer software version in case of the October days. Therefore Schiphol data are not included in the analysis presented here.

Another example for the same four stations is given in Figure A.3, for October 5, 2001. In all four panels, the specific shape of the development and decay of a convective mixing layer is detected by the algorithm. The mixing layer is topped with some cumulus clouds during the day. Note that, whereas the contour plots for Cabauw, De Bilt and Schiphol resemble each other very much, the contour plot for Hoogeveen is characterised by significantly other aerosol backscatter structures and cloud bases between 700 and 1100 m in the early morning (00 – 04 UTC). Furthermore, note the tempered development of the mixing layer after sunrise, probably caused by the early set in of clouds from approximately 10 UTC. Hence, the maximum of the MLH reached for this station is 960 m, whereas the other three stations show estimates of MLH up to roughly 1200 m. This difference may again be ascribed to the more eastern location of Hoogeveen with respect to the three other stations.

Scatter plots for Wavelet MLH1 at De Bilt, compared with MLH1 at Cabauw and at Hoogeveen for the 13 selected daytime periods (06 – 18 UTC) are shown in Figure A.4. The 13 daytime periods consist of 949 MLH comparison points. For the plots with all simultaneous detections, the difference in correlation coefficient between the two compared locations is remarkable; the well collocated locations of De Bilt and Cabauw (734 points) have a value of R^2 of 0.62, while for De Bilt and Hoogeveen (634 points) a value of 0.39 is found.

In the lower panels of Figure A.4 the same combinations of detections are plotted, but now limited to estimates with a 'Good' quality index for both locations. For Cabauw, 276 points remain, while for Hoogeveen only 178 points satisfy this criterion. The correlation coefficient of the regression analysis has increased to 0.84 for Cabauw and to 0.68 for Hoogeveen. Note the good agreement which can be seen in all plots for lower MLHs, while for higher MLH a lot more scatter is visible. This behavior was already noticed in the comparison with other measurement platforms in the main report.

Apart from the instrumental artifacts which can play a role, the horizontal variation of MLH can be attributed mainly to the horizontal variation of the surface heat flux. Hence, the soil type, land use and soil moisture content are determining the local development of MLH, but also surface roughness and orography may be important. Furthermore, a comparison of MLH at locations that are far apart from each other can also be differently influenced by the passing of mesoscale systems, or differences in the occurrence, timing or source areas of advected aerosol layers.

LD-40 MLH De Bilt vs. Cabauw

y = 0.7622x + 130.01
R² = 0.6249
N = 734

LD-40 MLH De Bilt vs. Hoogeveen

y = 0.7325x + 252.06
R² = 0.386
N = 643

LD-40 MLH De Bilt vs. Cabauw

y = 0.8902x + 25.027
R² = 0.8357
N = 276

LD-40 MLH De Bilt vs. Hoogeveen

y = 1.0055x + 74.511
R² = 0.6817
N = 178

FIGURE A.4. Scatter plots for daytime LD-40 Wavelet MLH1 in De Bilt vs. Wavelet MLH1 in Cabauw (left) and Hoogeveen (right), for 13 selected days in August and October 2001. In the upper panels, all simultaneous detections are shown, while in the lower panels only detections with a 'Good' quality index are taken into account.

Appendix B Instrument dependent overlap functions

The overlap correction that was introduced in chapter 3 has been generated by Vaisala, and is an improvement of the geometrical overlap function that is embedded in the LD-40 software. Because of tiny variations of lens and laser diode properties each ceilometer has an individual overlap function differing slightly from the standard (Schäfer et al., 2004). There have not been any investigations yet about the error and relative difference for different instruments. Since the main purpose of the LD-40 is cloud base detection, not much effort has been spent on this subject by the manufacturer.

The future application of the ceilometer MLH algorithms assessed in this report is to study the spatial variation of MLH in The Netherlands. As this feasibility study is mainly based on backscatter data for De Bilt and Cabauw, it is important to investigate whether the application of the MLH algorithm shows comparable performance for different LD-40 instruments. The windows of the LD-40 ceilometers which are operational in the KNMI network are cleaned every six months. Furthermore, an instrument is replaced with a spare if the calibration period has expired or in case of malfunctions or if users report complaints about the operation of the ceilometer. In the six years of stored LD-40 data for De Bilt (2000 – 2005), various instruments were operational (Table B.1). This gives the opportunity to compare derived overlap functions from data measured by different ceilometers to validate the standard overlap correction as provided by Vaisala.

TABLE B.1. Overview of the LD-40 sensor history 2000 to 2005, for test station 261 in De Bilt. (Source: KNMI MI/INSA Meetsystemen beheer.)

start date	end date	sensor nr.	comments
?[1]	22-09-00	12	
22-09-00	13-03-01	11	Replaced; sensor with new software version.
13-03-01	10-10-01	9	Replaced; failure. Bad data communication.
10-10-01	15-10-03	25	Replaced; test of sensor from Beek, with complaints.
15-10-03	05-04-04	19	Replaced; calibration period expired.
05-04-04	04-06-04	23	Replaced; test of sensor from De Kooy, with complaints.
04-06-04	10-06-04	31	Replaced; failure. Faulty cloud base detection.
10-06-04	09-11-04	23	Replaced; failure. Faulty cloud base detection.
09-11-04	?[2]	17	Replaced; testing sensor from Beek, with complaints.

The 1 minute range corrected profiles in the KNMI format were analysed for this purpose for each sensor separately. Only relatively clean and monotonously increasing backscatter profiles, free from disturbing structures like clouds or advected aerosol layers, were taken into consideration. Therefore profiles with a cloud base, vertical visibility or maximum range of detection below 1000 m, or with precipitation were rejected. In addition profiles with decreasing backscatter in the lowest 500 m and profiles with backscatter values

---

[1] Start date unknown; a new sensor database was employed in the year 2000.
[2] End date unknown; sensor is still operational (reference date August 1, 2006).

larger than $\ln(Pr^2) = 12.5$ at a height of 270 m were omitted. Finally, points with a value for $\ln(Pr^2)$ of 10.1 were rejected, because these are cut off and may deteriorate the results. A similar fine tuning of the overlap function was carried out by Schäfer et al. (2004) and should generate overlap corrected backscatter signals varying only slightly up to a height of 300 m. Several hours of filtered data for one instrument can be used to adapt the overlap function to its individual properties.

The filtered backscatter data were analysed by means of two different parameters for each day. The minimum daily backscatter value at each range gate was stored, together with the daily mean value of all selected backscatter values at each range gate. Next, the corresponding overlap correction factors (B_{min} and B_{mean}) for each value were calculated by converting the aforementioned parameters to the range corrected backscattered power and dividing this value by the range corrected backscattered power at a fixed level. This fixed level was chosen at the 36th range gate (270 m), because the overlap correction profile provided by Vaisala exceeds the value of 1 in this gate (i.e. 1.015) for the first time. The vertical domain of consideration is between 0 and 1800 m.

The estimated overlap correction functions in the lowest 270 m of the vertical domain, for six of the sensors listed in Table B.1, are shown in Figure B.1, together with the standard LD-40 overlap profile provided by Vaisala. Sensor 31 is not taken into account in this analysis, because of the short period of operation. The relative error for each range gate, with respect to the standard Vaisala profile, is presented in the lower panel of this figure. Note the very large differences from the Vaisala overlap for all sensors below 112.5 m. These large errors are mainly caused by the aforementioned truncation to a value of 10.1 of all backscatter values lower than 10.2. The truncated backscatter values were omitted in the analysis, which implies an unrealistic derivation of overlap factors from the remaining backscatter values. As a result of this rejection, the estimated overlap factors for the lower gates are based on a lower number of data points because of the very low overlap of the transmit and receiver beam. The number of available data points for each gate is generally more or less constant for the gates at 112.5 m and those beyond. The gate at 112.5 m is also the first one at which the calculated relative error of all sensors is below 20 % with respect to the Vaisala overlap. For sensors #9 and #23, the error becomes larger than 20 % again at 127.5 m, but generally an improving agreement is observed beyond the 112.5 m level. Note that it is especially sensor #25 which underestimates the Vaisala standard overlap, which means that backscatter profiles from this instrument are too much corrected when the standard overlap profile is applied for correction. On the other hand, sensor #23 overestimates the Vaisala standard overlap very much.

A further refinement of the overlap correction profile for the individual ceilometer instrument can be achieved by a tuning of the overlap profile construction criteria mentioned in this section and an analysis of the variability of the estimated overlap function. Furthermore, the use of raw data (see Appendix D) may provide more available measurements for the lowest range gates, which enables a further analysis of the highly erroneous estimated overlap factors below 112.5 m here. This improvement is possible because of the higher resolution and the absence of truncation in the raw data format.
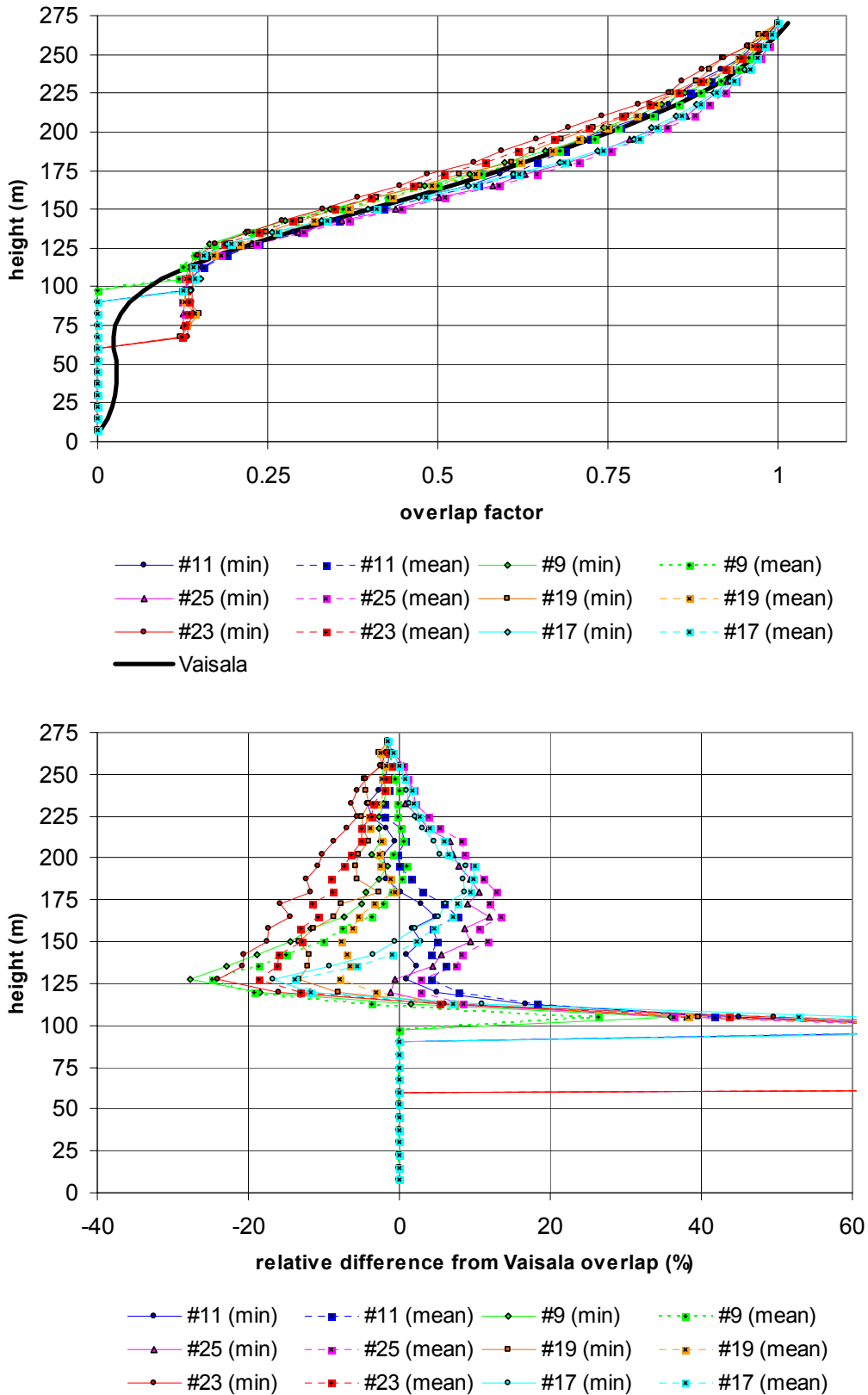
FIGURE B.1. Estimated overlap factors (upper) and relative difference with respect to the standard Vaisala LD-40 overlap function (lower) for six LD-40 sensors, operational at station 261 in the period 2000 – 2004. The vertical range under consideration is between 0 and 270 m. Note that the x-axis in the lower panel is cut off at a relative difference of +60 %.

Appendix C   Entrainment Zone Thickness estimation

The vertical extent of the entrainment zone is determined by the minimum and maximum height at which thermals that originate at the surface stop to rise due to the presence of a capping inversion. The entrainment zone thickness (EZT) was defined by Deardorff et al. (1980) as "the depth being confined between the outermost height reached by only the most vigorous penetrating parcels and by the lesser height where the mixed-layer fluid occupies usually some 90 to 95 percent of the total area". For example, Steyn et al. (1999) estimated the EZT from a MLH time series inferred from lidar measurements with $EZT = 2.77\sigma$. Hence, the top of the entrainment zone becomes $h_{top} = MLH + 1.38\sigma$, whereas the bottom height of the entrainment zone becomes $h_{bottom} = MLH - 1.38\sigma$. This corresponds to a location of the boundaries at 8 % and 92 % of the mixing layer height distribution of the time series.

The backscatter profiles used in this analysis are the averages of the five profiles available from the X1RD telegram every minute. A vertical smoothing is applied on these profiles, on a height interval of 67.5 m (+/- 4 gates). For the estimation of EZT, a time interval of 10 minutes is used. Hence, the calculated standard deviation is based on 10 consecutive MLH1 determinations. The output is calculated every minute. The corresponding horizontal scale of the smallest aerosol structure that can be distinguished is strongly dependent on the horizontal wind speed above the ceilometer site, ranging from 60 m for a mean wind speed of 1 m/s to 600 m for a mean wind speed of 10 m/s.

The cases shown in Figure C.1 have already been introduced in the case studies in chapter 5. The analysis period here is limited between 06 and 12 UTC, when the development of a convective mixing layer is possible. For the upper two panels, this development is clearly seen. The variability of the MLH time series increases enormously during the analysis period, indicating the presence of rising thermals with alternating strength. Whereas thermals with a high amount of buoyancy will overshoot the mean MLH up to the top of the entrainment zone, thermals with less buoyancy undershoot the mean MLH. The high resolution variability of the MLH1 time series as estimated with the Wavelet algorithm is generally in good agreement with the observed variability in aerosol backscatter by visual inspection of the contour plot.

The high temporal variability of MLH1 that is seen during the morning hours in the first two cases, is not present on January 14, 2006. The neutral shallow situation demonstrates a fairly constant MLH1 around 300 m, even for this high resolution analysis. The latter is caused by a strong capping inversion (increase in θ_v of approximately 8 K over only 100 m at 12 UTC) and only little buoyant activity. The quality indices for all analysed periods are generally good. Except for some 'Poor' (=red) estimates during the convective periods on May 11, 2000 and August 29, 2005, the majority of the estimates shows a 'Good' (=green) or 'Weak' (=yellow) quality index. This supports the reliability of the results shown here.
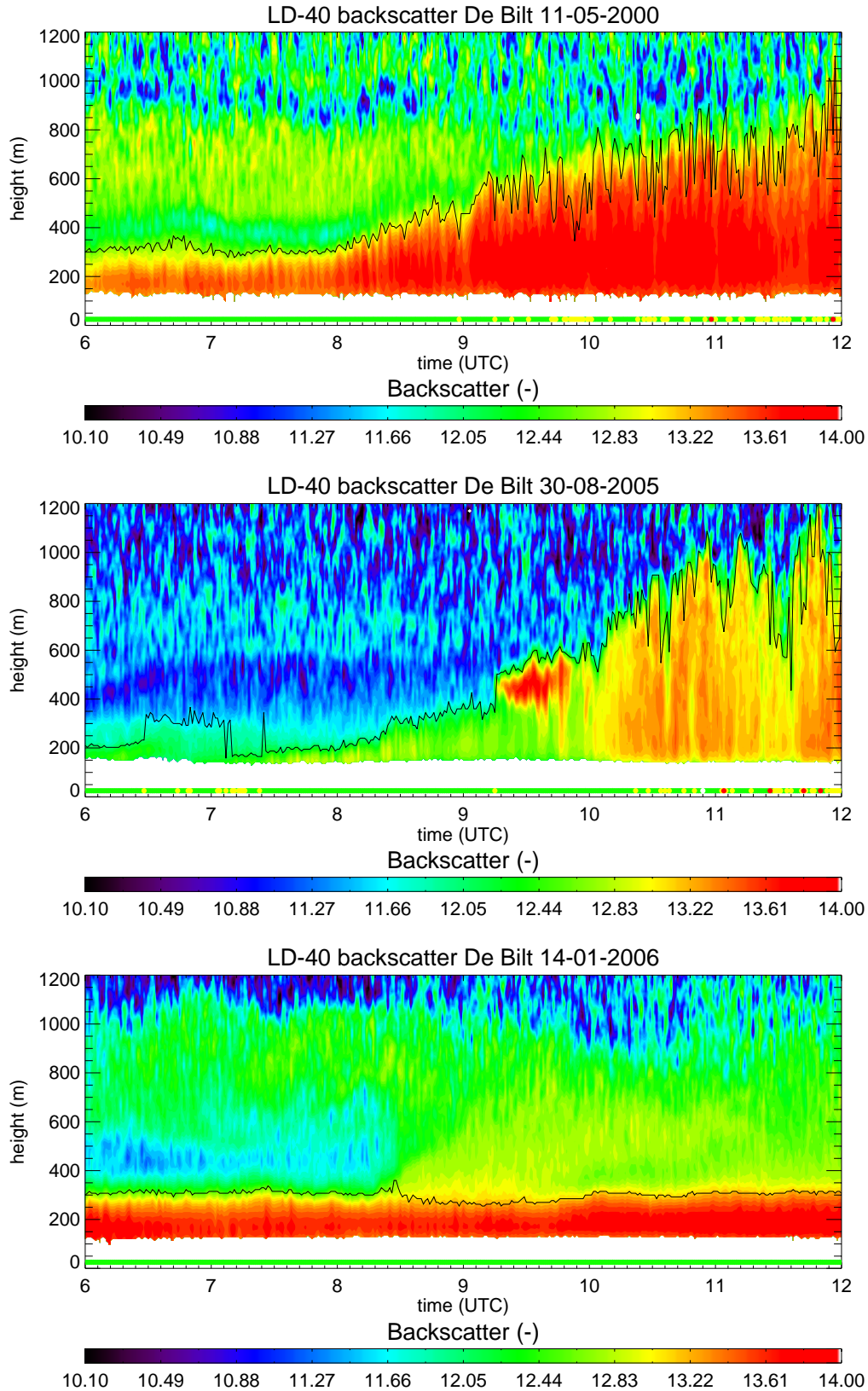
FIGURE C.1. LD-40 backscatter contour plots for De Bilt on May 11, 2000 (upper), August 30, 2005 (middle) and January 14, 2006 (lower). The 1 minute estimates of Wavelet MLH1 are indicated by the black line. For visualisation purposes, the upper boundary of the backscatter color bar has been changed to 14.0.

The estimates of the EZT for the three days in Figure C.1 are shown in Figure C.2. For that purpose the Steyn definition of the entrainment zone thickness is used: $EZT = 2.77\sigma$. Note the large difference between the two convective ML cases and the shallow wintertime ML case, which was already pointed out in the above mentioned discussion about Figure C.1. Since the entrainment zone is not present during nighttime, the EZT estimates during nighttime are from here on called 'MLH variability'. All three cases initially show a nighttime MLH variability below 200 m, in the period before 08 UTC. The majority of estimates for this period are between 10 and 100 m. The high nighttime values of the MLH variability for August 30, 2005, are caused by the jumping between successive faulty estimates of MLH. Between 08 and 12 UTC, EZT increases to values between 200 and 400 m for May 11, 2000 and August 30, 2005 respectively, whereas the EZT for January 14, 2006 persists at a value of about 50 m during the whole day. Only around 18:30 UTC, the EZT peaks to higher values, due to a short period with some faulty MLH detections.

· 11-05-2000 · 30-08-2005 · 14-01-2006
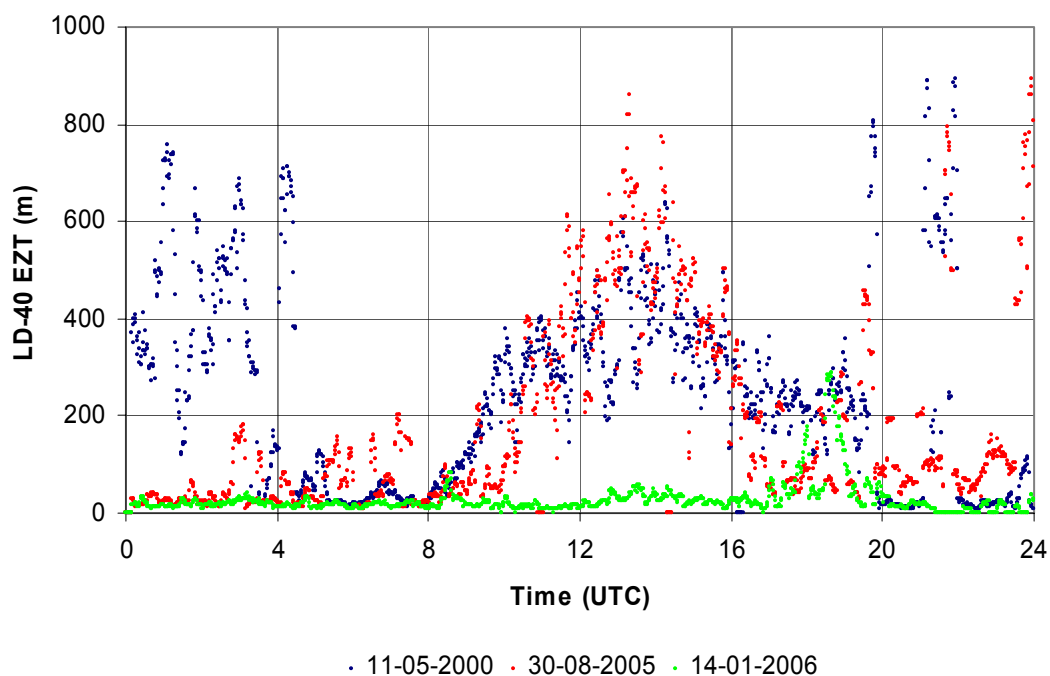
FIGURE C.2. EZT estimates for De Bilt on May 11, 2000 (blue), August 30, 2005 (red) and January 14, 2006 (green). Results are derived from the standard deviation calculated for ten 1 minute Wavelet MLH1 determinations.

The radiosonde observations of virtual potential temperature at 12 UTC (not shown) demonstrate inversion layers with a depth of roughly 100 m for January 14, 2006 and 400 m for May 11, 2000. Although this is not a very accurate estimator for the depth of the entrainment zone, the agreement with Figure C.2 seems evident. For the afternoon period, the convective ML cases report maximum values of EZT between approximately 200 and 700 m. The latter high values mainly occur during periods containing a significant number of 'Poor' detections on August 30, 2005, in the hours after noontime. The high temporal variability of MLH1 that corresponds to these high values of EZT was also observed in the 10 minute estimates, see Figure 5.3. The expected diurnal variation of MLH variability is also observed in Figure C.2 in the evening, when values return more or less to their initial morning values below 200 m.

Following Beyrich and Gryning (1998), the EZT is typically 20 to 30 % of the whole MLH, but it may reach a depth comparable to that of the mixing layer itself, in cases of a very shallow ML or during phases of rapid ML growth. According to Stull (1988), the EZT can reach heights of up to 40 % of the MLH. The EZT/MLH ratio for the considered days in this section is up to 0.2 for nighttime observations, while convective daytime ratios are mostly between 0.2 and 0.6. The shallow aerosol layer on January 14, 2006 reports relatively low daytime values of EZT/MLH of 0.15 at most. Finally, it should be remarked that in principle only reliable consecutive detections of MLH can lead to an accurate estimate of EZT. In case of MLH estimates alternating between the tops of two different aerosol layers, the EZT determination becomes unrealistic. This is illustrated by the high MLH1 variability on May 11, 2000, 00 – 04 UTC. Hence the estimations should be used with care.
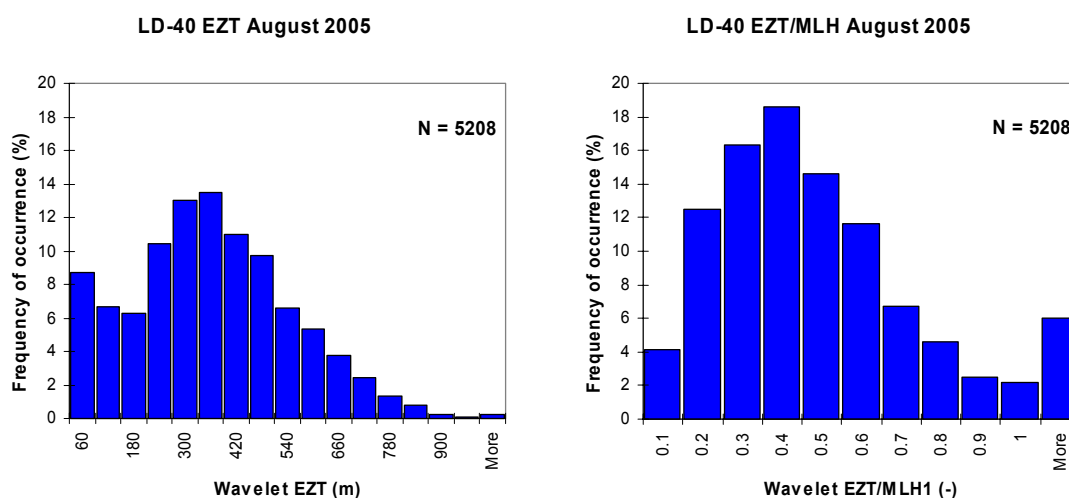
FIGURE C.3. Histograms of Wavelet EZT (left) and EZT/MLH1 ratio (right) distributions for August 2005 08-16 UTC, in De Bilt. A bin size of 60 m (left) and 0.1 (right) is used. The EZT was estimated in 36 % of the total number of cases.

The frequency of occurrence distributions for the estimated EZT and EZT/MLH ratio in August 2005 (De Bilt) are shown in Figure C.3. A total of 14880 1 minute backscatter profiles from the LD-40 is used for the analysis, in the period 08-16 UTC of each day. The method for EZT estimation as described above is used. Hence, no quality check is incorporated.

The maximum in EZT is observed between 300 and 360 m, while the maximum for the scaled EZT/MLH1 parameter is found in the bin between 0.3 and 0.4. This agrees well with the results by the aforementioned studies. A decreasing probability is observed towards EZT/MLH = 1, but also ratios with a value higher than 1 are significantly present (6 % of the cases). It is assumed that the corresponding bin 'More' is mainly populated by outliers caused by the jumping of the algorithm between different layers, like in the morning of May 11, 2000, as discussed in the text concerning Figure C.2.

Appendix D   Raw backscatter data Cabauw

The backscatter data in this report are all in the KNMI data format (Impulsphysik, 1999) supported by software version 3.4 and higher, as described in chapter 3. Backscatter values are stored in the form $\ln(Pr^2)$, with P the average power per transmitted pulse and r the distance between the ceilometer and the measurement volume (gate). To reduce the file size of the KNMI format backscatter file, values of $\ln(Pr^2)$ are coded in an ASCII character with a resolution of 0.2. As mentioned in the description of the data format (section 3.1), the minimum value of $\ln(Pr^2)$ is 10.1, the maximum value is 22.7. This means that only 64 discrete values are possible for the storage of the measurements in the corresponding X1RD telegram. Hence, the measured backscatter is rounded before it is stored in a file on a local PC. Furthermore, values of $\ln(Pr^2)$ smaller than 10.1 automatically obtain the lower limit value, whereas the values exceeding 22.7 are similarly truncated at the maximum value. The LD-40 is used by KNMI operationally for cloud base detection using the LD-40 cloud bases C1, C2 and C3, for this application the reported resolution of the backscatter data does not have any impact on the operational use of the instrument.

However, the use of data with a higher resolution may be interesting for boundary layer investigations of aerosol dispersion, like the MLH assessment study presented in this report. Binary raw files contain the complete raw data telegram as transmitted by the sensor. Each telegram is preceded by a time stamp with a length of 20 bytes. After byte 19, the X1TA telegram is stored, which contains information about the data format and location and orientation of the ceilometer. After the end of this telegram (at byte 116), each of the 2048 gates is represented by 3 bytes, which represents a 6 digit value of the backscatter signal after a transcription to a hexadecimal code of each separate byte. Together with the number of transmitted pulses and the offset, which are stored at the end of the telegram, the corrected signal C for each gate within the vertical domain can be calculated. Subsequently, the average power P [in pW] per transmitted pulse is calculated as $P = 6.23 \times C$ (Münkel, 2006; personal communication). The value of P is not range and overlap corrected.

The total number of bytes stored for each sensor cycle (15 seconds) is 6464. In the period November, 2005 to March, 2006 raw data files were stored for the LD-40 in Cabauw. During this period it was noted that the transmitted data contained three possible data sequences which are shown in Figure D.1 The 'x' marks an arbitrary byte position between 21 and 6262, but mostly 'x' is at the half of this range, around 3000 to 3100. The normal data sequence (1) gives no problems, but for sequences 2 and 3, some steps have to be made before the actual backscatter profiles can be acquired. The unusual location of the X1TA telegram in structure 2 is solved by a simple rearrangement of the bytes in the original order (as of sequence 1). Hence, the last three bytes before byte position 'x' and the first three bytes after byte 'x+97' correspond to two consecutive range gates. The unusual position of the X1TA telegram has been confirmed by other users of the LD-40 raw backscatter data.

For data sequence 3 however, some unknown range gates are missing because of the repeated X_1TA telegram. This problem was also earlier noticed by other users and is probably caused by the fact that raw data transmission is too slow and is therefore interrupted by the next X_1TA telegram, or the receiving PC is delayed during raw data reception. Another cause may be the older software version of the LD-40 in Cabauw. For software version 5.0 and higher, this artifact seems to be solved (Münkel, 2005; personal communication). The occurrence of irregular data sequences ranged between 5 and 60 % for the period analysed here.

1. Normal sequence

Byte position	0-19	20-116	117-6262	6263-6463
Data content	Timestamp	X_1TA	Backscatter	Sensor information

2. Wrong location of the X_1TA telegram

Byte position	0-19	20-x	x+1-x+97	x+98-6262	6263-6463
Data content	Timestamp	Backscatter	X_1TA	Backscatter	Sensor information

3. Repeated X_1TA telegram

Byte position	0-19	20-x	x+1-x+97	x+98-x+194	x+195-6262	6263-6463
Data content	Timestamp	Backscatter	X_1TA	X_1TA	Backscatter	Sensor information

FIGURE D.1. Overview of the three different possible LD-40 raw data sequences. See the text for a discussion.

Figure D.2 shows the raw LD-40 backscatter data for Cabauw on November 10, 2005. Note the wave pattern which is visible in the lowest 800 m of the backscatter contours. This so-called ringing effect is an instrument artifact and is commonly observed in scattering measurements from remote sensing instruments (Schäfer et al., 2004). Concerning the LD-40 ceilometer, it is related to the fact that the receiver electronics are slightly disturbed by the transmitter, when the laser pulse is triggered by high voltages. Since the physical distance to the receiver is quite close, even the applied strong electric shielding can not completely extinguish this effect. This effect occurs for all receivers and transmitters. Some effect is always there, but the magnitude can differ (Münkel, 2006; personal communication). Hence, it is not only observed in backscatter data stored in the raw format, but also the KNMI format data suffer from it.
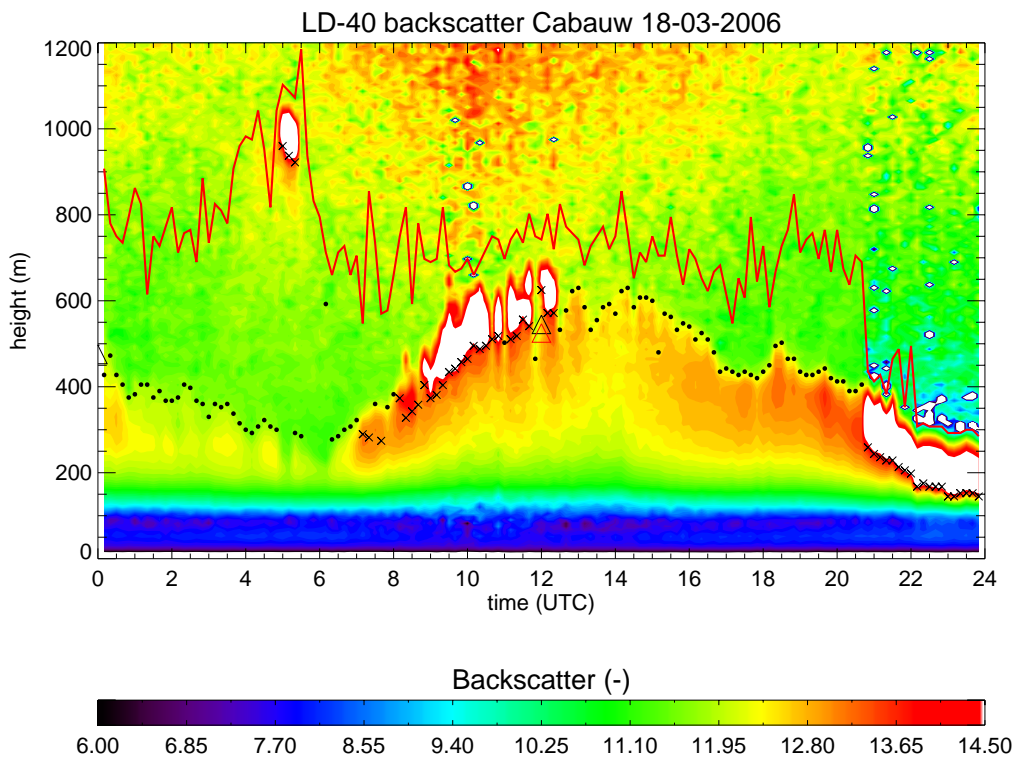
Figure D.3 shows two backscatter contour plots with estimates of MLH_1 for Cabauw on March 18, 2006. The raw LD-40 backscatter data used are range corrected and expressed in $\ln(Pr^2)$, as in the KNMI data format. No overlap correction is applied. In the upper panel, the original raw data are presented, with a numerical resolution of 0.001 and without a truncation of data at a lower or upper limit. The lower panel shows the raw data after it was adapted to the KNMI format, with a numerical resolution of 0.2 and truncated to a fixed value of 10.1 for all values below 10.2. Only the available backscatter profiles with a normal data sequence within the 10 minute interval are used for the calculation of the averaged 10 minute backscatter profile, because of the aforementioned occurrence of data with a repeated X_1TA telegram. The parameters as derived by the internal LD-40 software (i.e. C1 to C3, VV, CX and PI) were retrieved from another file which is transmitted by the sensor in raw mode (the so-called TXT file).
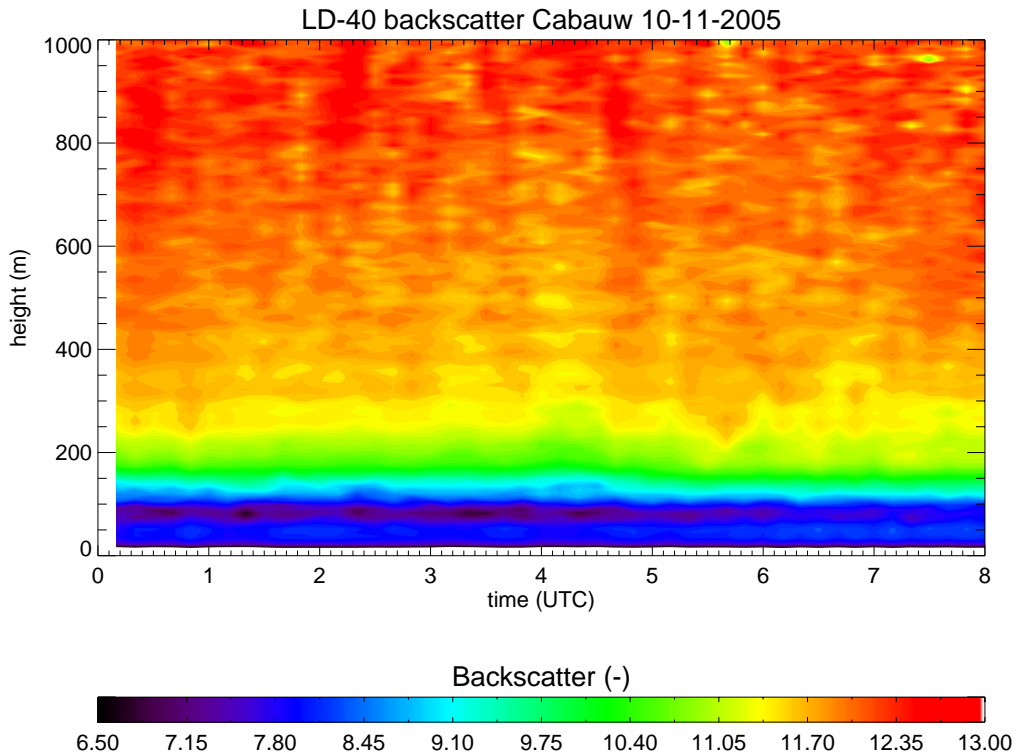
FIGURE D.2. LD-40 raw backscatter contour plot (in ln(Pr²) units) for Cabauw on November 10, 2005. Data are corrected for range, but not for overlap. Note the adjusted range of the color bar.

The figures show very similar results for this day with respect to the estimates of MLH1, as well as to the height of the derived SNR stop level. A developing mixing layer accompanied by clouds is observed for both formats, reaching values of MLH up to 600 m during the afternoon. Hence, there is no direct indication for an improvement in MLH estimation by the use of the LD-40 raw data. The differences concerning the use of the data formats are mainly observed in the backscatter contours. Whereas the 'KNMI format' (lower panel) has no valid backscatter data other than 10.1 due to truncation below approximately 150 m, the contour plot for the raw format (upper panel) shows valid backscatter data as from the second range gate, at 15 m. Observed values in these lower gates range between roughly 6 and 10, in ln(Pr²) units. The figures do not contain any overlap correction, therefore the real backscatter values for these lower gates are significantly higher. An overlap correction for the individual ceilometer should be determined (see Appendix B) before realistic values of the backscatter can be obtained below 270 m. This would also offer the opportunity to estimate values of mixing layer height in the lowest 150 m of the atmosphere, if necessary.

As discussed in Appendix B, a fine tuning of the overlap function for a single ceilometer was carried out by Schäfer et al. (2004). Several hours of filtered data for one instrument were used to adapt the overlap function to its individual properties, resulting in a correction differing only slightly up to a height of approximately 300 m.

FIGURE D.3. LD-40 raw backscatter contour plot (in ln(Pr²) units) for Cabauw on March 18, 2006. The parameters are again indicated as listed in Table 5.1. For visualisation purposes, the quality index is not shown.
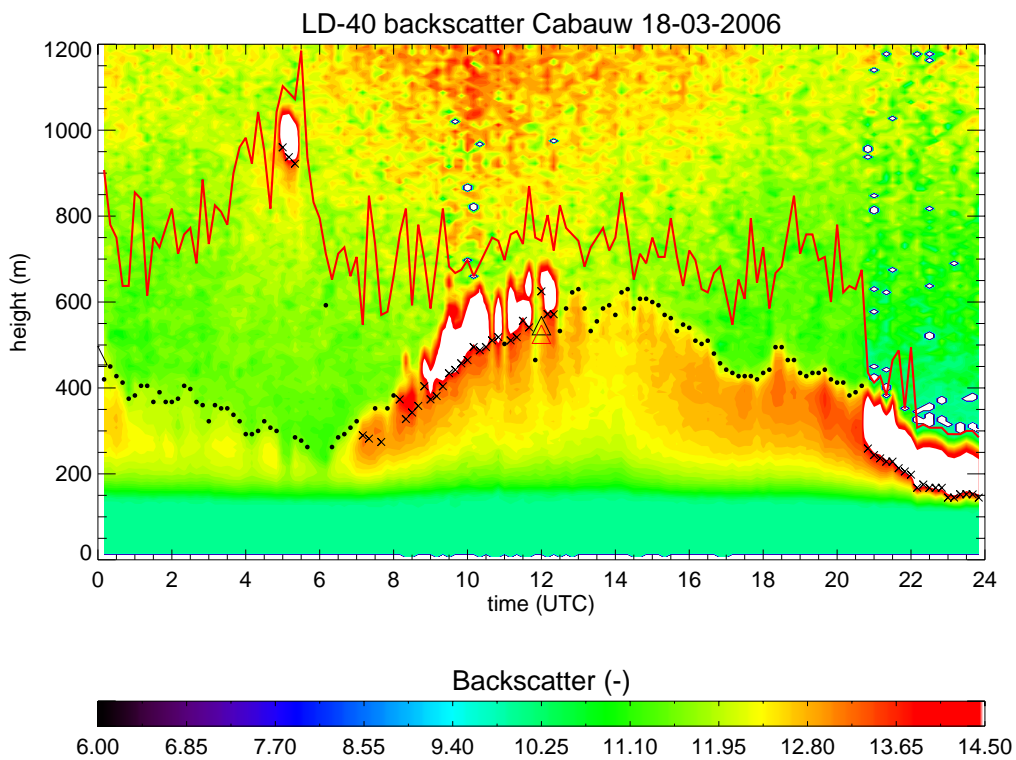
FIGURE D.4. Same as Figure D.3, but with data adapted to KNMI format. This implies a numerical resolution of 0.2 and a truncation of backscatter values to a lower limit of 10.1.

Appendix E   Local air quality monitoring

The Institute for Public Health and the Environment (RIVM) in Bilthoven, The Netherlands, operates a national measurement network for air quality monitoring, "Landelijk Meetnet Luchtkwaliteit" (LML). Concentrations of atmospheric and precipitative pollutants are measured at 48 locations spread over the country. The results are transmitted to the central computer in Bilthoven every hour, where the data are validated and incorporated in the national data base. The LML dates originally from 1973 and reached its maximum number of 244 measurement locations in 1983. Nowadays, the 48 remaining stations contain instruments that measure near surface concentrations of gaseous components like CO, O_3, NO_2, SO_2 and NH_3, but also particle concentrations of e.g. PM10 (dust), black smoke, acid substances and metals are measured.

In this section the focus is on a comparison with measurements of the mean daily PM10 concentration, which is the concentration of the dust particles in the atmosphere with a diameter smaller than 10 µm. It is important to note that a ceilometer is incapable to discriminate between particle sizes. For this purpose, and the estimation of microphysical properties of aerosol in general, quantitative backscatter and extinction profiles at multiple wavelengths are required.

Münkel et al. (2004) estimated PM10 concentrations from aerosol backscatter measurements of the Vaisala CT25K and LD-40 ceilometers. The near surface concentrations of the dust particles were compared with aerosol backscatter in the lowest 30 m of the atmosphere. The authors concluded that both ceilometers are able to monitor aerosol concentration fairly well, even though the design of the LD-40 is bi-axial. For a period of 1 year of data from the CT25K ceilometer and in-situ PM10 measurements in dry conditions, a l.s.q. regression correlation coefficient of 0.84 was found.

Time series of the average LD-40 aerosol backscatter (De Bilt) between 90 and 150 m and measured concentrations of PM10 at two locations in the city of Utrecht are shown in Figure E.1 for the period April – June 2005. For the calculation of the LD-40 average backscatter, 10 minute averaged backscatter profiles from the daily data files were used and profiles contaminated by rain (PI>1) or a cloud base below 600 m were excluded. Hence, the considered data are not influenced by the presence of cloud or rain droplets, which would enhance the measured backscatter intensity. Next, all gates between 90 and 150 m with a value for $\ln(Pr^2)$ larger than 10.1 were converted to the corresponding range-uncorrected value of P [in pW] and summed in order to eventually calculate the mean value by dividing the result by the number of incorporated gates. The PM10 measurements are taken from the hourly available validated data for the urban stations number 636 (Utrecht, De Jongweg) and 639 (Utrecht, Erzeijstraat), located only a few kilometres southwest and west from the LD-40 at the KNMI site in De Bilt.

Note the high consistency between days with a high daily mean PM10 concentration and days with high values for the mean LD-40 backscatter in the lowest 150 m. This is especially well seen for the coinciding maxima of the two parameters in the second half of

April and the beginning of May. For the maxima that do not coincide precisely, most of the time the maximum in backscatter follows one or two days later. This lag is not remarkable, whereas aerosols may reside for a longer time in the lower atmosphere, especially in periods without rain or frontal clouds. Furthermore, the time series of PM10 concentration for the two locations agree very well, with persisting higher values reported for station 639. Some weak smog events (24 h mean PM10 concentration > 50 μg/m³) are recognised.
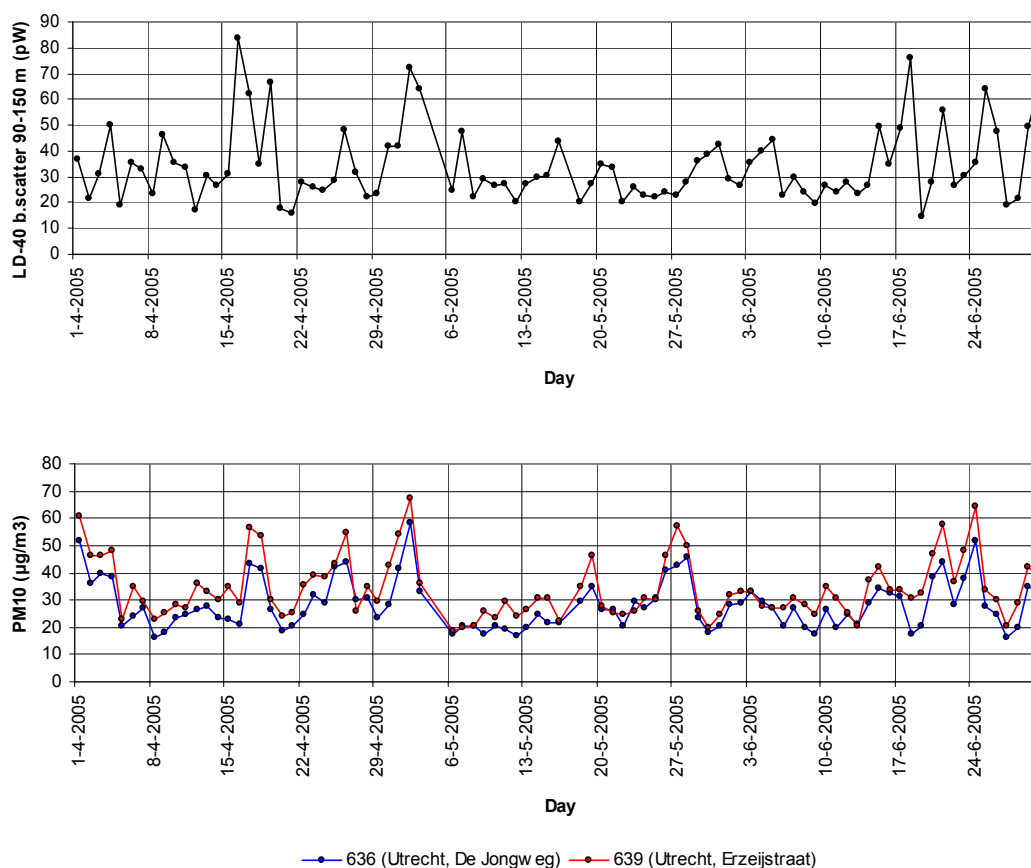
FIGURE E.1. Time series of average LD-40 backscatter (0-150 m) in De Bilt (upper) and PM10 concentrations at the stations 636 (Utrecht, De Jongweg) and 639 (Utrecht, Erzeijstraat) (lower), for the months April, May and June, 2005. Data source for the PM10 measurements: RIVM, Bilthoven, National Measurement Network for Air Quality (LML): http://www.lml.rivm.nl/.

The comparison carried out in this section gives a first insight in the ability to link LD-40 measurements to in-situ measurements of PM10 concentration. Variability in wind speed and differences in aerosol source area, land use and measurement errors should be incorporated in the analysis to give an estimate of the reliability of the derived measurements. Furthermore, the backscatter profiles were analysed between 90 and 150 m, whereas Münkel et al. (2004) only used the overlap corrected range gates between 0 and 30 m. The latter is assumed to be more representative for in-situ near surface measurements of particle concentrations. A better collocation, an overall more strict selection on fair weather cases and a comparison of more hourly (instead of daily mean) PM10 measurements might result in a possible calibration of the LD-40 backscatter with respect to PM10 concentration.
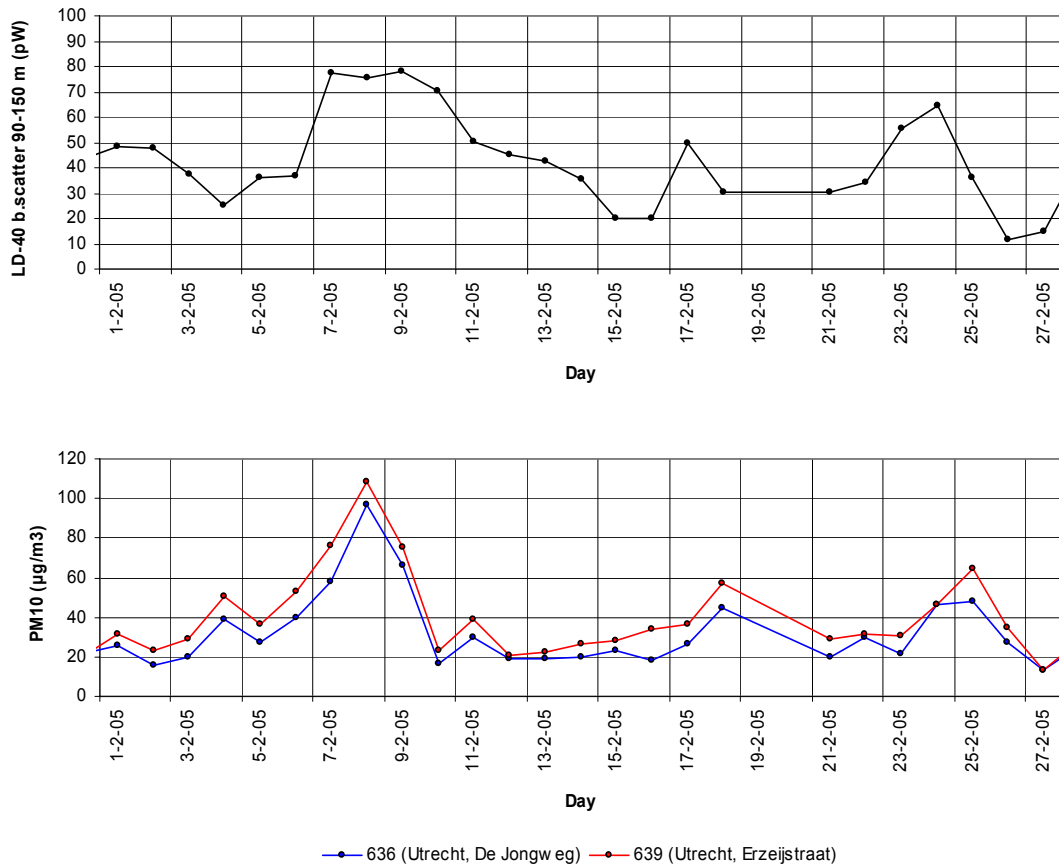
636 (Utrecht, De Jongweg) ——— 639 (Utrecht, Erzeijstraat)

FIGURE E.2. Same as Figure E.1, but for February, 2005.

An additional example for a monthly comparison between the near-surface daily mean backscatter in De Bilt and PM10 concentration measurements at the two RIVM stations in Utrecht is shown in Figure E.2, for February 2005. Coinciding maxima are observed around the 8th, 18th and 25th of this month.

PM10 particles are the main atmospheric constituents emitted when fireworks are let off. Concentrations of PM10 are known to increase enormously during the first hours of the New Year and are mainly dependent on the weather situation and the geographical (i.e. rural or urban) location of the observation (RIVM, 2003).

In Figure E.3, the backscatter contours are plotted for the period from 20 UTC on December 31, 2004 to 04 UTC on January 1, 2005. Note that the time in the plot is in UTC, whereas the local time in The Netherlands (MET) is UTC + one hour. Reduced values for aerosol backscatter are observed until approximately 23:20 UTC. Hereafter, approximately 20 minutes after the turn of the year, the near-surface emissions caused by the fireworks have dispersed up to 250 m. Note the large contribution of multiple scattering that is suddenly present in the aerosol backscatter, changing the lower boundary of the reliable signal down to a height of 52.5 m. The high values of LD-40 backscatter persist during the first hours of the new year. This enhanced backscatter coincides with a high concentration of PM10. For example, the regional stations in Utrecht report maximum PM10 concentrations of 534 and 574 µg/m³ between 02 and 04 MET. As one notes that the thresholds for weak and severe smog are fixed at 24 hour

mean PM10 concentrations of 50 and 200 μg/m³ respectively, the above mentioned values show that a serious amount of dust is emitted in the atmosphere after the turn of the year. The estimates of MLH1 as derived with the Wavelet algorithm continuously jump between an aerosol layer with its top at 90 m and an aerosol height between 200 and 300 m. This might be related to aerosol from other areas which pass over the ceilometer site, driven by the wind a few hundreds of metres above the surface. Another possible cause for this behavior is the unreliable overlap correction for low range gates.
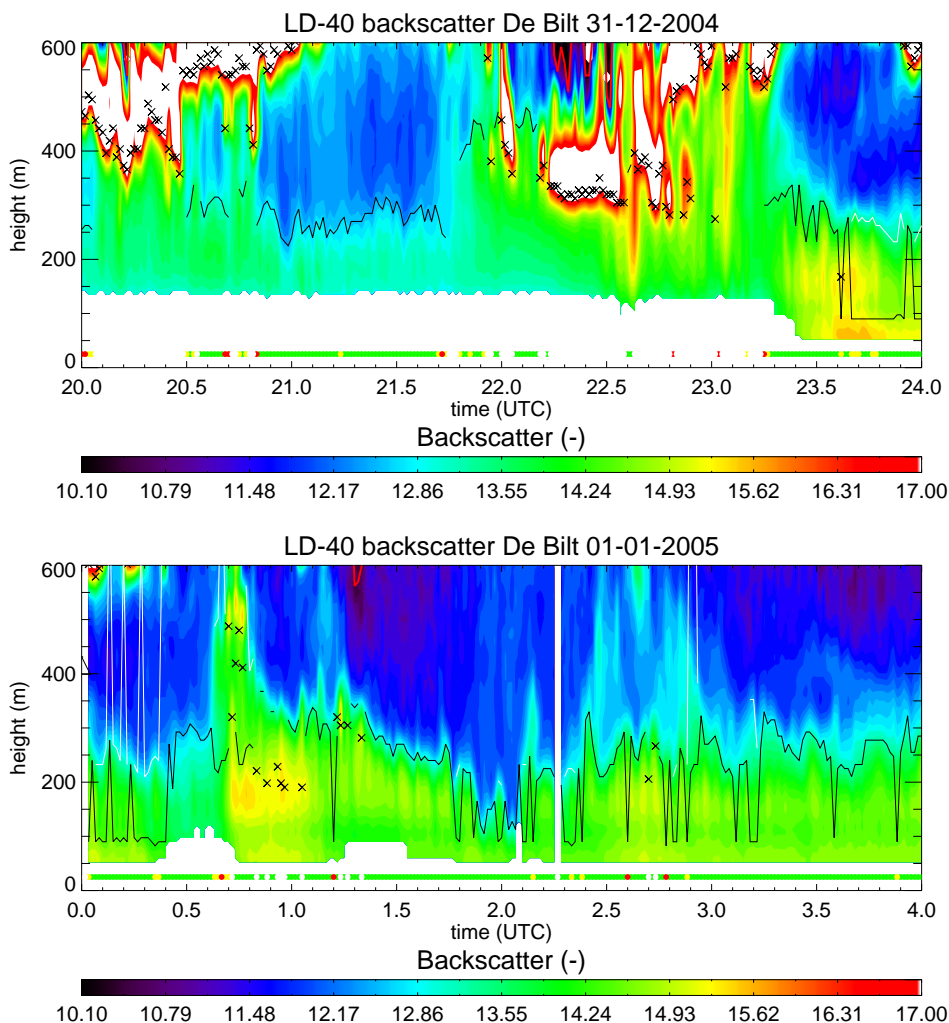
FIGURE E.3. LD-40 backscatter contour plots for De Bilt on December 31, 2004 (upper) and January 1, 2005. The 1 minute estimates of Wavelet MLH1 and MLH2 are indicated by the black and white line, respectively. For visualisation purposes, the upper boundary of the backscatter color bar has been changed to 17.0.

Considering the examples discussed in this section, it can be noted that the ceilometer is sensitive to (high) PM10 concentrations. The mean daily values of PM10 from the LML seem to correlate nicely with the near surface LD-40 backscatter at a nearby site. Hence, it can be used as a qualitative indicator for the spatial and temporal variation of observed PM10 concentration. However, one has to keep in mind that a ceilometer is incapable of determining microphysical properties of aerosol.